

國立臺灣大學電資學院電機工程學研究所
博士論文

Department or Graduate Institute of Electrical Engineering
College of Electrical Engineering and Computer Science
National Taiwan University
Doctoral Dissertation

奈米金粒子在光聲生醫影像之應用
Applications of Gold Nanoparticles in Photoacoustic
Biomedical Imaging

魏振瑋
Chen-Wei Wei

指導教授：李百祺 博士
Advisor: Pai-Chi Li, Ph. D.

中華民國 九十八 年 七 月
July, 2009

致謝

謝謝指導教授李百祺老師，您一直不厭其煩地在研究上、生活上、待人處事上以身教言教的方式讓我學習成長，我無法以言詞準確地表達我由衷的感謝，只能誠懇地向老師說：謝謝您！

謝謝六年來實驗室的學長學姐同學學弟學妹們，不管是一起討論研究、一起實驗、一起打球、一起吃飯、一起聊天、一起打混…的日子，都是我學生生涯最充實快樂的一段時光。

謝謝家人們還有妳無限的支持，有你們在身後默默的付出，我才能毫無後顧之憂地完成這本論文。如果我有任何成就，我希望都能獻給你們。

最後是無法看到這本論文的你們，感謝你們為這本論文完成所作的犧牲奉獻。

畢業不是結束，而是開始。我會懷著感恩，將我受到這許多人的幫助以及祝福，回饋給更多人。

ABSTRACT

Photoacoustic imaging is a new imaging technique that has been used to image the optical properties of biological tissues. However, the applications of photoacoustic imaging in most researches have been limited to morphological observations. Also, high optical scattering of biological tissues and depth dependent decay of incident optical energy degrade the detection sensitivity. In this thesis, the use of gold nanoparticles as photoacoustic contrast agents helps to increase the sensitivity of photoacoustic imaging and to extend the applications to functional and molecular imaging, including cardiac functional assessment and cancer diagnosis. In the first part of the thesis, quantitative blood flow measurements based on the time-intensity method were tested. Gold nanoparticles were used as a photoacoustic contrast agent. In wash-in methods, the photo-induced rod-to-sphere shape transformation of gold nanorods was utilized. Results show that the correlation coefficients between the measured velocities and the true values are close to unity. For molecular imaging, photoacoustic imaging was utilized to probe information from oncogene surface molecules of oral cancer cell, OECM1 and Cal27, with the aid of bioconjugated gold nanorods. *In vitro* cell culture and *in vivo* small animal results show that both cancer cells with antibody conjugated nanorods of specific targeting exhibit a higher photoacoustic response than control groups with plain nanorods. Also, angiogenesis targeting was achieved with peptide conjugated gold nanorods. Images of OECM1 tumor with mixed nanoprobe injection also reveal enhanced photoacoustic intensity at different wavelengths than those with mixed plain gold nanorods injection, thus demonstrating simultaneous multiple targeting is feasible and can be used to obtain variable molecular signatures by simply switching laser wavelength. Also, photoacoustic pressure amplitude, which is linearly correlated with temperature, can be applied for real-time monitoring of the temperature non-invasively during photothermal therapy. Quantitative thermal imaging showed that the temperature can reach the hyperthermia level for effective cancer treatment. The results of pathological analysis of the tumor confirm the necrosis of the tumor cells without damaging surrounding normal cells. In the last part of the thesis, a subband imaging method to further enhance the image contrast was developed. The method was based on that high-absorption media generate acoustic waves with higher frequency components, and hence the imaging contrast can be enhanced by appropriate selection of the spectral subbands. The experimental results revealed that the contrast between two absorbers with eight times difference in optical absorption can be effectively

increased by choosing a higher subband. These methods help to recognize the region of interest with gold nanoparticles particularly for *in vivo* studies. In summary, the thesis has realized photoacoustic functional and molecular imaging including quantitative flow/perfusion estimation and multiple targeting on tumor with the aid of gold nanoparticles. Future works will focus on *in vivo* flow estimation on tumor angiogenesis and improvement of detection sensitivity.

Keywords: photoacoustic imaging, gold nanoparticle, blood flow estimation, time-intensity curve, molecular imaging, multiple targeting, targeted thermal therapy, subband imaging



中文摘要

光聲影像為一新興之影像技術，在生醫應用上以得知生物組織中光學的特性為主。然而目前光聲影像研究大多仍侷限於型態觀察為主，而由於入射光能量在生物組織中強散射以及衰減皆會降低光聲影像之靈敏度，在此篇論文中，將使用金奈米粒子來增強光聲影像之偵測靈敏度以及擴展其應用範疇至功能性影像以及分子影像，其應用包含心血管疾病以及腫瘤之偵測以及診斷。在本論文的第一部份中，使用金奈米粒子作為指示劑，以實驗證明時間強度法量化估測血流速度之可行性。沖入法利用金奈米桿在適當脈衝雷射照射下產生形變的特性，實驗結果顯示沖出以及沖入兩種方法所測得之流速與實際流速之間之相關係數皆接近一，顯示其相對流速測量能力。在分子影像的應用上，使用與生化分子接合而具有特異性靶向能力之金奈米，可以偵測癌症細胞表面致癌基因的表現，以口腔癌細胞 OECM1 以及 Cal27 為測試細胞株。離體細胞實驗以及活體小動物實驗結果皆顯示，相較於與純金奈米桿反應，兩種癌細胞與各自有高表現之抗體接合金奈米桿反應能得到較強之光聲訊號，另外，與縮氨酸接合之金奈米桿也被用來對於腫瘤血管新生部份作特異性的辨識。而同時多重靶向性以得到多重分子表徵的目的，也以注射混合之奈米探針並以不同之波長雷射得到光聲影像驗證，注射混合探針之腫瘤在不同波長所得之影像強度皆大於注射純金奈米桿之腫瘤影像強度。靶向性熱治療也可藉由將一連續波雷射與光聲分子影像系統而達成，同時為了安全以及熱治療效力的考量，可在熱治療同時以光聲訊號即時且非侵入式的監控溫度變化，以所得光聲影像量化計算出的溫度影像顯示以加熱靶向性之金奈米桿方式可使腫瘤區域達到過高熱狀態，顯示可達到熱治療目的以及量化估測溫度之目的。腫瘤之病理切片結果也驗證靶向熱治療的效果，在未傷及正常細胞的情況下，腫瘤細胞可有效的被殺死。在本論文的最後，發展了一分頻影像方法，可有效提昇光聲影像之對比，此方法之根據為較高光吸收物質產生之光聲訊號含有較多的高頻成份，因此適當地選擇訊號分頻影像，可有效提昇影像之對比。以光吸收度相差八倍之吸收體所得影像之對比可藉由選擇較高頻之頻帶成像而有顯著的提昇。這些方法有助於提昇在高散射的活體實驗中對於含有金奈米粒子區域（因此光吸收度較高）之偵測能力。本研究使用金奈米實現了光聲功能性影像以及分子影像，包含定量血流量測以及腫瘤的多重靶向性。未來工作以活體之腫瘤血管新生區域流速量測以及提昇系統之靈敏度為主。

關鍵詞：光聲影像，金奈米粒子，血液流速量測，時間強度曲線，分子影像，多重靶向性，靶向性熱治療，分頻影像

GLOSSARY OF SYMBOLS

T : temperature

z : depth

μ_a : optical absorption coefficient

Φ : laser fluence

ρ : density

C_p : heat capacity

$\eta(t)$: laser temporal profile

φ : scalar potential of velocity field

β : thermal expansion coefficient

c_s : speed of sound

P : pressure

R : aspect ratio of gold nanorod

ε_m : dielectric constant

TIC: time-intensity curve

λ : laser wavelength

V : volume of mixing/perfusion chamber

Q : flow rate

t : time

$n_I(t)$: input concentration function of time

$n_O(t)$: output concentration function of time

\otimes : convolution

$\delta(\cdot)$: Dirac function

$h(t)$: transfer function of the mixing system

τ : time constant of the wash-out TIC

MTT: mean transmit time of the wash-out TIC

$\gamma(\cdot)$: gamma function

t_0 : delay time

$\alpha_1, \alpha_2, \alpha_3$: parameters of the gamma function

x : spatial coordinate

$n(x, t)$: contrast agent concentration function of space and time

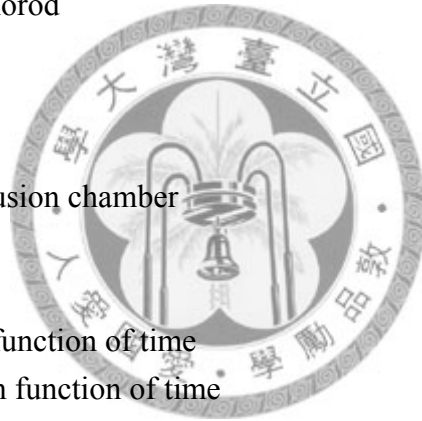
n_0 : initial concentration of contrast agent

$b(x)$: transducer beam profile

σ^2 : variance of $b(x)$ when it is a Gaussian distribution

b_0 : scaling parameter of transducer beam profile

$\exp(\cdot)$: exponential function



$n'(t)$: effective contrast agent concentration versus time

$\Pi(\cdot)$: rectangular function

$l(x)$: destruction profile by laser irradiation

L : laser beam width

l_0 : destruction ratio in the destruction phase in two-energy wash-in TIC

$g(x; t)$: impulse response corresponding to $n(x; 0) = \delta(x)$

v : flow velocity

D : dispersion coefficient

$\text{erf}(\cdot)$: error function

$\text{sgn}(\cdot)$: sign function

d : ratio of D to v

$m(\cdot)$: mathematical model of the wash-in TIC

$\hat{m}(\cdot)$: exponential model for fitting $m(\cdot)$

δ : ratio of u to v

c : model parameter in $\hat{m}(\cdot)$

u : rate constant

E : width of the detection region

PRF: pulse repetition rate

k : laser pulse index

q : destruction rate of a single laser pulse

n_∞ : $(1-s)/(1+rs)$, the steady state concentration of contrast agent in the single-energy wash-in TIC

$n''(k)$: $n'(t - t_0)|_{t=(t_0+k/\text{PRF})} / n_0$

s : $\exp(-u/\text{PRF})$

z : r times s

$\log(\cdot)$: natural logarithm function

$E\{\cdot\}$: take mean

$\text{var}\{\cdot\}$: take variance

Δx : compartment length of vessel

Γ : Grüneisen parameter

κ : diffusion coefficient

μ_s : optical scattering coefficient

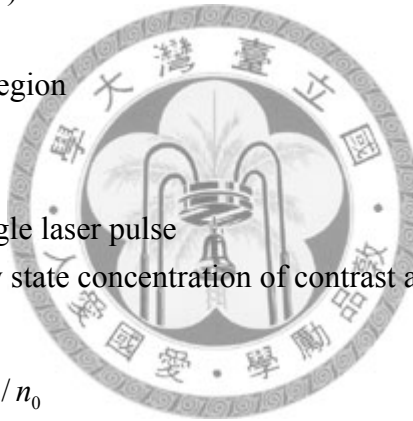
q_0 : isotropic light source

CNR: contrast-to-noise ratio

w : weighting of subband image

$\text{cov}(\cdot, \cdot)$: covariance between two subband images

conts : contrast vector



K : sum of covariance matrices

a : scaling factor of optimal weighting

MPE: maximum permissible exposure of laser to skin

C_a : wavelength dependent parameter in calculation of MPE

VI: vascularity index

Z : acoustic impedance

ε : dielectric constant

Q_m : quality factor



TABLE OF CONTENTS

ABSTRACT	I
中文摘要	III
GLOSSARY OF SYMBOLS	IV
TABLE OF CONTENTS	VII
LIST OF FIGURES	X
LISTS OF TABLES	XVII
CHAPTER 1 INTRODUCTION	1
1.1 PHOTOACOUSTIC IMAGING	1
1.2 PHOTOACOUSTIC IMAGING IN BIOMEDICAL APPLICATIONS.....	2
1.3 GOLD NANOPARTICLES	4
1.3.1 <i>Shape-dependent optical properties</i>	5
1.3.2 <i>Shape transition of gold nanorods</i>	6
1.4 OBJECTIVES.....	7
1.4.1 <i>Quantitative photoacoustic flow estimation</i>	7
1.4.2 <i>Photoacoustic molecular imaging and targeted thermal therapy using bioconjugated gold nanorods</i>	8
1.4.3 <i>Subband imaging for contrast improvement</i>	9
1.5 ORGANIZATION OF THE DISSERTATION	10
CHAPTER 2 TIME-INTENSITY CURVE BASED QUANTITATIVE FLOW ESTIMATION ... 12	
2.1 TIME INTENSITY CURVE FOR FLOW ESTIMATION.....	12
2.2 PRINCIPLES OF PHOTOACOUSTIC WASH-OUT FLOW ESTIMATION.....	15
2.3 PRINCIPLES OF PHOTOACOUSTIC WASH-IN FLOW ESTIMATION.....	17
2.3.1 <i>Derivation for the two-energy method</i>	18
2.3.2 <i>Derivation for the single-energy method</i>	22
2.4 WASH-OUT BASED FLOW ESTIMATION WITH GOLD NANOSPHERES.....	26
2.5 WASH-IN BASED FLOW ESTIMATION WITH GOLD NANORODS.....	29
2.5.1 <i>Phantom results</i>	29
2.5.2 <i>Discussion: effective width of replenishment</i>	34
2.5.3 <i>Discussion: two-energy method vs. single-energy method</i>	35
2.6 CONCLUDING REMARKS	36
CHAPTER 3 PHOTOACOUSTIC MOLECULAR IMAGING	37

3.1 INTRODUCTION	37
3.2 MULTIPLE SELECTIVE TARGETING USING BIOCONJUGATED GOLD NANORODS	39
3.3 <i>IN VITRO</i> CELL CULTURE STUDY	42
3.3.1 <i>Cell culture</i>	43
3.3.2 <i>Antibody and peptide preparation</i>	43
3.3.3 <i>Nanoprobes conjugation</i>	43
3.3.4 <i>Western blot</i>	44
3.3.5 <i>Transmission electron microscopy image</i>	45
3.3.6 <i>Photoacoustic measurement</i>	46
3.4 <i>IN VIVO</i> SMALL ANIMAL STUDY	47
3.4.1 <i>Targeting cancer cell with antibody-conjugated nanoprobes</i>	47
3.4.2 <i>Targeting angiogenesis with peptide-conjugated nanoprobes</i>	52
3.4.3 <i>Simultaneous targeting with mixed nanoprobes</i>	54
3.5 DISCUSSION	56
3.5.1 <i>Photoacoustic signals outside tumor</i>	56
3.5.2 <i>Concentration of targeted nanoprobes on tumor</i>	57
3.6 CONCLUDING REMARKS	58
CHAPTER 4 PHOTOACOUSTIC THERMAL IMAGING OF TARGETED THERMAL THERAPY	59
4.1 GOLD NANOPARTICLES ASSISTED TARGETED THERMAL THERAPY	59
4.2 PHOTOACOUSTIC TEMPERATURE MONITORING	60
4.2.1 <i>Linearity between photoacoustic amplitude and temperature</i>	60
4.2.2 <i>Integration of photoacoustic imaging system and photothermal therapy system</i>	62
4.3 PHOTOACOUSTIC QUANTITATIVE THERMAL IMAGING	63
4.3.1 <i>In vivo studies: subcutaneous injection</i>	64
4.3.2 <i>In vivo studies: tail vein injection</i>	68
4.4 DISCUSSION	71
4.5 CONCLUDING REMARKS	72
CHAPTER 5 PHOTOACOUSTIC SUBBAND IMAGING FOR CONTRAST IMPROVEMENT	73
5.1 INTRODUCTION	73
5.2 RELATION BETWEEN OPTICAL ABSORPTION AND PHOTOACOUSTIC SIGNAL FREQUENCY	74
5.2.1 <i>Numerical simulations</i>	74
5.2.2 <i>Phantom experiments</i>	77
5.3 SUBBAND IMAGING	79
5.3.1 <i>Phantom experimental results</i>	80

5.3.2 <i>Optimal weighting imaging</i>	81
5.4 DISCUSSION.....	83
5.4.1 <i>Signal frequency at backward and forward detection</i>	83
5.4.2 <i>More precise methods for frequency component extraction</i>	84
5.4.3 <i>Geometry dependent frequency</i>	86
5.5 CONCLUDING REMARKS	87
CHAPTER 6 DISCUSSION	89
6.1 LASER SAFETY REGULATION.....	89
6.2 BIOCOMPATIBILITY OF GOLD NANOPARTICLES	90
CHAPTER 7 CONCLUSIONS AND FUTURE WORKS	94
7.1 CONCLUSIONS	94
7.2 FUTURE WORK: <i>IN VIVO</i> PERFUSION MEASUREMENTS	95
7.3 FUTURE WORK: SUBBAND IMAGING FOR <i>IN VIVO</i> STUDIES	97
7.4 FUTURE WORK: NEW NANOPARTICLES FOR SENSITIVITY IMPROVEMENT	98
REFERENCES	104
PUBLICATION LIST	112



LIST OF FIGURES

FIGURE 1-1. OPTICAL ABSORBANCE SPECTRA OF GOLD NANOPARTICLES WITH ASPECT RATIOS FROM 1.0 TO 6.5.	6
FIGURE 1-2. (A) TRANSMISSION ELECTRON MICROSCOPY IMAGE OF GOLD NANORODS AFTER SHAPE TRANSITION INDUCED BY LASER IRRADIATION. (B) ABSORBANCE SPECTRA BEFORE AND AFTER LASER IRRADIATION [29].	7
FIGURE 2-1. THE TWO-ENERGY TIME-CONCENTRATION CURVE (SOLID LINE) AND TIC (DOTTED LINE). ...	14
FIGURE 2-2. THE SINGLE-ENERGY TIME-CONCENTRATION CURVE (SOLID LINE) AND TIC (DOTTED LINE).	15
FIGURE 2-3. COORDINATES OF THE MEASUREMENT SYSTEM. THE VESSEL IS LOCATED ALONG THE X-AXIS, THE LASER-BEAM AXIS IS ALONG THE Y-AXIS, AND THE ULTRASONIC-BEAM AXIS IS ALONG THE Z-AXIS.	18
FIGURE 2-4. THE MEASURED BEAM PROFILE (SOLID LINE) OF THE ULTRASOUND TRANSDUCER AND THE FITTED RESULT WITH A GAUSSIAN FUNCTION (DASHED LINE).	18
FIGURE 2-5. SIMULATION RESULTS OF FLOW ESTIMATION USING THE TWO-ENERGY METHOD. (A) CONCENTRATION OF NANORODS AS A FUNCTION OF TIME FOR VELOCITY v EQUAL TO 1 MM/SEC (SOLID LINE) AND FITTED RESULT WITH THE EXPONENTIAL MODEL (DASHED LINE). (B) EXTRACTED FLOW PARAMETER u FROM THE FITTED CURVE VS. THE FLOW VELOCITY v , INDICATING THE LINEAR RELATIONSHIP BETWEEN u AND v	22
FIGURE 2-6. MODELING THE VESSEL AS A SERIES OF COMPARTMENTS OF SIZE (LENGTH) Δx	26
FIGURE 2-7. SCHEMATIC OF THE PHOTOACOUSTIC TIC MEASUREMENTS SYSTEM.	27
FIGURE 2-8. MEASURED PHOTOACOUSTIC SIGNAL AMPLITUDE AS A FUNCTION OF THE CONCENTRATION OF GOLD NANOPARTICLES.	27
FIGURE 2-9. MEASURED TICs AND FITTED RESULTS WITH GAMMA FUNCTION. (A) $V/Q = 14$ SEC. (B) $V/Q = 49$ SEC. (C) $V/Q = 91$ SEC. (D) $V/Q = 113$ SEC. (E) CURVE-FITTED TICs FROM EXPERIMENTAL RESULTS AT VARIOUS FLOW RATES (NORMALIZED).	28
FIGURE 2-10. RESULTS FOR FLOW RATES OF 3, 2.14, 1.2, 0.61, 0.45, 0.33, AND 0.23 ML/SEC. (A) MTT VS. V/Q , (B) τ VS. V/Q	29
FIGURE 2-11. SCHEMATIC OF THE PHOTOACOUSTIC FLOW MEASUREMENT SYSTEM. THE FLOW CONTAINING GOLD NANORODS IS SUPPLIED BY AN INFUSION PUMP. THE LASER IRRADIATION FOR DESTRUCTION/DETECTION IS FROM THE SIDE, AND THE ULTRASONIC TRANSDUCER FOR DETECTION IS AT THE TOP. PVA, POLYVINYL ALCOHOL.	31
FIGURE 2-12. MEASURED PHOTOACOUSTIC SIGNAL AMPLITUDE AS A FUNCTION OF THE CONCENTRATION OF GOLD NANORODS.	31
FIGURE 2-13. THE TICs OF GOLD NANORODS AT ZERO VELOCITY FOR DIFFERENT LASER IRRADIATION ENERGIES.	32

FIGURE 2-14. SAMPLED RAW DATA AND FITTED TICs USING THE TWO-ENERGY METHOD (A) AND SINGLE-ENERGY METHOD (B) AT VARIOUS FLOW VELOCITIES.	33
FIGURE 2-15. EXPERIMENTAL RESULTS OF FLOW ESTIMATION FOR FLOW VELOCITIES OF 0.35, 0.71, 1.42, AND 2.83 MM/SEC. (A) TWO-ENERGY METHOD. (B) SINGLE-ENERGY METHOD. ERROR BARS SHOW STANDARD DEVIATIONS.	34
FIGURE 2-16. (A) DIAGRAM OF THE EFFECTIVE BEAM WIDTH. (B) ESTIMATED RESULTS (TWO-ENERGY METHOD) FOR DIFFERENT EFFECTIVE BEAM WIDTHS.	35
FIGURE 2-17. COMPARISON OF THE EXPERIMENTAL RESULTS BETWEEN THE TWO-ENERGY AND SINGLE-ENERGY METHODS.	36
FIGURE 3-1. DIAGRAM OF MULTIPLE TARGETING OF TWO CANCER CELLS BY USING DIFFERENT NANOPROBES WITH PHOTOACOUSTIC DETECTION AT DIFFERENT WAVELENGTHS.	39
FIGURE 3-2. DIAGRAM SHOWING TARGETING OF TWO TYPES OF NANOPROBES ON CANCER CELL REGION. ONE CAN DIRECTLY TARGET ON ENDOTHELIAL CELLS AT ANGIOGENESIS REGION, THE OTHER PENETRATES THROUGH THE ENDOTHELIAL GAP (EXTRAVASATIONS) TO TARGET IN CANCER CELLS. 41	41
FIGURE 3-3. ABSORPTION SPECTRA OF GOLD NANORODS WITH TWO ASPECT RATIOS: (A) AuNR ₈₀₀ AND (B) AuNR ₁₀₀₀ . THIS FIGURE WAS MEASURED BY PROF. WANG'S LAB IN NATIONAL CHUNG CHENG UNIVERSITY.	42
FIGURE 3-4. WESTERN BLOT ANALYSIS REVEALS OVER EXPRESSION OF HER2 IN OECM1 CELL, EGFR IN CAL27, AND CXCR4 IN BOTH CELLS. THE RESULTS WERE FROM DR. D.-B. SHIEH'S LAB IN NATIONAL CHENG KUNG UNIVERSITY.	45
FIGURE 3-5. ELECTRON MICROGRAPH OF A PORTION OF AN OECM1 CELL TARGETED WITH MIXED NANOPROBES, AuNR ₈₀₀ -ANTIHER2 AND AuNR ₁₀₀₀ -ANTICXCR4, CLEARLY SHOWING THE PRESENCE OF THE GOLD NANORODS (BLACK CYLINDERS) ATTACHED AROUND THE BORDER OF THE CELL. THE RESULTS WERE FROM DR. D.-B. SHIEH'S LAB IN NATIONAL CHENG KUNG UNIVERSITY.	46
FIGURE 3-6. (A) IMAGES OF OECM1 CELLS OBTAINED AT 800 AND 1064 NM. OECM1 CELLS WERE WITH AuNR ₈₀₀ -ANTIHER2, AuNR ₁₀₀₀ -ANTI EGFR, AND AuNR ₈₀₀ (FROM LEFT TO RIGHT) (B) IMAGES OF CAL27 CELLS OBTAINED AT 800 AND 1064 NM. CAL27 CELLS WERE WITH AuNR ₁₀₀₀ -ANTI EGFR, AuNR ₈₀₀ -ANTIHER2, AND AuNR ₁₀₀₀ (FROM LEFT TO RIGHT). THE IMAGES ARE DISPLAYED WITH A DYNAMIC RANGE OF 10 DB.	47
FIGURE 3-7. SCHEMATIC DIAGRAM OF THE EXPERIMENTAL SETUP FOR <i>IN VIVO</i> PHOTOACOUSTIC IMAGING.	48
FIGURE 3-8. IMAGES OF A CAL27 TUMOR BEFORE AND AFTER THE INJECTION OF AuNR ₁₀₀₀ AND AuNR ₁₀₀₀ -ANTI EGFR. ELLIPSES INDICATE THE TUMOR REGIONS. (A) FUSION IMAGES BEFORE/AFTER AuNR ₁₀₀₀ -ANTI EGFR INJECTION AT DIFFERENT TIME POINTS. THE ULTRASOUND IMAGES ARE DISPLAYED ON A GRAYSCALE, AND THE SUPERIMPOSED PHOTOACOUSTIC IMAGES OBTAINED AT AN OPTICAL WAVELENGTH OF 1064 NM ARE DISPLAYED IN RED PSEUDOCOLOR. (B) PHOTOACOUSTIC IMAGES BEFORE/AFTER AuNR ₁₀₀₀ -ANTI EGFR INJECTION SHOWN IN THE SAME	

SCALE. (C) FUSION IMAGES BEFORE/AFTER AuNR₁₀₀₀ INJECTION AT DIFFERENT TIME POINTS. THE ULTRASOUND IMAGES ARE DISPLAYED ON A GRAYSCALE, AND THE SUPERIMPOSED PHOTOACOUSTIC IMAGES OBTAINED AT AN OPTICAL WAVELENGTH OF 1064 NM ARE DISPLAYED IN RED PSEUDOCOLOR. (D) PHOTOACOUSTIC IMAGES BEFORE/AFTER AuNR₁₀₀₀ INJECTION SHOWN IN THE SAME SCALE. ...49

FIGURE 3-9. IMAGES OF OECM1 TUMOR BEFORE AND AFTER THE INJECTION OF AuNR₈₀₀ AND AuNR₈₀₀-ANTIHER2. ELLIPSES INDICATE THE TUMOR REGIONS. (A) FUSION IMAGES BEFORE/AFTER AuNR₈₀₀-ANTIHER2 INJECTION AT DIFFERENT TIME POINTS. THE ULTRASOUND IMAGES ARE DISPLAYED ON A GRAYSCALE, AND THE SUPERIMPOSED PHOTOACOUSTIC IMAGES OBTAINED AT AN OPTICAL WAVELENGTH OF 800 NM ARE DISPLAYED IN RED PSEUDOCOLOR. (B) PHOTOACOUSTIC IMAGES BEFORE/AFTER AuNR₈₀₀-ANTIHER2 INJECTION SHOWN IN THE SAME SCALE. (C) FUSION IMAGES BEFORE/AFTER AuNR₈₀₀ INJECTION AT DIFFERENT TIME POINTS. THE ULTRASOUND IMAGES ARE DISPLAYED ON A GRAYSCALE, AND THE SUPERIMPOSED PHOTOACOUSTIC IMAGES OBTAINED AT AN OPTICAL WAVELENGTH OF 800 NM ARE DISPLAYED IN RED PSEUDOCOLOR. (D) PHOTOACOUSTIC IMAGES BEFORE/AFTER AuNR₈₀₀ INJECTION SHOWN IN THE SAME SCALE.50

FIGURE 3-10. IMAGES OF OECM1 CELLS OBTAINED AT VARIOUS TIME POINTS AFTER INJECTION OF AuNR₈₀₀-ANTIHER2 + AuNR₈₀₀-ANTICXCR4.51

FIGURE 3-11. (A) AVERAGED IMAGE INTENSITIES WITHIN THE TUMOR REGION VERSUS TIME AFTER INJECTIONS WITH AuNR₁₀₀₀-ANTI EGFR (SOLID LINE) AND AuNR₁₀₀₀ (DASHED LINE). (B) AVERAGED IMAGE INTENSITIES WITHIN THE TUMOR REGION VERSUS TIME AFTER INJECTION WITH AuNR₈₀₀-ANTIHER2 (SOLID LINE), AuNR₈₀₀ (DASHED LINE), AND AuNR₈₀₀-ANTIHER2 + AuNR₈₀₀-ANTICXCR4 (DOTTED LINE). THE AVERAGES WERE CALCULATED FROM THREE CROSS-SECTIONAL IMAGES. ERROR BARS INDICATE STANDARD DEVIATIONS.52

FIGURE 3-12. IMAGES OF OECM1 CELLS WITH AuNR₈₀₀ (CONTROL GROUP) AND AuNR₈₀₀-RGD4C INJECTION OBTAINED AT 800 NM. (A) BEFORE AuNR₈₀₀ INJECTION. (B) BEFORE AuNR₈₀₀-RGD4C INJECTION. (C) 4 HOURS AFTER AuNR₈₀₀ INJECTION. (D) 4 HOURS AFTER AuNR₈₀₀-RGD4C INJECTION.53

FIGURE 3-13. IMAGES OF RGD4C-PROBE INJECTION FROM 10 MINUTES TO 4 HOURS AFTER INJECTION. .54

FIGURE 3-14. NORMALIZED PHOTOACOUSTIC INTENSITY WITHIN TUMOR REGION WITH RGD4C PROBES INJECTION VERSUS OBSERVATION TIME.54

FIGURE 3-15. ULTRASOUND AND 800 NM AND 1064 NM PHOTOACOUSTIC IMAGES AT DIFFERENT TIME POINTS AFTER MIXED PROBES INJECTION.55

FIGURE 3-16. NORMALIZED PHOTOACOUSTIC INTENSITY WITHIN TUMOR REGION WITH MIXED PROBES INJECTION VERSUS OBSERVATION TIME. (A) MIXED PROBES INJECTION: AuNR₈₀₀-RGD4C AND AuNR₁₀₀₀-ANTIHER2. (B) MIXED PURE GOLD NANORODS INJECTION: AuNR₈₀₀ AND AuNR₁₀₀₀...56

FIGURE 3-17. HISTOLOGY WITH A SCALE BAR OF 500 MM. EPIDERMIS, DERMIS, SUBCUTIS, FASCIA, AND MUSCULAR LAYERS WERE ON THE TOP OF THE TUMOR.57

FIGURE 4-1. OPTICAL MICROSCOPIC IMAGES OF LIT MEASUREMENTS. THE CELLS WITHIN THE LASER BEAM WERE DYED IN BLUE WITH TRYPAN, INDICATING THE CELLS WERE KILLED BY THE

HYPERTHERMIA CAUSED BY IRRADIATING THE TARGETED NANOPROBES. THE IMAGE WAS FROM PROF. C.-R.-C. WANG'S LAB IN NATIONAL CHUNG CHENG UNIVERSITY.	59
FIGURE 4-2. GRÜNEISEN PARAMETER OF WATER VERSUS TEMPERATURE (SOLID LINE) AND THE LINEAR FIT (DOTTED LINE).....	62
FIGURE 4-3. THE LINEAR RELATION BETWEEN TEMPERATURE AND PHOTOACOUSTIC AMPLITUDE OF GOLD NANOPARTICLES [80].	62
FIGURE 4-4. INTEGRATED SYSTEM WITH PHOTOACOUSTIC IMAGING SYSTEM AND LASER THERMAL THERAPY SYSTEM.	63
FIGURE 4-5. PHOTOACOUSTIC IMAGES OF TUMOR WITH SUBCUTANEOUS INJECTION OF GOLD NANORODS. (A) BEFORE NANORODS INJECTION, CW LASER OFF. (B) BEFORE NANORODS INJECTION, CW LASER ON. (C) AFTER NANORODS INJECTION, CW LASER OFF. (D) AFTER NANORODS INJECTION, CW LASER ON.....	65
FIGURE 4-6. THERMAL IMAGING CALCULATED FROM FIG. 4-5(C) AND (D). THE IMAGES ARE UNDER THRESHOLD BY SIGNAL INTENSITY IN FIG. 4-5(C). COLORBARS SHOW THE TEMPERATURE IN CELSIUS. (A) TEMPERATURE DISTRIBUTION USING PIXEL-TO-PIXEL CALCULATION. (B) TEMPERATURE DISTRIBUTION USING 3-TIMES-3 WINDOW CALCULATION. (C) TEMPERATURE DISTRIBUTION USING 3-TIMES-3 WINDOW CALCULATION.	66
FIGURE 4-7. LOWPASS FILTERED PHOTOACOUSTIC IMAGES OF TUMOR WITH SUBCUTANEOUS INJECTION OF GOLD NANORODS. (A) BEFORE NANORODS INJECTION, CW LASER OFF. (B) BEFORE NANORODS INJECTION, CW LASER ON. (C) AFTER NANORODS INJECTION, CW LASER OFF. (D) AFTER NANORODS INJECTION, CW LASER ON.	67
FIGURE 4-8. THERMAL IMAGING CALCULATED FROM FIG. 4-7(C) AND (D). THE IMAGES ARE UNDER THRESHOLD BY SIGNAL INTENSITY IN FIG. 4-7(C). COLORBARS SHOW THE TEMPERATURE IN CELSIUS. (A) TEMPERATURE DISTRIBUTION USING PIXEL-TO-PIXEL CALCULATION. (B) TEMPERATURE DISTRIBUTION USING 3-TIMES-3 WINDOW CALCULATION. (C) TEMPERATURE DISTRIBUTION USING 3-TIMES-3 WINDOW CALCULATION.	67
FIGURE 4-9. FUSION RESULT OF ULTRASOUND PULSE/ECHO (GRAY) AND PHOTOACOUSTIC (PSEUDO COLOR) IMAGES OBTAINED AT DIFFERENT CONDITIONS. (A) BEFORE INJECTION, CW LASER OFF. (B) BEFORE INJECTION CW LASER ON. (C) 24 HOURS POST INJECTION, CW LASER OFF. (D) 24 HOURS POST INJECTION, CW LASER ON. (E) 24 HOURS POST INJECTION, CW LASER RE-OFF.....	69
FIGURE 4-10. AVERAGED IMAGE INTENSITY AT DIFFERENT CONDITIONS IN FIG. 4-10. CASE (1): BEFORE INJECTION, CW LASER OFF. CASE (2): BEFORE INJECTION CW LASER ON. CASE (3): 24 HOURS POST INJECTION, CW LASER OFF. CASE (4): 24 HOURS POST INJECTION CW LASER ON. CASE (5): 24 HOURS POST INJECTION CW LASER RE-OFF.	70
FIGURE 4-11. THERMAL IMAGE OF TUMOR WITH TARGETED GOLD NANORODS. DOTTED CIRCLE INDICATES THE TUMOR REGION, AND COLORBAR REPRESENTS TEMPERATURE IN CELSIUS. (A) THERMAL IMAGE FROM FIG. 4-9(C) AND (D). (B) THERMAL IMAGE FROM FIG. 4-9(C) AND (E).	70
FIGURE 4-12. PATHOLOGY OF TUMOR [80]. (A) THE NECROSIS OF TUMOR CELLS (RED ARROWS) AND	

PRESERVATION OF THE FIBROBLAST CELLS (YELLOW ARROWS). (B) THE NECROSIS OF TUMOR CELLS (RED ARROWS) AND PRESERVATION OF THE PERIPHERAL FOLLICLES (GREEN ARROWS).....	71
FIGURE 4-13. PATHOLOGY OF TUMOR [80]. (A) TUMOR WITHOUT TREATMENT. (B) TUMOR AFTER TARGETED THERMAL THERAPY.	71
FIGURE 5-1. THE DIAGRAM OF THE ABSORBER AND THE DETECTION POINT FOR SIMULATING THE PHOTOACOUSTIC SIGNAL PROPAGATION.	75
FIGURE 5-2. THE SIMULATION RESULTS OF PHANTOMS OF VARIED ABSORPTION. (A) NORMALIZED ENERGY DEPOSITION OF AN ABSORBER WITH ABSORPTION 20 cm^{-1} . (B) NORMALIZED ENERGY DEPOSITION OF AN ABSORBER WITH ABSORPTION 8 cm^{-1} . (C) NORMALIZED ENERGY DEPOSITION OF AN ABSORBER WITH ABSORPTION 2 cm^{-1} . (D) ENERGY DEPOSITION PROFILES ALONG THE DASHED LINES IN (A), (B), AND (C). (E) PROPAGATED PHOTOACOUSTIC SIGNALS DETECTED BY USING FORWARD MODE. (F) FREQUENCY SPECTRUMS OF THE THREE ABSORBERS IN FORWARD MODE. (G) PROPAGATED PHOTOACOUSTIC SIGNALS DETECTED BY USING BACKWARD MODE. (H) FREQUENCY SPECTRUMS OF THE THREE ABSORBERS IN BACKWARD MODE.	75
FIGURE 5-3. THE SIMULATION (FORWARD MODE) RESULTS OF PHANTOMS OF VARIED ABSORPTION. (A) PHOTOACOUSTIC SIGNALS DETECTED BY HYDROPHONE. (B) FREQUENCY SPECTRA OF THE PHOTOACOUSTIC SIGNALS. (C) PEAK FREQUENCIES, -6 dB, AND -20 dB BANDWIDTHS VS. ABSORPTION COEFFICIENTS.	77
FIGURE 5-4. THE DIAGRAM OF EXPERIMENTAL SETUP FOR PHOTOACOUSTIC IMAGING. (A) PHANTOM MANUFACTURE. (B) FORWARD MODE. (C) BACKWARD MODE.	77
FIGURE 5-5. THE EXPERIMENTAL (FORWARD MODE) RESULTS OF PHANTOMS OF VARIED ABSORPTION. (A) PHOTOACOUSTIC SIGNALS DETECTED BY HYDROPHONE. (B) FREQUENCY SPECTRA OF THE PHOTOACOUSTIC SIGNALS. (C) PEAK FREQUENCIES, -6 dB, AND -20 dB BANDWIDTHS VS. ABSORPTION COEFFICIENTS.	79
FIGURE 5-6. THE EXPERIMENTAL (BACKWARD MODE) RESULTS OF PHANTOMS OF VARIED ABSORPTION. (A) PHOTOACOUSTIC SIGNALS DETECTED BY HYDROPHONE. (B) FREQUENCY SPECTRA OF THE PHOTOACOUSTIC SIGNALS. (C) PEAK FREQUENCIES, -6 dB, AND -20 dB BANDWIDTHS VS. ABSORPTION COEFFICIENTS.	79
FIGURE 5-7. (A) IMAGE OF AGAR PHANTOM WITH ABSORPTION COEFFICIENTS 41.75 cm^{-1} (LEFT) AND 5.01 cm^{-1} (RIGHT), RESPECTIVELY. (B) FREQUENCY (MAGNITUDE) SPECTRUMS OF THE PHOTOACOUSTIC SIGNALS OF EACH LINE. (C) THE PEAK FREQUENCIES OF EACH LINE. (D) FREQUENCY (MAGNITUDE) SPECTRUMS OF THREE FILTERS FOR SUBBAND IMAGES.	80
FIGURE 5-8. SUBBAND IMAGES EXHIBITED BY USING PSEUDO-COLORS. (A) BAND 0-7 MHz. (B) BAND 7-14 MHz. (C) BAND 14-21 MHz. (D) COMBINATION IMAGE OF SUBBAND IMAGES.	81
FIGURE 5-9. LATERAL PROJECTIONS OF SUBBAND IMAGES. (A) BAND 0-7 MHz. (B) BAND 7-14 MHz. (C) BAND 14-21 MHz.	81
FIGURE 5-10. THE OPTIMAL CONTRAST WEIGHTING SUMMATION PROCESS.	83
FIGURE 5-11. (A) SUMMED IMAGE WITH EQUAL WEIGHTING. (B) SUMMED IMAGE WITH OPTIMAL	

WEIGHTING. (C) LATERAL PROJECTIONS OF THE ORIGINAL IMAGE, EQUAL WEIGHTING IMAGE, AND OPTIMAL WEIGHTING IMAGE, RESPECTIVELY.....	83
FIGURE 5-12. PEAK FREQUENCIES VS. VARIOUS ABSORPTIONS BY FORWARD MODE AND BACKWARD MODE, RESPECTIVELY.....	84
FIGURE 5-13. SIMULATION RESULTS FOR FREQUENCY ANALYSIS. (A) ABSORPTION COEFFICIENT DISTRIBUTION. (B) RECEIVED PHOTOACOUSTIC IMAGE. (C) AVERAGED FREQUENCY BY WAVELET ANALYSIS. (D) AVERAGED FREQUENCY BY HHT ANALYSIS.	85
FIGURE 5-14. MULTIPLYING IMAGE OF SUBBAND IMAGE AND AVERAGED FREQUENCY IMAGE.....	86
FIGURE 5-15. SIMULATION RESULTS OF ABSORBERS WITH DIFFERENT OPTICAL ABSORPTIONS. (A) ABSORPTION COEFFICIENT DISTRIBUTION. (B) AVERAGED FREQUENCY BY HHT ANALYSIS. (C) AVERAGED FREQUENCY VS. ABSORPTION COEFFICIENT.	87
FIGURE 5-16. SIMULATION RESULTS OF ABSORBERS WITH DIFFERENT THICKNESS. (A) ABSORPTION COEFFICIENT DISTRIBUTION. (B) AVERAGED FREQUENCY VS. THICKNESS.....	87
FIGURE 6-1. THE RELATION BETWEEN CELL VIABILITY (NORMALIZED TO THE CONTROL) AND THE CONCENTRATION OF BIOCONJUGATED GOLD NANORODS. THE RESULTS WERE FROM DR. D.-B. SHIEH'S LAB IN NATIONAL CHENG KUNG UNIVERSITY.....	90
FIGURE 6-2. <i>IN VITRO</i> BIOSAFETY ANALYSIS OF THE AU NANORODS. THE ANALYSIS WAS PERFORMED USING MTT ASSAY IN HUMAN UMBILICAL VEIN ENDOTHELIAL CELL (HUVEC) LINE. (A) CELLS REACTED WITH AuNR ₈₀₀ AND AuNR ₈₀₀ -ANTIHER2. (B) CELLS REACTED WITH AuNR ₁₀₀₀ AND AuNR ₁₀₀₀ -ANTI EGFR. THE RESULTS WERE FROM DR. D.-B. SHIEH'S LAB IN NATIONAL CHENG KUNG UNIVERSITY.	91
FIGURE 6-3. <i>IN VITRO</i> BIOSAFETY ANALYSIS OF THE AU NANORODS. THE ANALYSIS WAS PERFORMED USING MTT ASSAY IN OECM1 AND CAL27 CELL LINES WITH A NUMBER OF 5,000 CELLS. THE TEST TIME WAS 24 HOURS (A) OECM1 CELLS REACTED WITH AuNR ₈₀₀ AND AuNR ₈₀₀ -ANTIHER2. (B) OECM1 CELLS REACTED WITH AuNR ₁₀₀₀ AND AuNR ₁₀₀₀ -ANTI EGFR. (C) CAL27 CELLS REACTED WITH AuNR ₈₀₀ AND AuNR ₈₀₀ -ANTIHER2. (D) CAL27 CELLS REACTED WITH AuNR ₁₀₀₀ AND AuNR ₁₀₀₀ -ANTI EGFR. THE RESULTS WERE FROM DR. D.-B. SHIEH'S LAB IN NATIONAL CHENG KUNG UNIVERSITY.	91
FIGURE 6-4. HEMOLYSIS ASSAY RESULTS. HUMAN BLOOD WAS MIXED WITH AuNR ₈₀₀ OF DIFFERENT CONCENTRATION. THE EXPERIMENTAL GROUPS WERE IRRADIATED BY LASER PULSES AT 800 NM WITH AN ENERGY DENSITY OF 40 MJ/CM ² PER PULSE. THE IRRADIATION TIME WAS 1 MINUTE (ABOUT 600 PULSES). THREE SAMPLES WERE PERFORMED FOR EACH CASE TO OBTAIN THE AVERAGE AND STANDARD DEVIATION. THE RESULTS WERE FROM DR. D.-B. SHIEH'S LAB IN NATIONAL CHENG KUNG UNIVERSITY.	92
FIGURE 6-5. <i>IN VIVO</i> SYSTEMIC TOXICITY ANALYSIS REVEALED THAT ALL TEST ANIMALS SURVIVED THE TWO MONTHS EVALUATION PERIOD OF TIME. (A) MICE INJECTED WITH AuNR ₈₀₀ . (B) MICE INJECTED WITH AuNR ₁₀₀₀ . THE RESULTS WERE FROM DR. D.-B. SHIEH'S LAB IN NATIONAL CHENG KUNG UNIVERSITY.....	92

FIGURE 6-6. ATOMIC ABSORPTION SPECTROSCOPY ANALYSIS OF ORGANS TAKEN FROM TEST MICE AT DIFFERENT TIME PERIOD AFTER INTRAVENOUS INJECTION. THE RESULT REVEALED THAT THESE NANORODS WERE MAINLY ACCUMULATED IN THE SPLEEN AND LIVER AND COULD BE CLEARED AFTER 168 HOURS. THE RESULTS WERE ACCOMPLISHED BY DR. D.-B. SHIEH'S LAB IN NATIONAL CHENG KUNG UNIVERSITY..... 93

FIGURE 7-1. SCHEMATIC DIAGRAM REPRESENTING THE ASYMMETRIC SYNTHESIS OF AuNR@SiO₂ OR NANODUMB BELLS GOLD/SILVER NANOPARTICLES. THIS SYNTHESIS PROCESS WAS FROM PROF. C.-R.-C. WANG'S LAB IN NATIONAL CHUNG CHENG UNIVERSITY. 99

FIGURE 7-2. DIAGRAMS OF DIFFERENT AuNR SAMPLES..... 99

FIGURE 7-3. TEM IMAGES OF NEW AuNR PARTICLES. THE IMAGES WERE FROM PROF. C.-R.-C. WANG'S LAB IN NATIONAL CHUNG CHENG UNIVERSITY..... 100

FIGURE 7-4. PHOTOACOUSTIC EXPERIMENTAL SETUP FOR TESTING NEW PARTICLES. 101

FIGURE 7-5. PHOTOACOUSTIC IMAGES OF DIFFERENT SAMPLES. UP TO BOTTOM: WATER, AuNR-PEG IN PBS, Ag@AuNR PNP, Au@AuNR PNP, AND AuNR@SiO₂. 101

FIGURE 7-6. PHOTOACOUSTIC INTENSITY WITHIN THE TUBE OF DIFFERENT SAMPLES. 102

FIGURE 7-7. NORMALIZED PHOTOACOUSTIC INTENSITY OF AuNR-PEG AND AuNR@SiO₂ VS. TIME. .. 103



LISTS OF TABLES

TABLE 1-1. THE ABSORPTION COEFFICIENTS OF MAIN CONSTITUTIONS OF BIOLOGICAL TISSUES UNDER NEAR-INFRARED RANGE [40].	9
TABLE 7-1. THE PROPERTIES OF PIEZOELECTRIC MATERIALS.	98

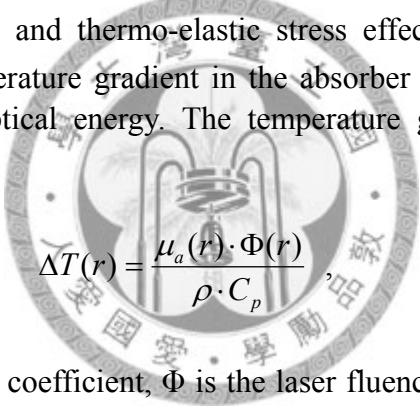


CHAPTER 1 Introduction

1.1 Photoacoustic imaging

Photoacoustic imaging is a newly developed imaging technique that has been used to image the optical properties of biological tissues in recent decades. Generation of photoacoustic signal is described as follows. First, a short laser pulse illuminates an image object (e.g., tissue of interest), heats the object due to absorption, and consequently, by means of thermoelastic expansion, generates an acoustic signal in megahertz frequency range that can be detected using an ultrasonic transducer [1, 2].

There are mainly two physical phenomena involved in photoacoustic generation: photo-thermal mechanism and thermo-elastic stress effect [1, 3]. The former one refers to the instant temperature gradient in the absorber to be observed due to the absorption of incident optical energy. The temperature gradient $\Delta T(r)$ generated within the object is


$$\Delta T(r) = \frac{\mu_a(r) \cdot \Phi(r)}{\rho \cdot C_p}, \quad (1-1)$$

where μ_a is the absorption coefficient, Φ is the laser fluence, ρ represents the density of the object, and C_p represents the heat capacity at constant pressure. If the laser temporal profile is represented as $\eta(t)$, laser fluence becomes

$$\Phi(r, t) = \Phi(r) \cdot \eta(t), \quad (1-2)$$

and

$$\Delta T(r, t) = \frac{\mu_a(r) \cdot \Phi(r, t)}{\rho \cdot C_p}. \quad (1-3)$$

Thermo-elastic effect describes the production of acoustic waves from elastic stress of the observed object due to the heat expansion. After the resulting laser fluence and the further temperature gradient, wave equation was applied to achieve the photoacoustic pressure:

$$\frac{\partial^2 \varphi}{\partial t^2} - c_s^2 \nabla^2 \varphi = c_s^2 \beta \Delta T = \frac{c_s^2 \beta}{\rho C_p} \mu_a(r) \Phi(r, t). \quad (1-4)$$

where β is the thermal volume expansion coefficient, c_s is the speed of sound, and φ is the scalar potential of velocity field. By substituting the pressure $P(r, t)$ as

$$P(r, t) = -\rho \frac{\partial \varphi(r, t)}{\partial t}, \quad (1-5)$$

equation (1-4) can be rewritten as

$$\nabla^2 P - \frac{1}{c_s^2} \frac{\partial^2 P}{\partial t^2} = -\frac{\beta}{C_p} \frac{\partial (\mu_a(r) \Phi(r, t))}{\partial t}. \quad (1-6)$$

Then, the pressure can be solved as

$$P(r, t) = \frac{\beta}{4\pi C_p} \int_V \frac{\mu_a(r_0) \Phi(r_0) \frac{\partial \eta(t_0)}{\partial t_0} \Big|_{t_0 = t - \frac{|r-r_0|}{c_s}}}{|r-r_0|} dr_0. \quad (1-7)$$

1.2 Photoacoustic imaging in biomedical applications

High optical contrast in photoacoustic imaging makes it a useful tool for visualization of not only morphological distribution of optical absorption, but also functional and dynamic biological processes which result in changes of photoacoustic signals. Photoacoustic imaging has been used for obtaining structural morphological information of biological tissues, such as epidermal melanin measurement [4], vascular distribution [5], and tumor detection [2, 6]. The applications of photoacoustic functional imaging include blood oxygenation monitoring, blood flow velocity measurement, and temperature changes recording during laser irradiation. Esenaliev et al. built a photoacoustic system for noninvasive and continuous monitoring the cerebral venous oxygenation in real-time [7]. The photoacoustic signal amplitude was measured linearly correlated with the blood oxygenation in the wide range from 24% to 92%. They also mentioned how to measure the absolute value of blood oxygenation at different hemoglobin using two-wavelength photoacoustic system, from which the concentrations of oxyhemoglobin and deoxyhemoglobin at two wavelengths can be

obtained. This model has also been used by Laufer et al. for quantitative measurement of tissue chromophores or targeted contrast agent [8]. A functional photoacoustic microscopy system by Zhang et al. was developed for *in vivo* imaging of angiogenesis, hemoglobin oxygen concentration [5]. Quantitative mapping of hemoglobin oxygen can be obtained from correlation calculation of the image intensity at four wavelengths. The functional image helps to distinguish arterioles and venules that are hard to discriminate from only structural images.

Cancer remains a mainly cause of death today. The different optical properties of cancerous and normal tissues make photoacoustic technique a promising tool for early detection of tumor. Some groups have developed photoacoustic mammography system to detect tumor deeply embedded in scattered tissues with phantom studies [2, 6]. The developed system is capable of detecting a tumor-like object with 2 mm in diameter at depth of 60 mm in a scattered tissue phantom [2].

Some other groups have used targeted contrast agent that can bind at tumor site for an enhanced contrast [9, 10]. The targeted contrast agents, also called nanoprobes, are usually formed with nanoparticles of high optical absorption and some affinity ligands, such as antibody or peptides. Nanoprobes are able to bind at tumor site through the antibody-antigen specific binding at the surface of the tumor [9-11], or peptide-integrins binding at angiogenesis [12]. The targeted contrast agents not only help to recognize the location and geometry of cancerous tissues, but also provide molecular profiles indicating the expressions of oncogenes, which is useful for better diagnosis and more effective treatment.

Small animal models play an indispensable part of modern pre-clinical researches, including cancer research, drug development, and molecular biology. Every year, tens of million mice were bred and used for biologic researches. Therefore, a non-invasive imaging system with high resolution and high sensitivity is needed for small animal model experiments to shorten the development period of research and reduce the used number of small animals. There are several reasons why photoacoustic imaging system is a promising modality for obtaining structural, functional, and molecular information in small animal studies. First, the spatial resolution level of photoacoustic imaging is sub-millimeter as high frequency ultrasonic micro imaging system, which is advantaged to existing imaging modalities, such as PET (positron emission tomography) and X-ray. Second, photoacoustic imaging system can be directly combined with ultrasonic micro imaging system for obtaining multi-modality imaging providing variable information. Third, the high optical contrast according to difference of optical absorption makes photoacoustic

imaging a more suitable tool to distinguish different tissues. Forth, use of nanoparticles extends the capability of photoacoustic imaging to functional and molecular imaging for small animal *in vivo* studies as mentioned in last section.

Lao et al. have used photoacoustic techniques to visualize the subcutaneous vasculature or angiogenesis at tumor region in mice [13] for early detection of pathological changes. Wang's systems revealed the blood vessels as well as detailed brain structures based on the intrinsic optical contrast between blood and brain tissues [14, 15] and also exogenous photoacoustic contrast agents, including nanoshells [16] and optical dye indocyanine green (ICG) [17]. The brain structures in photoacoustic images with skin and skull intact well match that in the open-skull histological photography. The spatial resolution of these systems can achieve about 60 μm [14] and the optical absorption in the blood vessel can increase 100% after administrating nanoshell with a concentration of 1010 particles per milliliter [16]. The functional imaging of the rat brain was also obtained with the system [15]. The cerebral cortex activities of left and right brain were found different from the photoacoustic image during stimulation at different side of whisker [15]. The hemodynamic changes in the brain vessel corresponding to the whisker stimulation result in changes of optical absorption that can be detected by the photoacoustic imaging system.

Recently, 3D imaging systems have been developed to obtain more complete information of object that 2D imaging system can only capture planar slices of it. Also, the geometry and location of objects of interest can be recognized more precisely. 3D whole-body photoacoustic tomography of mice has also been developed [18]. The system can achieve a spatial resolution better than 600 μm , and visualize superficial vasculature, blood vessels, and organs if near-infrared wavelengths (755 nm and 1064 nm) are applied. A photoacoustic 3D volume of 10 mm thick abdominal section of a mouse has been imaged to reveal several organs and big vessels.

1.3 Gold nanoparticles

Gold nanoparticles coupled with biomolecules have been used for biological labeling, imaging and assays [19]. In immunoassay systems, many current diagnostic kits have been developed utilizing the interactions between antibody conjugated gold nanoparticles and their antigens [20, 21]. Recently, gold nanoparticles coupling with DNA single or double strains have shown great potentials for gene delivery and detecting unknown gene sequences [22]. Also, the use of the nanoparticles for imaging

has been also demonstrated because of the excellent contrast of gold nanoparticles under an electron microscope [23]. There are several technical advantages of using gold nanoparticles for biological labeling, imaging and assays. First, the sizes of gold nanoparticles are comparable to those of small molecules, short peptides and DNA sequences. Therefore, they can be easily coupled with those materials to produce new nanoparticles with dual or multiple biological functions. For example, the gold nanoparticles coupled with carbohydrate molecules have shown that they can be applied to identify the binding site of a specific protein on the pili of *E. coli* [24]. Second, a single nanoparticle with large surface volume ratio is suitable for the covalent attachment of multiple ligands, which may generate a strong binding affinity between the nanoparticle conjugates and the specific binding target [25]. Third, the gold nanoparticles exhibit an intense color in visible region for spectroscopic detection and also great contrast for imaging so that they can be applied for many new biological labeling and imaging purposes. Finally, gold nanoparticles are biologically compatible so that they are safe when used for biological detecting or imaging.

The strong optical response from the visible to infrared spectral region ought to be taken notice on in photoacoustic imaging. The molar absorptivity of a 20 nm nanospheres (8.1×10^{-17} gram per particle) is of the order of $10^9 \text{ cm}^{-1}\text{M}^{-1}$ and increases to $10^{11} \text{ cm}^{-1}\text{M}^{-1}$ as the volume of the particle increases [26, 27]. As a reference, the indocyanine green, which is an optical dye with molecular weight of about 775 Dalton (1.3×10^{-21} gram per molecule), has molar absorptivity small than $10^6 \text{ cm}^{-1}\text{M}^{-1}$ [27]. Therefore, gold nanoparticles effectively assist generation of photoacoustic signals. In photoacoustic imaging, gold nanoparticles have been used for contrast enhancement for tumor detection [27] and rat brain imaging [16].

1.3.1 Shape-dependent optical properties

The absorption of spherical gold nanoparticles have shown that the peak optical absorption red-shifts with the increasing particle size. In general, gold nanospheres with diameters of tens of nanometers exhibit absorption peak at around 550 nm [28]. For gold nanorods (i.e., cylindrical gold nanoparticles, AuNR), the wavelength of peak absorption only weakly depends on the diameter of gold nanoparticle. Generally, the wavelength with maximal absorption increases significantly with the aspect ratio (defined as the ratio of the length of the major axis to that of the minor axis). The absorption spectrum of gold nanorods has two distinct peaks. One absorption peak is determined by the length of the minor axis at around 550 nm, which is similar to the absorption peak of gold nanospheres. The other one is red-shifted from the first peak

and strongly depends on the aspect ratio. The two absorption peaks are called the transverse band and the longitudinal band, respectively [28]. In general, the magnitude of the longitudinal band is more pronounced than that of the transverse band and the wavelength range of the former is mostly used in the applications of gold nanorods. The peak wavelength λ_{\max} of the longitudinal band can be related to the aspect ratio R by [28]

$$\lambda_{\max} = (33.34 \cdot R - 46.31) \cdot \varepsilon_m + 472.31, \quad (1-8)$$

where ε_m is the dielectric constant of the surrounding medium. Fig. 1-1 shows that the absorbance peak wavelength is red-shifted from 550 nm to 1050 nm by increasing the aspect ratio from 1.0 to 6.5 [26, 29]. The longitudinal bands are red-shifted as the aspect ratio increases. Thus, irradiation of laser at wavelength corresponding to the peak absorption results in the maximal absorption cross-section and thus the maximal photoacoustic signal. Hence, the photoacoustic signals can be generated effectively and gold nanorods can be potentially used as a photoacoustic contrast agent.

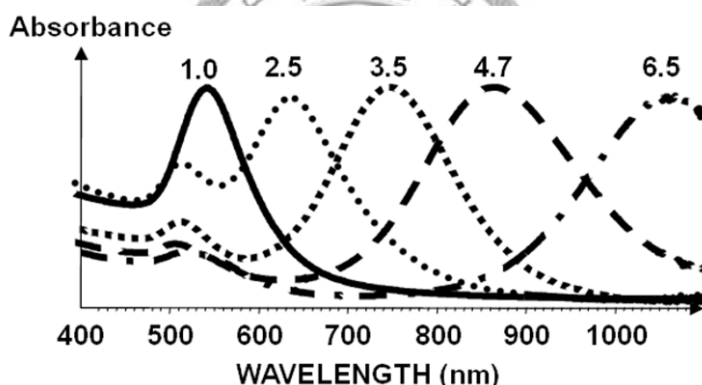


Figure 1-1. Optical absorbance spectra of gold nanoparticles with aspect ratios from 1.0 to 6.5.

1.3.2 Shape transition of gold nanorods

The other important characteristic of gold nanorods is the photo-induced shape transition, whereby stimulation with laser pulses of sufficiently high energy results in a shape transition from nanorods into spheres or other transitional shapes [29]. Fig. 1-2(a) shows the transmission electron microscopy image of a sample after a single laser pulse of 42.5 mJ/cm^2 is applied. It is shown that a portion of the gold nanorods becomes spheres and the other becomes transitional shapes [9, 29]. The shape transition results in a decrease at the optical absorption wavelength shown in Fig. 1-2(b) and the decrease of photoacoustic signal intensity at the same wavelength λ .

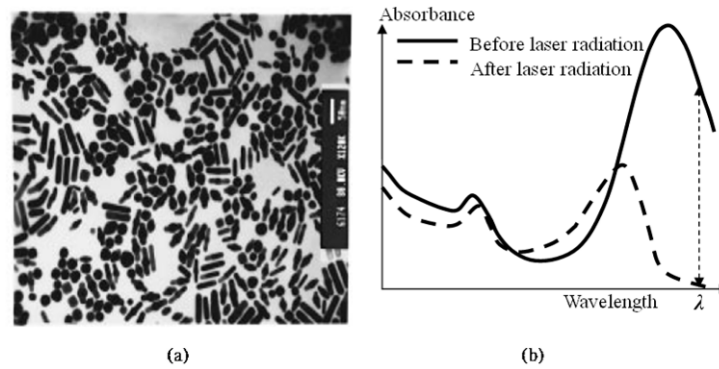


Figure 1-2. (a) Transmission electron microscopy image of gold nanorods after shape transition induced by laser irradiation. (b) Absorbance spectra before and after laser irradiation [29].

1.4 Objectives

In this thesis, gold nanoparticle assisted photoacoustic techniques have been used for achieving functional and molecular imaging in biomedical researches. Specifically, functional imaging refers to quantitatively velocity measurement of the blood flow, which plays an important role in diagnosis of cardiovascular diseases. As for molecular imaging, molecular probes with specific targeting to certain biomarkers on cell surface were used for detection of the biological processes and interactions in living tissues or organs at molecular level. The targeted probes can be non-invasively sensed by an imaging system. It has a great potential for the early detection and more effective treatment of diseases, because aberrations at the cellular and molecular levels occur much earlier than anatomic changes. Molecular imaging methods have developed for many different imaging modalities. X. Gau et al. have developed nanoprobe based on semiconductor quantum dots for cancer targeting and fluorescence imaging in living mice [30]. For ultrasound imaging, microbubbles targeted to $\alpha_v\beta_3$ -integrins expressed on the endothelium cells were used for imaging angiogenesis [31]. L. Josephson et al. have showed that peptide-conjugated magnetic nanoparticles can target lymph nodes and be the MR contrast agent [32]. Furthermore, S. R. Cherry mentioned that several groups have considerable success in small animal imaging by using nuclear imaging system including PET and SPECT with the assist of radionuclides-labeled probes [33].

1.4.1 Quantitative photoacoustic flow estimation

Conventional ultrasound-based flow estimation techniques utilize the Doppler

effect to detect the frequency change of echoes backscattered from the moving blood [34]. However, application of these techniques is generally limited by the difficulty of obtaining the beam-to-flow angle [35]. In the present study, contrast agents that are used in imaging modalities to enhance the desired signal from blood were applied to the measurement of blood flow parameters according to the measurements of signal amplitude (signal intensity, or contrast agent concentration) as a function of time, which is called the time-intensity curve (TIC) [36-38]. The use of an appropriate photoacoustic contrast agents was required to assist in the quantitative flow measurements based on TIC analysis.

In this thesis, gold nanorods are used to assist in building photoacoustic functional and molecular imaging as contrast agents with multiple functions. Specifically, functional imaging refers to quantitatively velocity measurement of the blood flow using destruction-replenishment methods. It exploits the laser-induced shape transformation properties of the gold nanorod and the following wash-in of new nanorods to extract the flow velocity related parameters from the recorded photoacoustic signals. The wash-in analysis is used to avoid limitations of wash-out analysis and provides an alternative technique for blood flow estimation and perfusion assessment.

1.4.2 Photoacoustic molecular imaging and targeted thermal therapy using bioconjugated gold nanorods

Targeting cancer cells helps to determine the expressions of oncogenic surface molecules, which will aid the prediction of clinical outcomes and treatment responses. For this it is necessary to image cancer lesions and obtain pathogenic information on them at the molecular level. However, most previous researches reported in the literature have employed only a single target. Therefore, the goal was to realize photoacoustic imaging with simultaneous multiple selective targeting for cancer diagnosis. The feasibility of the photoacoustic imaging on tumor targeting will be tested *in vitro* and *in vivo* on small-animal models. Moreover, a photothermal therapy for cancer cells without harming surrounding normal tissues can be achieved with the local heating from the targeting gold nanoparticles [39]. However, there is no effective method for monitoring the tissue temperature during thermal-therapy to avoid normal tissue damage and to record the temperature rise on cancer cells.

Bioconjugated gold nanorods with specific targeting to certain biomarkers on cell surface were used for detection of the biological processes and interactions in living

tissues or organs at molecular level. Multiple selective targeting is the goal for obtaining functional perfusion information and pathogenic information at the molecular level for cancer diagnosis on small animal model. Also, photo-thermal system of targeted thermal therapy on cancer cells will be developed and combined with photoacoustic imaging system. The goal is to monitor the temperature rise during thermal therapy via the recorded photoacoustic signals.

1.4.3 Subband imaging for contrast improvement

In previous works, gold nanoparticles had been used to increase the contrast in optical absorption (i.e., contrast agent) in phantom and in in-vitro studies, which include flow estimation and tumor targeting for molecular imaging. For *in vivo* studies, however, the absorption and the optical scattering of biological tissues will decrease the sensitivity of detecting the contrast agent (i.e., gold nanoparticles). Here the influence of the optical absorption of the tissue is focused and discussed. Table 1 lists the absorption coefficients of several constitutions of biological tissues under the near-infrared wavelength range [40]. It can be seen that, in Table 1, most tissues have absorption coefficients lower than 10 cm^{-1} , except for epidermis at 800 nm and deoxyhemoglobin (Hb) at 960 nm. Epidermis has thickness less than 1.5 mm [41] and is away from regions to be observed with contrast agent (e.g., vessel or tumor), so the interference of epidermis will not be conspicuous. As for Hb, a wavelength in which the absorption coefficient of Hb is less than 10 cm^{-1} (e.g., 1064 nm) can be chosen for imaging. Therefore, the contrast agent can enhance the photoacoustic signals if their absorption coefficients are larger than 10 cm^{-1} .

Table 1-1. The absorption coefficients of main constitutions of biological tissues under near-infrared range [40].

Tissue	Epidermis	Dermis	HbO ₂			Hb		
Wavelength (nm)	800		810	960	1064	810	960	1064
Absorption (cm ⁻¹)	40	2.3	4.5	2.84	3.0	4.5	16.8	0.3

Tissue	Whole blood (Oxygenation > 98%)						Fat	
							Subcutaneous	Abdominal
Wavelength (nm)	810	865	910	965	1010	1064	1064	
Absorption (cm ⁻¹)	6.5	7.2	8.9	9.3	8.3	5.6	2.6	3.0

A subband based method that can further enhance the contrast between the contrast agent and the tissue is proposed. The absorption difference not only determines

the contrast but also results in various frequency components, which can be employed to suppress the tissue signal. When laser irradiates on the optical absorber, the energy is absorbed and decays with the distance from the irradiation. It can be comprehended that the laser energy decays more rapidly if the absorber has a higher absorption. The decay profile along the depth infers the pressure distribution, which forms the acoustic waveform to propagate outward. As a result, the propagated photoacoustic signal from object with higher absorption will contain higher frequency portions since the pressure waveform which decays rapidly represents higher frequency. Thus, the photoacoustic signal can be detected by a wideband detector and its frequency spectrum can be divided into several subbands. The contrast can be enhanced by choosing the subbands in which the frequency components of the object with higher absorption are larger than those with lower absorption.

1.5 Organization of the dissertation

This thesis is organized as follows. Quantitative photoacoustic blood flow velocity measurements using time-intensity curve based methods are presented in Chapter 2. Principle derivations of the mathematic models and phantom experiments of both wash-out and wash-in analyses with the assist of gold nanoparticles were performed. The measurement results by using different methods were compared. In Chapter 3, bioconjugated gold nanorods are utilized to demonstrate multiple targeting on cancer in photoacoustic. Biomolecules including antibody and peptide were conjugated on gold nanorods with different absorption spectra to form multiple nanoprobe, which were able to bind on cancer cells and angiogenesis. Photoacoustic molecular imaging was demonstrated in both *in vitro* cell culture and *in vivo* small animal experiments. In Chapter 4, the targeted gold nanorods are used as an optical absorber for targeted thermal therapy of the cancer. A photothermal therapy system was integrated with the photoacoustic imaging system. Also, a photoacoustic method that can monitor the temperature changes during thermal therapy was developed for safety and efficacy concern. Phantom and *in vivo* small animal studies were performed to obtain the quantitative thermal imaging. Chapter 5 describes a subband imaging method for enhance the contrast in photoacoustic images. The method utilizes the relation of higher optical absorption producing higher frequency photoacoustic waveform, and it helps to improve the sensitivity for detection of biological tissues with photoacoustic contrast agents (i.e., gold nanoparticles). Numerical simulations and phantom experiments were performed to verify the

absorption-frequency relation and contrast enhancement with subband imaging. Laser safety regulation and biocompatibility of gold nanoparticles are discussed in Chapter 6. Also, a new type of gold nanoparticle is introduced to enhance the photoacoustic response and better detection sensitivity for *in vivo* studies. This thesis concludes in Chapter 7 with future works described.



CHAPTER 2 Time-intensity CURVE BASED QUANTITATIVE FLOW ESTIMATION

In this chapter, photoacoustic methods for quantitative blood flow estimation will be described. In particular, gold nanoparticles are used as the contrast agent for signal enhancement and for TIC measurements. To obtain the concentration of the gold nanoparticles as a function of time, the photoacoustic signal amplitude of gold nanoparticles has to be linearly proportional to the concentration. The amplitude-concentration relation will be verified by experiments prior to flow estimation. In general, there are two types of TICs: wash-out TIC and wash-in TIC, with which the “wash-out” and “wash-in” characteristics of the contrast agent are utilized for flow estimation. Mathematical models based on the indicator-dilution theory for the TICs are derived and used for fitting the curves obtained from simulations and phantom experiments.

2.1 Time intensity curve for flow estimation

When nanoparticles are added into a flowing fluid (e.g., blood in a vessel), dilution of these particles can be modeled by the indicator-dilution theory [42]. Typically a mixing chamber is included with an input vessel and an output vessel. With this model, the wash-out TIC is measured at the output end of the chamber with the input being a bolus injection. Generally the dilution process is assumed homogeneous and instant and the chamber is modeled as a linear and time-invariant system with a transfer function relating the input and output concentration of indicator (i.e., contrast agent) [43]. Under the bolus injection assumption (i.e., impulse input), it has been found that the flow rate can be derived from the wash-out TIC [37, 42]. If the contrast agent is not injected in a bolus (i.e., a Dirac delta function), deconvolution of the injection rate (as a function of time) may be necessary [38].

If the contrast agent is somehow destructible, it is also possible to measure the wash-in TIC [44]. This technique overcomes the difficulty of ensuring a bolus injection of contrast agent for wash-out analysis in practice. The flow rate of a chamber over the chamber volume or the flow velocity at a specific cross section of a

vessel can be estimated if a constant initial concentration of the contrast agent is achieved in the flow system. For example, ultrasonic microbubble contrast agents can be destroyed by a high-pressure ultrasonic pulse within a certain region of the circulation, with the subsequent replenishment of new contrast agent being monitored by observing the backscattered signals as a function of time [45]. The replenishment rate (i.e., wash-in rate) is highly correlated with the flow velocity, and thus it is feasible to use wash-in TIC with ultrasound to measure flow velocities [44-46].

A two-energy wash-in method was first proposed for estimating the flow velocity that exploits the shape transition property of gold nanorods to measure their wash-in TIC in a photoacoustic modality. This method employs a depletion step followed by a replenishment/observation step, as shown in Fig. 2-1. The solid and dotted lines represent the concentration and the intensity curves, respectively. First, in the depletion step, several consecutive high-energy laser pulses at a wavelength near the peak absorption wavelength are used to induce the shape transition process turning a portion of nanorods into other shapes (and thus reduce the effective concentration of gold nanorods with the original shape) [29]. The shape transition of the gold nanorods decreases the optical absorption at the laser wavelength, and can be considered as “being destroyed” as in the use of microbubbles as a contrast agent in ultrasound imaging. Then, in the replenishment/observation step, laser pulses of the same wavelength but with an energy that is sufficiently low so as not to destroy the gold nanorods are used to induce the photoacoustic signal for measuring the TIC as new gold nanorods “wash-in” the region of interest. Because the photoacoustic signal amplitude increases with the concentration of gold nanorods, the TIC reflects the replenishment process of gold nanorods as determined by the flow rate. The linearity of the relationship between concentration and acoustic amplitude has been established [47], and this was tested experimentally in the present study. Finally, fitting the TIC with an exponential model can extract a parameter (in the exponential model) that is highly correlated with the flow velocity.

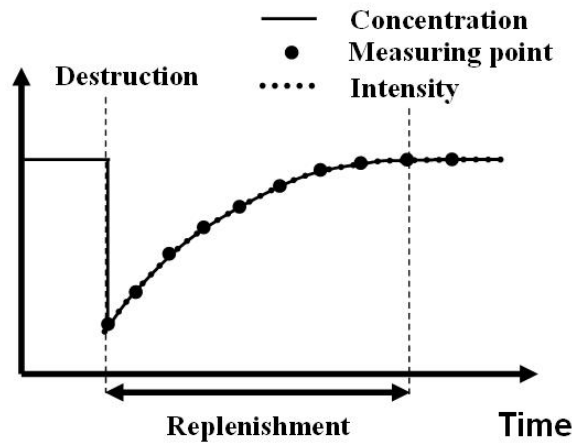


Figure 2-1. The two-energy time-concentration curve (solid line) and TIC (dotted line).

The flow velocity can also be estimated using a single-energy method, in which laser pulses with a fixed energy are used for both the depletion and replenishment/observation steps. The diagram of wash-in TIC based on single-energy method is shown as Fig. 2-2. Laser pulses of a wavelength near the optical absorption but a lower energy (than that of laser pulses used for destruction in the two-energy method) transform the nanorods into nanorods with a smaller aspect ratio or into nanospheres at a slower rate (i.e., the replenishment rate is of the same order as the destruction rate). Thus, the concentration of gold nanorods at the observed region in the vessel is controlled by the two opposing forces of depletion of laser pulses and replenishment of flow, and the wash-in TIC can be obtained by monitoring the acoustic intensities as a function of time. In the same way, the TIC can be fitted with an exponential model to extract a parameter related to the flow velocity. In Fig. 2-2, the concentration and the intensity curves of the gold nanorods are shown as solid and dotted lines, respectively. The concentration curve between each measurement points (i.e., the firing of laser pulse for destruction and photoacoustic signal generation) behaves like that obtained from the two-energy method. Note that for the single-energy method, the variations of the concentration curves and the intensity curves are different while the two curves vary in accordance for the two-energy method (as shown in Fig. 2-1).

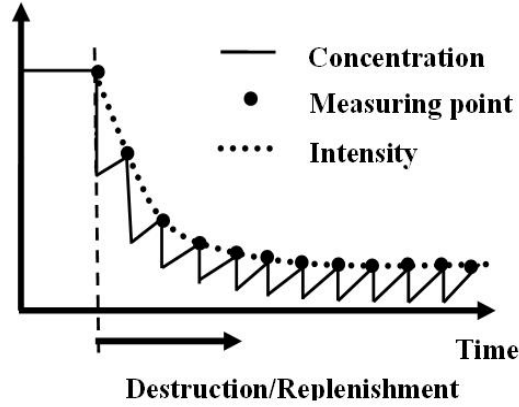


Figure 2-2. The single-energy time-concentration curve (solid line) and TIC (dotted line).

2.2 Principles of photoacoustic wash-out flow estimation

Consider a bolus of contrast agent injected into a simple mixing or perfused volume V , in which blood enters at a flow rate Q via a single input vessel and leaves via a single output vessel. The concentration of the nanoparticles (i.e., the number of nanoparticles per unit volume) entering the volume as a function of time (i.e., the input function) is defined as $n_I(t)$. According to the dilution theory, if the dilution process is homogeneous and instant and the mixing chamber is a linear time-invariant system, the concentration of the nanoparticles at the output end of the mixing/perfused volume $n_O(t)$ (i.e., the output function) is given by

$$n_O(t) = n_I(t) \otimes h(t), \quad (2-1)$$

where \otimes stands for convolution, and $h(t)$ is the dilution transfer function [43, 48-50]. Note that the measured signal amplitude is assumed to be linearly related to the concentration, an assumption that has also been made in other imaging modalities [43, 50]. This assumption is experimentally tested and will be described in the following section.

If the input is an impulse function (i.e., bolus injection), the output function measured is equal to the transfer function of the mixing chamber according to the convolution relation described in (2-1). This is shown by

$$n_I(t) = \delta(t), \quad (2-2)$$

and

$$n_o(t) = h(t), \quad (2-3)$$

where $\delta(t)$ is the impulse function. Assuming a bolus injection at $t=0$ (i.e., $n_o(t) = 0$ for $t < 0$), and an instant and perfect mixing in the chamber, the difference between the input and output numbers of the contrast agent at time t should equal the time derivation of the number of the contrast agent within the mixing chamber. That is,

$$\frac{dVn_o(t)}{dt} = Qn_i(t) - Qn_o(t). \quad (2-4)$$

Thus, according to (2-3) and (2-4), the transfer function becomes [36, 43, 48-50]

$$h(t) = \begin{cases} 0 & t < 0 \\ \frac{Q}{V} e^{-\frac{t}{\tau}} & t > 0 \end{cases}. \quad (2-5)$$

The time constant τ is defined as the ratio of the mixing volume to the volume flow rate, i.e., $\tau = V/Q$. In addition to τ , the TIC can be used to derive other flow-related parameters such as mean transit time (MTT), which is defined as

$$\text{MTT} = \frac{\int_0^{\infty} t \cdot n_o(t) dt}{\int_0^{\infty} n_o(t) dt} \quad [43, 48-50]. \quad (2-6)$$

The MTT represents the time for the entire fluid volume to pass through the mixing volume. According to the indicator-dilution theory, the flow rate is inversely proportional to the MTT. If the input is a bolus and the transfer function is defined as in (2-5), it can be shown that MTT, τ , and V/Q are all equal [49],

$$\text{MTT} = \frac{\int_0^{\infty} t \cdot n_o(t) dt}{\int_0^{\infty} n_o(t) dt} \cong \frac{\int_0^{\infty} t \cdot h(t) dt}{\int_0^{\infty} h(t) dt} = \frac{\int_0^{\infty} t \cdot \frac{Q}{V} e^{-\frac{t}{\tau}} dt}{\int_0^{\infty} \frac{Q}{V} e^{-\frac{t}{\tau}} dt} = \tau = \frac{V}{Q}. \quad (2-7)$$

To reduce estimation errors in the time-intensity measurements so that the flow-related parameters can be accurately extracted, the TICs are fitted to a gamma function $\gamma(t)$ defined by

$$\gamma(t) = \alpha_1 (t - t_o)^{\alpha_2} e^{-\alpha_2(t-t_o)}, \quad (2-8)$$

where t_0 indicates a delay time, α_1 and α_2 are scaling factors, and α_3 represents the skewness [36].

2.3 Principles of photoacoustic wash-in flow estimation

The parameters related to flow velocity are calculated using the TIC by fitting the curve with a mathematical model (that can accurately predict its behavior) [51, 52]. Exponential models have been used previously to fit the wash-in TICs of ultrasonic microbubble contrast agents [44-46]. This approach was applied in the present study to photoacoustic flow measurements employing the laser-induced shape transitions of gold nanorods based on a wash-in analysis. In this section, we describe simulations that were used to confirm the validity of using an exponential model to fit the TIC measured with the proposed methods.

Fig. 2-3 shows a photoacoustic measurement system with a vessel located along the x-axis, the laser-beam axis along the y-axis, and the ultrasonic-beam axis along the z-axis. We assume that the laser spot is much larger than the diameter of the vessel, and let $n(x;t)$ denote the concentration of gold nanorods in the vessel as a function of position (x) and time (t), which has an initial value of $n(x;t) = n_0$ before the measurement process begins (here $n(x;t)$ can be treated as the average concentration on the cross section at x). Assuming that in common detection, the beam profile of the transducer is $b(x)$, which approximates a Gaussian distribution. The measured beam profile of the transducer in this study and the fitted result with a Gaussian function are shown as Fig. 2-4. From the successful fitted result, the beam profile can be represented as

$$b(x) = \frac{b_0}{\sqrt{2\pi\sigma^2}} \exp\left(-\frac{x^2}{2\sigma^2}\right), \quad (2-9)$$

where σ^2 stands for the variance. The effective concentration observed by the transducer is

$$n'(t) = \frac{\int n(x;t)b(x)dx}{\int b(x)dx} = \int n(x;t)b'(x)dx, \quad (2-10)$$

where

$$b'(x) = \frac{b(x)}{\int b(x_0) dx_0} = \frac{1}{\sqrt{2\pi\sigma^2}} \exp\left(-\frac{x^2}{2\sigma^2}\right). \quad (2-11)$$

$n'(t)$ in (2-10) is proportional to the amplitude of the measured photoacoustic signal.

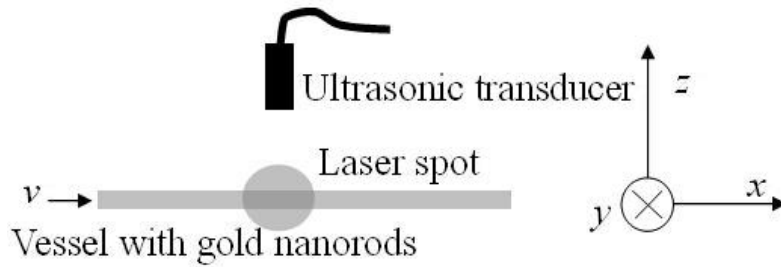


Figure 2-3. Coordinates of the measurement system. The vessel is located along the x-axis, the laser-beam axis is along the y-axis, and the ultrasonic-beam axis is along the z-axis.

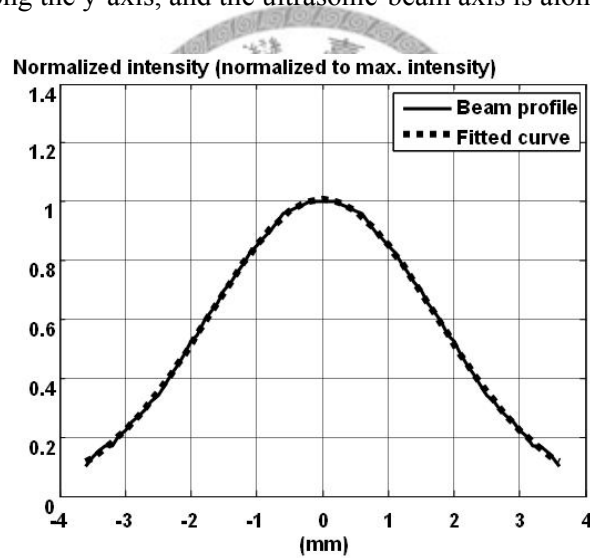


Figure 2-4. The measured beam profile (solid line) of the ultrasound transducer and the fitted result with a Gaussian function (dashed line).

2.3.1 Derivation for the two-energy method

For the two-energy method, the high-energy destruction by laser dominates the TIC in the depletion step because the destruction rate is much higher than the replenishment rate of flow. Once the energy is switched to a level that is sufficiently low to avoid a shape transition, the TIC is mainly determined by the replenishment with new nanorods (of the original shape). Therefore, using the TIC in the

replenishment step to estimate the flow velocity is sufficient in the two-energy method.

Analyzing the effects of the replenishment requires $n(x; t - t_0)$ to be predicted for $t > t_0$ based on $n(x; t_0)$, where the initial condition $n(x; t_0) = n_0 - n_0 l(x)$ with $l(x)$ depends on the shape of the laser beam, which here is approximated as a uniform distribution [53]. $l(x)$ is the destruction profile as opposed to the laser amplitude profile, since the destruction amount (i.e., the number of nanorods transformed) increases as the amplitude of laser pulses [29]. $l(x)$ can be represented as

$$l(x) \cong l_0 \Pi\left(\frac{x}{L}\right) = \begin{cases} l_0 & \text{for } |x| \leq L/2 \\ 0 & \text{elsewhere} \end{cases}, \quad (2-12)$$

where L is the laser beam width of about 5 mm and $l_0 < 1$ is the destruction ratio. From (2-12), the initial condition at the beginning of the replenishment becomes

$$n(x; t_0) = \begin{cases} n_0(1 - l_0) & \text{for } |x| \leq L/2 \\ n_0 & \text{elsewhere} \end{cases}, \quad (2-13)$$

which results from the destruction by the irradiation with high-energy laser pulses.

The concentration in the vessel can be viewed as a collection of compartments with tiny size and the concentration of each compartment approximates a Dirac delta function (of x). Assuming that the flow system is linear and shift-invariant, the contribution to $n(x; t - t_0)$ from one single compartment at $x = x_0$ and $t = t_0$ is $g(x - x_0; t - t_0)n(x_0; t_0)$, where $g(x - x_0; t - t_0)$ is the impulse response corresponding to $n(x; t_0) = \delta(x - x_0)$, and $\delta(x)$ is the Dirac delta function. Taking summation over x_0 yields

$$n(x; t - t_0) = \int g(x - x_0; t - t_0)n(x_0; t_0)dx_0 = n_0 - n_0 g(x; t - t_0) \otimes l(x) \quad \text{for } t > t_0, \quad (2-14)$$

where \otimes denotes convolution (on x). According to the random-walk model, which predicts the characteristics of curves of label (i.e., gold nanorods) concentration in a circulatory system [52], it can be obtained that

$$g(x - x_0; t - t_0) = \frac{1}{\sqrt{4\pi D(t - t_0)}} \exp\left\{-\frac{[x - x_0 - v(t - t_0)]^2}{4D(t - t_0)}\right\}, \quad (2-15)$$

where v is the flow velocity to be estimated, and D is the velocity-dependent dispersion coefficient that represents the randomness [51, 52]. The relation between v and D will be verified in the end of this section. Equation (2-15) represents that $g(x - x_0; t - t_0)$ is a Gaussian distribution, which results from the diffusion effect of the Dirac function at position x_0 and time t_0 , with mean and standard deviation related to v . According to (2-10) and (2-14),

$$\begin{aligned} n'(t - t_0) &= n_0 - n_0 \int [g(x; t - t_0) \otimes l(x)] p'(x) dx \\ &= n_0 - n_0 \int \left[\int g(x - x_0; t - t_0) b'(x) dx \right] l(x_0) dx_0. \end{aligned} \quad (2-16)$$

From (2-11) and (2-15), we can obtain that

$$\int g(x - x_0; t - t_0) b'(x) dx = \frac{1}{\sqrt{\pi[4D(t - t_0) + 2\sigma^2]}} \exp\left\{-\frac{[x_0 + v(t - t_0)]^2}{4D(t - t_0) + 2\sigma^2}\right\}. \quad (2-17)$$

Then, $n'(t)$ can be derived by combining (2-12) and (2-16). That is,

$$\begin{aligned} n'(t - t_0) &= n_0 - n_0 l_0 \int_{-L/2}^{L/2} \frac{1}{\sqrt{\pi[4D(t - t_0) + 2\sigma^2]}} \exp\left\{-\frac{[x_0 + v(t - t_0)]^2}{4D(t - t_0) + 2\sigma^2}\right\} dx_0 \\ &= n_0 - n_0 \frac{l_0}{2} \left\{ \operatorname{erf}\left(\frac{v(t - t_0) + L/2}{\sqrt{4D(t - t_0) + 2\sigma^2}}\right) - \operatorname{sgn}[v(t - t_0) - L/2] \operatorname{erf}\left(\frac{|v(t - t_0) - L/2|}{\sqrt{4D(t - t_0) + 2\sigma^2}}\right) \right\}, \end{aligned} \quad (2-18)$$

where

$$\operatorname{erf}(x) = \frac{2}{\sqrt{\pi}} \int_0^x \exp(-x_0^2) dx_0, \quad (2-19)$$

and

$$\operatorname{sgn}(x) = \begin{cases} 1 & \text{if } x > 0 \\ 0 & \text{if } x = 0 \\ -1 & \text{if } x < 0 \end{cases}. \quad (2-20)$$

We show later in this section that it is reasonable to assume that $D = dv$, where d is a constant. In this case,

$$n'(t-t_0) = n'(t-t_0; v) \cong n_0 \{1 - m[v(t-t_0)]\}, \quad (2-21)$$

where

$$m(y) = \frac{l_0}{2} \left\{ \operatorname{erf} \left(\frac{y+L/2}{\sqrt{4dy+2\sigma^2}} \right) - \operatorname{sgn}[y-L/2] \operatorname{erf} \left(\frac{|y-L/2|}{\sqrt{4dy+2\sigma^2}} \right) \right\}. \quad (2-22)$$

The model suggested by (2-21) and (2-22) is difficult to implement, and hence needs to be simplified. By fitting such an $m(y)$ with

$$\hat{m}(y) = m(0) \exp(-\delta y), \quad (2-23)$$

where δ is a model parameter, we found that for d between 0.7 and 1.6 mm, $m(y)$ and $\hat{m}(y)$ are close to each other. That is,

$$n'(t-t_0)/n_0 \cong 1 - c \exp[-\delta v(t-t_0)] = 1 - c \exp[-u(t-t_0)], \quad (2-24)$$

where c and u are model parameters, and u is proportional to v . According to [44], the ratio of v to u corresponds to the thickness E of detection region (i.e., the region where the nanorods flow in for replenishment and give rise to the signal intensity until the concentration reaches the original level):

$$E \cong \frac{1}{\delta} = \frac{v}{u}. \quad (2-25)$$

The actual ratio of v to u can be determined via phantom experiments. The TICs obtained with the two-energy method can be modeled using (2-24). Fig. 2-5(a) shows simulation results of the replenishment process of gold nanorods using (2-21), where the velocity was 1 mm/sec, d was set to 0.8 mm, l_0 was set to 0.3, and σ was 1.73 mm, which was obtained from the fitted result in Fig. 2-4. The temporal concentration curve (normalized to n_0) of the nanorods was fitted using the exponential model described by (2-24). The simulation result demonstrates the validity of using an exponential model to describe the replenishment process. Fig. 2-5(b) shows the flow parameter u extracted from the fitted exponential curves for flow velocities from 0.3 to 3 mm/sec, which clearly demonstrates the linearity of the relationship between u and v .

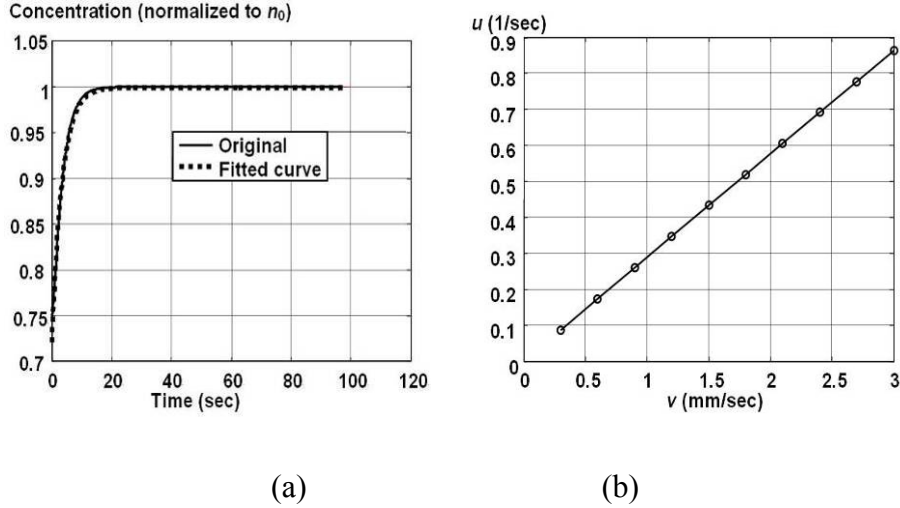


Figure 2-5. Simulation results of flow estimation using the two-energy method. (a) Concentration of nanorods as a function of time for velocity v equal to 1 mm/sec (solid line) and fitted result with the exponential model (dashed line). (b) Extracted flow parameter u from the fitted curve vs. the flow velocity v , indicating the linear relationship between u and v .

2.3.2 Derivation for the single-energy method

In the following the model for TICs obtained with single-energy method is deduced with taking account of interlacing destruction by laser and replenishment of flow (as shown in Fig. 2-2). Consider the irradiation of the vessel using a laser pulse sequence starting at $t = t_0$ with a fixed pulse repetition frequency (PRF) and fixed pulse energy. If the pulse energy is sufficiently low to avoid shape transitions, $n'(t - t_0) = n(x; t - t_0) = n_0$ for $t > t_0$ and the wash-in analysis does not work. In contrast, applying a high pulse energy changes some gold nanorods into spheres or other shapes [29] and consequently $n'(t - t_0)|_{t=(t_0+k/\text{PRF})^+} < n'(t - t_0)|_{t=(t_0+k/\text{PRF})^-}$, where k is the pulse index, and the superscripts + and - in the subscripts represent “soon after” and “immediately before”, respectively. These short periods between $t = (t_0 + k/\text{PRF})^-$ and $t = (t_0 + k/\text{PRF})^+$ are called the destruction phases. The replenishment phases occur between $t = (t_0 + k/\text{PRF})^+$ and $t = [t_0 + (k + 1)/\text{PRF}]^-$, during which $n'(t - t_0)$ increases towards n_0 . The two opposing forces - the destruction phases and the replenishment phases, together determine the characteristic of the TIC as measured by the transducer.

To derive the model for TICs, we separately assessed the effects of the

destruction and replenishment phases on $n'(t-t_0)$. We first consider the destruction phases alone. Assuming that the flow velocity v is zero, the destruction phases dominate the behavior of $n'(t-t_0)$. That is,

$$n'(t-t_0)\Big|_{t=[t_0+(k+1)/\text{PRF}]^-} \cong n'(t-t_0)\Big|_{t=(t_0+k/\text{PRF})^+} . \quad (2-26)$$

It is known that $n'(t-t_0)$ for $t > t_0$ will decrease asymptotically to a constant level. That is,

$$n'(t-t_0)\Big|_{t=(t_0+k/\text{PRF})^-} \cong (n_0 - n_\infty)q^k + n_\infty \text{ for } k = 0, 1, 2, \dots, \quad (2-27)$$

where $q < 1$ is the survival rate, which is a constant if the pulse energy is constant, and n_∞ is the baseline concentration. In general, $0 < n_\infty \ll n_0$ and

$$n'(t-t_0)\Big|_{t=[t_0+(k+1)/\text{PRF}]^-} \cong qn'(t-t_0)\Big|_{t=(t_0+k/\text{PRF})^-} . \quad (2-28)$$

According to (2-26) and (2-28),

$$n'(t-t_0)\Big|_{t=(t_0+k/\text{PRF})^+} \cong qn'(t-t_0)\Big|_{t=(t_0+k/\text{PRF})^-} . \quad (2-29)$$

Equation (2-29) describes the effects of the destruction phases on the concentration of the gold nanorods. It is noticeable that if the flow velocity is low, the replenishment during the destruction phase is negligible because the pulse duration (i.e., period between $t = (t_0 + k / \text{PRF})^-$ and $t = (t_0 + k / \text{PRF})^+$) is on the order of nanoseconds and is much smaller than the length of the replenishment phase (i.e., $1/\text{PRF} = 1/15$ second).

The effects of the replenishment phases between each laser pulse firing can be estimated according to (2-24),

$$1 - n'(t-t_0)\Big|_{t=(t_0+k/\text{PRF})^+} / n_0 \cong c \exp[-u(t-t_0)]\Big|_{t=(t_0+k/\text{PRF})^+} , \quad (2-30)$$

$$1 - n'(t-t_0)\Big|_{t=[t_0+(k+1)/\text{PRF}]^-} / n_0 \cong c \exp[-u(t-t_0)]\Big|_{t=[t_0+(k+1)/\text{PRF}]^-} , \quad (2-31)$$

and

$$1 - n'(t - t_0) \Big|_{t=[t_0+(k+1)/PRF]^-} / n_0 \cong \exp(-u / PRF) \left[1 - n'(t - t_0) \Big|_{t=(t_0+k/PRF)^+} / n_0 \right]. \quad (2-32)$$

Equation (2-32) describes the effects of the replenishment phases on the concentration of gold nanorods.

Combining (2-29) (destruction phase) with (2-32) (replenishment phase) yields

$$1 - n'(t - t_0) \Big|_{t=[t_0+(k+1)/PRF]^-} / n_0 \cong \exp(-u / PRF) \left[1 - qn'(t - t_0) \Big|_{t=(t_0+k/PRF)^-} / n_0 \right]. \quad (2-33)$$

Denoting $n'(t - t_0) \Big|_{t=(t_0+k/PRF)^-} / n_0$ as $n''(k)$ yields

$$n''(k + 1) = 1 - [1 - qn''(k)]s, \quad (2-34)$$

where $s = \exp(-u / PRF)$, and solving (2-34) with $n''(0) = 1$ leads to

$$n''(k) = \left(\frac{1-s}{1-qs} \right) + \left[1 - \left(\frac{1-s}{1-qs} \right) \right] (qs)^k. \quad (2-35)$$

Equation (2-35) indicates that the concentration of gold nanorods decreases exponentially to a constant value determined by the flow velocity and the laser pulse energy. By fitting the measured TIC (with single-energy method) to the following model:

$$n''(k) = n''_{\infty} + (1 - n''_{\infty})z^k, \quad (2-36)$$

where $n''_{\infty} = \frac{1-s}{1-qs}$ and $z = qs$,

$$s = 1 - (1 - qs)n''_{\infty} = 1 - (1 - z)n''_{\infty} \quad (2-37)$$

can be solved, and the flow velocity v is proportional to

$$u = -PRF \cdot \log[1 - (1 - z)n''_{\infty}]. \quad (2-38)$$

Also, the ratio of v to u can be determined via phantom experiments.

Note that $g(x - x_0; t - t_0)$ in (2-14) can be treated as a probability density

function of x for $t \geq t_0$ in the random-walk model [51] with the mean of

$$E\{g\} = x_0 + v(t - t_0) \quad (2-39)$$

and variance of

$$\text{var}(g) = E\{g^2\} - E^2\{g\} = 2D(t - t_0). \quad (2-40)$$

On the other hand, $g(x - x_0; t, t_0)$ is also the solution of the dispersion equation [54]:

$$\frac{\partial n}{\partial t} + v \frac{\partial n}{\partial x} = D \frac{\partial^2 n}{\partial x^2}, \quad (2-41)$$

with the initial condition $n(x; t_0) = \delta(x - x_0)$. Although (2-41) is in the form of a diffusion equation, it is more appropriate to assume that $D = dv$, instead of D being a constant for the flow system considered here.

To justify the relation $D = dv$, consider modeling the vessel as a series of compartments each of length Δx , as shown in Fig. 2-6. The concentration of the gold nanorods in the compartments obeys

$$\frac{dn(x_0, t)}{dt} = -\frac{v}{\Delta x} n(x_0, t) \quad (2-42)$$

and

$$\frac{dn(x_0 + k\Delta x, t)}{dt} = -\frac{v}{\Delta x} \{n(x_0 + k\Delta x, t) - n[x_0 + (k-1)\Delta x, t]\} \text{ for } k \geq 1 \quad [51, 52]. \quad (2-43)$$

Let $g'(k\Delta x; t - t_0)$ be the solution of (2-42) and (2-43) with the initial conditions $n(x_0, t_0) = 1$ and $n(x_0 + k\Delta x, t_0) = 0$ for $k \geq 1$, then

$$g'(k\Delta x; t - t_0) = \frac{[v(t - t_0)/\Delta x]^k \exp[-v(t - t_0)/\Delta x]}{k!} \text{ for } k \geq 0. \quad (2-44)$$

At any time $t \geq t_0$,

$$E\{g'\} = x_0 + [v(t - t_0)/\Delta x]\Delta x = x_0 + v(t - t_0) \quad (2-45)$$

and

$$\text{var}(g') = [v(t - t_0) / \Delta x](\Delta x)^2 = v(t - t_0)\Delta x. \quad (2-46)$$

Equating the right-hand sides of (2-46) and (2-40) yields

$$D = v\Delta x / 2. \quad (2-47)$$

Equation (2-47) indicates that the dispersion coefficient D is proportional to the flow velocity v if both the random-walk model and the compartmental model are appropriate for describing the evolution of the concentration of gold nanorods in a vessel as a function of time and position.

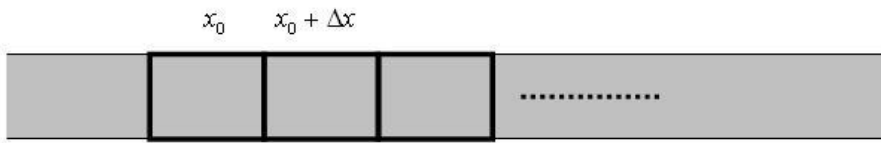


Figure 2-6. Modeling the vessel as a series of compartments of size (length) Δx .

2.4 Wash-out based flow estimation with gold nanospheres

A schematic of the TIC measurement system is shown in Fig. 2-7, which consists of a flow phantom, a laser system, and an ultrasonic receiver. A frequency-doubled Nd:YAG laser (LS-2132U, LOTIS TII, Minsk, Republic of Belarus) operating at 532 nm with a pulse duration of 5 ns and a beam width of 5 mm was used for optical illumination. The optical energy of the laser pulse was 7 mJ, and the pulse repetition rate was 15 Hz. An ultrasonic single crystal transducer (V-381, Panametrics, Waltham, MA) with a center frequency of 3.5 MHz and a focal depth of 7 cm was used to detect the acoustic signals. After detection, the acoustic waveforms were amplified (5800PR, Panametrics, Waltham, MA) and then sampled at 100 MHz by a data acquisition card (CompuScope 12100, Gage, Lachine, Canada) housed in a personal computer on which subsequent data analyses were performed.

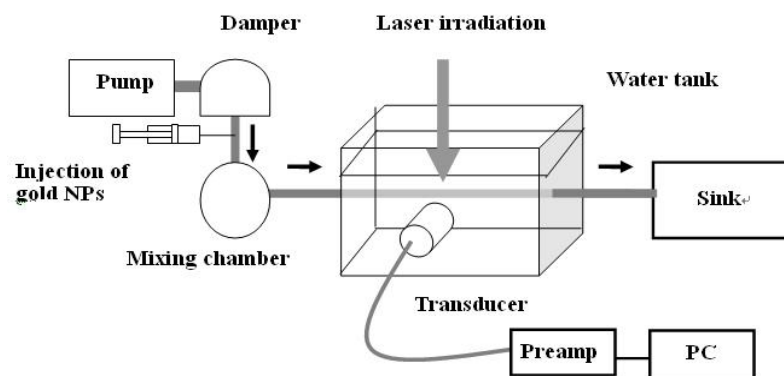


Figure 2-7. Schematic of the photoacoustic TIC measurements system.

Fig. 2-8 shows the results of the linearity between concentration of gold nanospheres and the measured photoacoustic signal. Gold nanospheres with a diameter of 40 nm and peak optical absorption at 520 nm were used. The linearity relation was measured with a measurement system as shown in Fig. 2-7, except there was no flow through the tube and no mixing chamber. Gold nanospheres of different concentrations were placed in the tube, and the photoacoustic signals were recorded by the transducer with laser irradiation. The measurements were repeated three times for each concentration to get the mean value. The jump at the concentration near zero is caused by the low signal-to-noise ratio. From Fig. 2-8, the measured photoacoustic amplitude is linearly related to the concentration where the concentration is less than 0.25 nM. Thus, this concentration range was used for subsequent TIC measurements.

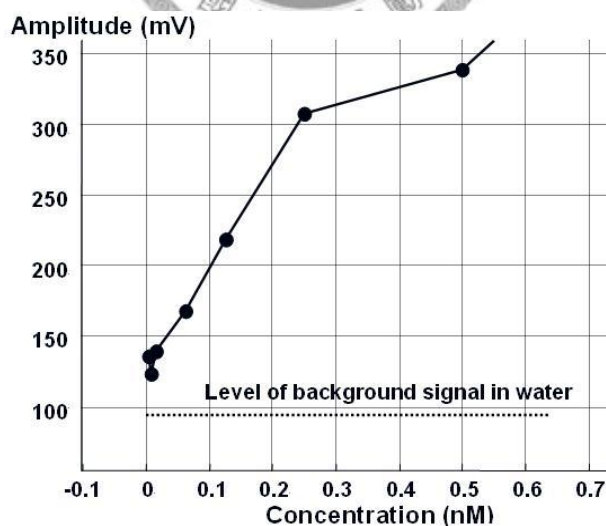


Figure 2-8. Measured photoacoustic signal amplitude as a function of the concentration of gold nanoparticles.

For photoacoustic TIC measurements, gold nanospheres of concentration 1 nM

were injected into a transparent vessel with a diameter of 5 mm. The volume of injection for each measurement was 1 ml. The injection time was around 3 to 5 seconds, which was much shorter than the transit time. The particles then flowed through a chamber with a volume of 30 ml, which was used to prolong the TIC and to simulate the situation where the injection site is far away from the measurement site [49]. A damper was used prior to the injection site in order to stabilize the flow from the pump. Laser irradiation came from the top of the vessel and the acoustic detection was placed on the side. To prevent recirculation of the nanoparticles back in the phantom, the water passed through the phantom only once.

Fig. 2-9 shows measured TICs at various flow rates and results of curve fitting using the gamma function described by (2-16). The flow rates were 2.14 ml/s, 0.61 ml/s, 0.33 ml/s, and 0.23 ml/s, which were equal to the blood flow velocity of human arterioles and venules [55]. V was the volume of the mixing chamber and Q was the flow rate, which is controlled by a flow pump (77021-60, Cole Parmer, Vernon Hills, Illinois). Q was measured by dividing the volume of the mixing chamber (i.e., V) by the time it took to fill the chamber. The time (i.e., V/Q) represented the theoretical transit time. At high flow rates (i.e., V/Q is small), the TIC reaches its maximum and falls toward baseline rapidly. MTT and τ are plotted as functions of theoretical transit time (i.e., V/Q) in Fig. 2-10. The dotted lines represent the linear regression results. At each flow rate, mean and standard deviation values were obtained with three repeated measurements.

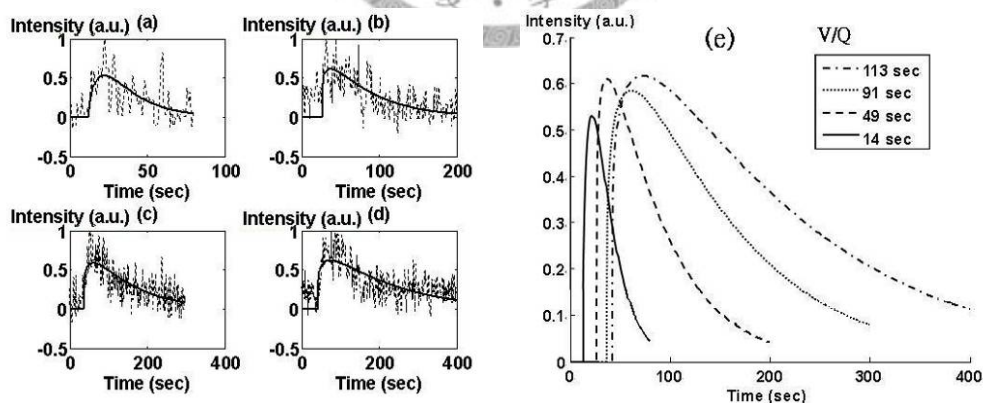


Figure 2-9. Measured TICs and fitted results with gamma function. (a) $V/Q = 14$ sec. (b) $V/Q = 49$ sec. (c) $V/Q = 91$ sec. (d) $V/Q = 113$ sec. (e) Curve-fitted TICs from experimental results at various flow rates (normalized).

As shown in Fig. 2-10, the measured MTT and τ depart from the theoretical values. The possible sources of the deviation are discussed in the following. First, as

noted in our previous study [48], the effective mixing volume may be smaller than the physical volume of the mixing chamber, particularly when the mixing chamber is large or the flow rate is low. This may also contribute to the results shown in this study. As shown in Fig. 2-10, both MTT and τ tend to be underestimated. Second, the MTT results shown in Fig. 2-10, top, intersect with the ideal curve, indicating that there is an overall offset. But note that the measurement curve and the ideal curve do not intersect each other in Fig. 2-10, bottom (τ). This could be due to the fact that the models used in this manuscript assume an instantaneous injection. In practice, however, the injection time is finite. As noted in [49], the finite injection time increases the MTT but not τ , because MTT is calculated using the entire curve but τ is only using the wash-out portion of the curve. And, the insufficient SNR also contributes to part of the measurement errors. Although the absolute measurements are not possible at this point, the linear regression lines (dashed lines) in Fig. 2-10 indicate that the correlation coefficients between the measured time constants and their linear regression fit are close to unity, which demonstrates that relative flow estimation is feasible using TIC methods with gold nanoparticles.

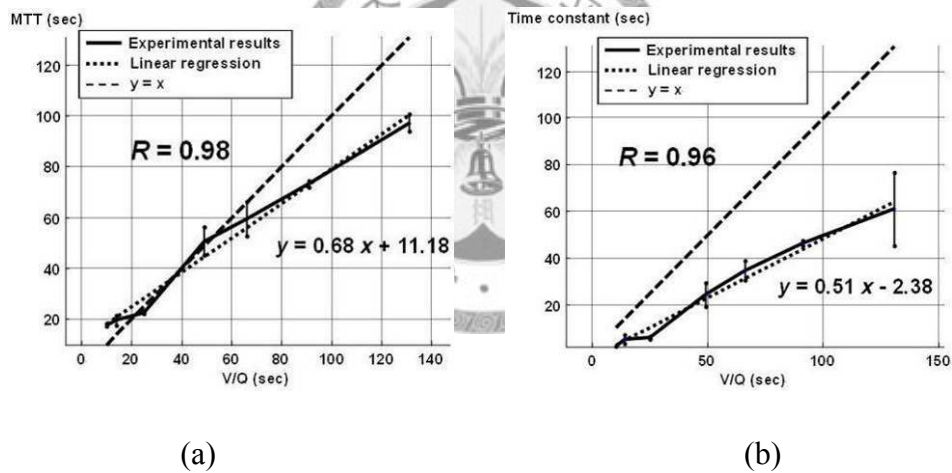


Figure 2-10. Results for flow rates of 3, 2.14, 1.2, 0.61, 0.45, 0.33, and 0.23 ml/sec. (a) MTT vs. V/Q , (b) τ vs. V/Q .

2.5 Wash-in based flow estimation with gold nanorods

2.5.1 Phantom results

The above two-energy and single-energy methods have been experimentally verified using the setup shown in Fig. 2-11, which consisted of a flow system, a laser

system, and an ultrasonic receiver. A frequency-doubled Nd:YAG laser (LS-2132U, LOTIS TII, Minsk, Belarus) operating at 1064 nm with a pulse duration of 5 ns was used for optical excitation. The PRF was 15 Hz. For the two-energy method, the laser energy density for destruction was 24.82 mJ/cm^2 per pulse, which is sufficient to transform the original nanorods into nanospheres or nanorods with a smaller aspect ratio (i.e., nanorods with less optical absorption at 1064 nm) [29]. A series of laser pulses with lower energy density (3.84 mJ/cm^2 per pulse) was then delivered for the observation step. In the single-energy method, a series of laser pulses with an energy density of 16.74 mJ/cm^2 per pulse was applied to simultaneously transform the nanorods at a slow rate and generate acoustic signals for detection. The photoacoustic signals were detected using an ultrasonic single-element transducer (V-303, Panametrics, Waltham, MA, USA) with a center frequency of 1-MHz and a focal depth of 1.8 cm. The -6 dB one-way beam width was measured as 4.0 mm in water by using a needle hydrophone (HNV-0400, ONDA Sunnyvale, CA, USA) with flat spectrum from 0.1 to 20 MHz. The transducer and the hydrophone faced each other horizontally. The focal depth was measured by scanning along the axial direction. Then the beam profile in the focal depth could be obtained by scanning along the elevation direction and the lateral direction and the -6 dB one-way beam width could be estimated accordingly. The acoustic waveforms were amplified by an ultrasonic receiver (5800PR, Panametrics, Waltham, MA, USA) and sampled at 100 MHz using a personal-computer-hosted data acquisition card (CompuScope 12100, Gage, Lachine, QC, Canada), and stored on the personal computer for subsequent data analysis. Gold nanorods with an absorption peak at 1018 nm and at a concentration of 0.26 nM were injected into a vessel with a diameter of 1 mm in a transparent phantom made of polyvinyl alcohol with a sound velocity of about 1800 m/sec. The flow velocity was controlled by an infusion pump (KDS 100, Montreal, QC, Canada). Laser irradiation and acoustic detection were from the side and top of the vessel, respectively (see Fig. 2-11). To prevent recirculation of the nanorods back into the phantom, the solution with nanorods passed through the measurement site once only. The tested flow velocities for both two-energy method and single-energy method were from 0.35 to 2.83 mm/sec, which were close to the blood flow velocity of human capillaries and venules [55]. At each flow rate, mean and standard deviation values were obtained for ten repeated measurements.

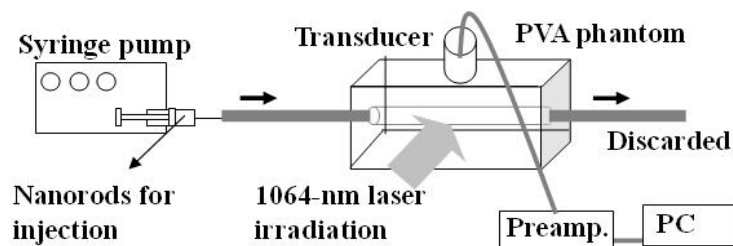


Figure 2-11. Schematic of the photoacoustic flow measurement system. The flow containing gold nanorods is supplied by an infusion pump. The laser irradiation for destruction/detection is from the side, and the ultrasonic transducer for detection is at the top. PVA, polyvinyl alcohol.

The linearity of the relationship between concentration and acoustic amplitude was measured experimentally (Fig. 2-12). At each concentration, mean and standard deviation values (shown as error bars) were obtained with three repeated measurements. The laser irradiation energy density was 6.45 mJ/cm^2 per pulse, and the gold nanorods had an aspect ratio of 5.4 and a peak optical absorption at 990 nm. The measured photoacoustic amplitude was linearly related to the concentration when the concentration was less than 0.5 nM (nanorods per ml). Thus, the concentration range (0.26 nM) used for the flow measurements was within the linear region and was used for subsequent TIC measurements.

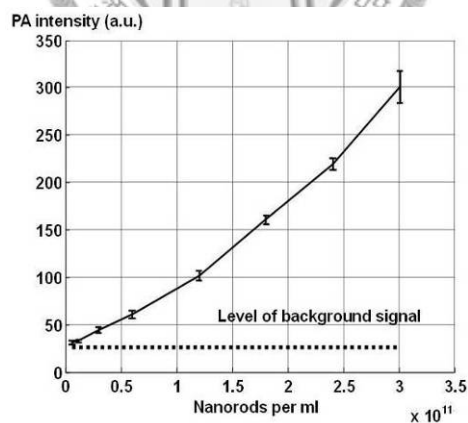


Figure 2-12. Measured photoacoustic signal amplitude as a function of the concentration of gold nanorods.

Fig. 2-13 shows the TICs at zero flow velocity for laser irradiation with different energies. The TIC for an irradiation energy density of 3.84 mJ/cm^2 per pulse was almost constant, which means that this energy density is sufficiently low to ensure minimal rod-to-sphere conversion, and hence this level was used for detection in the

two-energy method. The temporal decreases in the intensities toward baseline for laser energy densities of 16.74 and 24.82 mJ/cm² per pulse indicate the presence of shape transitions: the former and latter were chosen for the single-energy method and destruction of two-energy method, respectively.

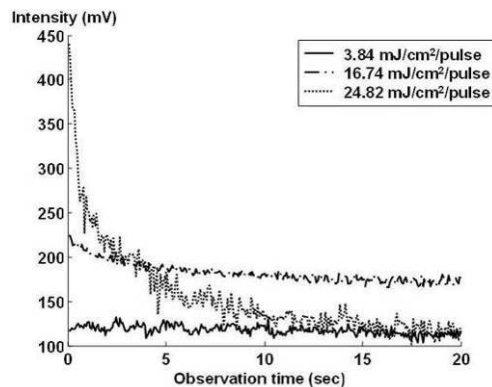


Figure 2-13. The TICs of gold nanorods at zero velocity for different laser irradiation energies.

For flow estimation in the two-energy method, the laser pulses with high energy (24.82 mJ/cm² per pulse) irradiated the gold nanorods for about 5 sec to ensure that most of the nanorods in the region of observation underwent a shape transition (according to Fig. 2-13). The laser energy density was then switched to 3.84 mJ/cm² per pulse for detection, and the acoustic data were recorded.

Fig. 2-14(a) shows the experimentally measured two-energy intensity (normalized to the maximum intensity) at various flow velocities (from 0.35 to 2.83 mm/sec) after curve fitting using the exponential model described by (2-24). The goodness of fit is measured by calculating the root mean squared error (RMSE) between the data set and the fitted curve. Among all fitted results, the RMSE's are below 0.01, indicating accurate fitting is achieved. The presence of the replenishment process is indicated by the temporal increase in intensity, with the curves reaching their maximum intensity (initial constant intensity) faster as the flow velocity increases, which means that the wash-in (replenishment) of gold nanorods into the region of interest of the original shape is highly correlated to the flow velocity.

The flow-dependent variability in the measured TICs in the single-energy method is evident in Fig. 2-14(b), in which the TICs were fitted with the exponential model described by (2-35). The model describes the measured curves well with all RMSE's lower than 0.01. The flow velocities were the same as those used for the two-energy method (i.e., 0.35 to 2.83 mm/sec). Recalling (2-36), the curve decreases

toward a constant value ($n_{\infty} = 1 - \frac{s}{1 - qs}$) that is dependent on the flow velocity and the pulse energy. For a fixed pulse energy the survival rate q of gold nanorods after a single laser irradiation is assumed to be unchanged, and hence the constant n_{∞} determined by the replenishment factor $s = \exp(-u / \text{PRF})$ increases with the flow velocity. This prediction is confirmed experimentally in Fig. 2-14(b).

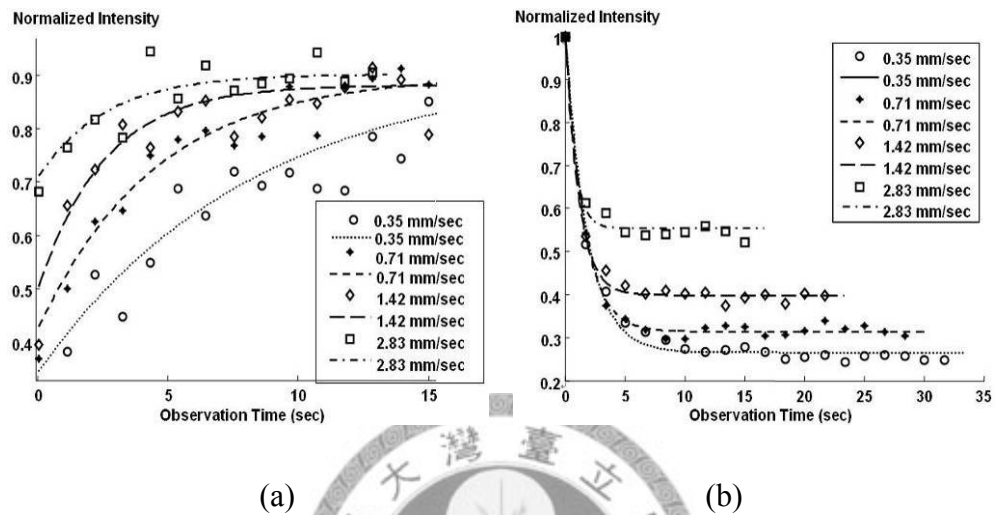


Figure 2-14. Sampled raw data and fitted TICs using the two-energy method (a) and single-energy method (b) at various flow velocities.

The experimental results of flow velocity estimation using the two-energy and single-energy methods are shown in Fig. 2-15(a) and Fig. 2-15(b), respectively. The results are calculated by multiplying the model parameter u (from the curve fitted results of the experimental TICs) by the thickness E of the detection region. The theoretical value of E is chosen as 4.5 mm, and this choice of E will be verified in the next section. At each flow rate, mean and standard deviation values were obtained for ten repeated measurements. The linear regression and theoretical results (i.e., $y = x$) are also shown. Reasons why the slopes of the linear regressions are not unity and why the y-intercepts are not zero are presented in the Discussion. Although the absolute measurements are clearly not accurate at this point, the excellent agreement between the measured velocities and the actual velocities (with linear regression correlation coefficients of 0.94 and 0.99) demonstrates the feasibility of relative flow estimation using wash-in TIC methods with gold nanorods.

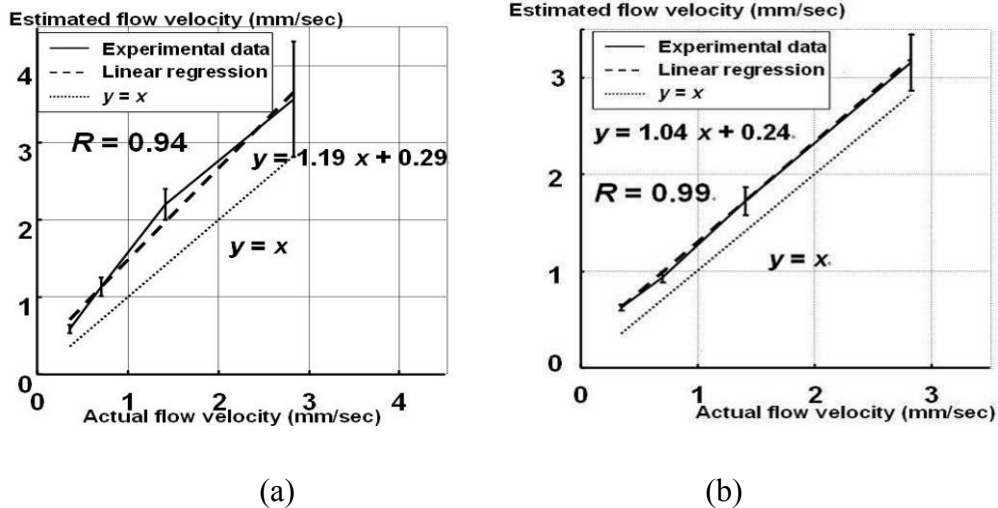


Figure 2-15. Experimental results of flow estimation for flow velocities of 0.35, 0.71, 1.42, and 2.83 mm/sec. (a) Two-energy method. (b) Single-energy method. Error bars show standard deviations.

2.5.2 Discussion: effective width of replenishment

The discrepancy between the estimated flow velocity and the actual flow velocity may be attributable to the effective detection beam width E used in (2-25) to calculate the velocity differing from the actual laser beam width (5 mm). The choice of the effective beam width - which represents the detectable length of replenishment - is determined by the geometry of the irradiating laser beam and the detecting ultrasound beam, which is shown in detail in Fig. 2-16(a). The effective beam width is the distance between the border of the laser beam in the upstream flow (according to the flow direction) and the downstream edge of the ultrasound beam. Thus, the effective beam width was set to 4.5 mm (i.e., half the laser beam width plus half the ultrasound beam) assuming that the ultrasonic beam is located at the center of the laser beam. Note that this assumption may not hold in practice and it results in variations in different experiments. Fig. 2-16(b) shows the linear regression results for the estimated flow velocities, as calculated for effective beam widths from 2 to 5 mm. The slopes of the linear regression lines increase with the effective beam width. However, the correlation coefficients of the measurements and the actual flow velocity are unaffected by the effective beam width. This indicates that relative flow estimation is feasible, and is independent of the effective beam width (i.e., the ratio of v to u). The nonzero intercept on the y-axis may result from the large standard deviation at the highest flow velocity (i.e., 2.83 mm/sec). The curves at this velocity reach their constant value fast, which means the standard deviation increases with

insufficient length of the curves for calculating the velocity. However, the nonzero intercept is generally small enough to be neglected, and so relative flow estimation is also considered to be feasible.

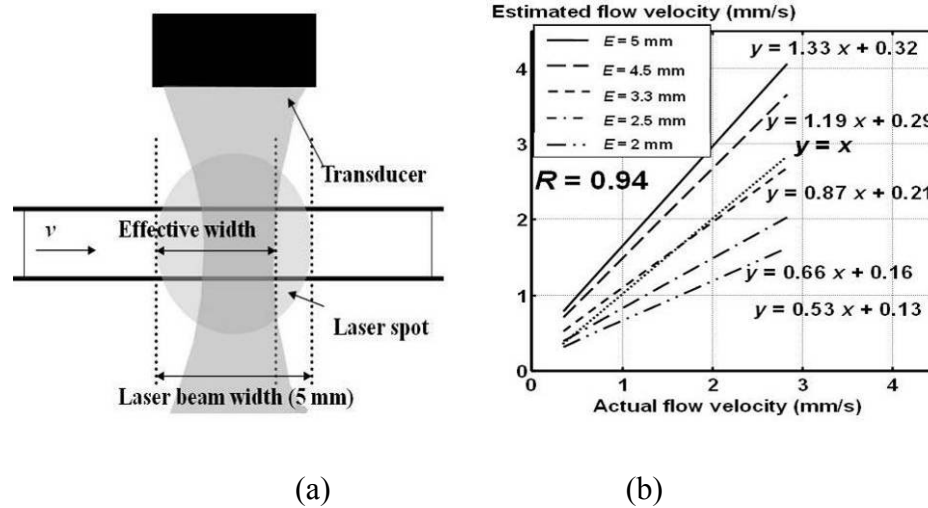


Figure 2-16. (a) Diagram of the effective beam width. (b) Estimated results (two-energy method) for different effective beam widths.

2.5.3 Discussion: two-energy method vs. single-energy method

Fig. 2-17 compares the estimates of the flow velocities obtained using the two-energy and single-energy methods. The overestimated velocities estimated by the two-energy method (except for the smallest flow velocity) may be due to the insufficient length of TIC for calculating v in higher velocities. This is the same reason for nonzero intercept discussed above. Also, the larger standard deviations in high flow velocities may associate to the invalid assumption of a constant survival rate q defined in (2-27) in practice. The survival rate of gold nanorods may vary for each laser pulse due to the concentration of gold nanorods in the observed region varying as a result of the replenishment. In other words, the destruction shape (i.e., $l(x)$) and the destruction level are related to not only the irradiated laser pulse but also the replenishment process. Furthermore, the destruction shape $l(x)$ will not be symmetrical if the replenishment rate dominates the concentration in the detection region when the flow velocity is high. The TIC models may require further refinement for higher flow velocities.

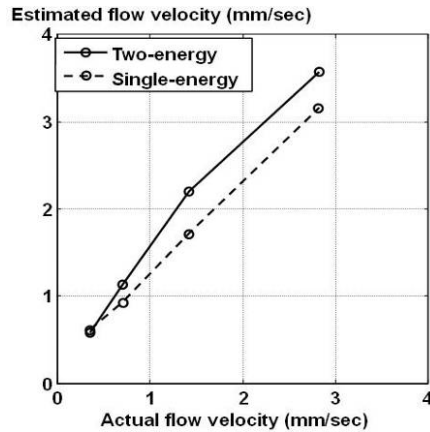


Figure 2-17. Comparison of the experimental results between the two-energy and single-energy methods.

2.6 Concluding remarks

This study has demonstrated the feasibility of using gold nanoparticles as a photoacoustic contrast agent, and confirmed the hypothesis that such particles can be used for flow measurements based on the indicator-dilution theory. The correlation coefficients between the derived parameters (i.e., τ and MTT) and their linear regression fit are all higher than 0.96, thus showing its potential for relative flow rate measurements.

For wash-in analysis, Gold nanorods with a peak optical absorption at 1018 nm were used to estimate flow velocities ranging from 0.35 to 2.83 mm/sec in two-energy method and single-energy method. The linear regression results show that the correlation coefficients between the measured velocities and the true values are close to unity (> 0.94), thus demonstrating the feasibility of the proposed photoacoustic techniques for relative flow estimation.

From the experimental results in Fig. 2-11, the system can achieve sensitivity for a signal-to-noise ratio of 2 at a concentration about 0.1 nanomole per liter, which is at the same order as the concentration (about 0.3 nanomole per liter) of the gold-silica nanoshells injected to the rat for photoacoustic imaging as described in [16]. For *in vivo* applications, the high optical absorption and scattering of tissue constituents may reduce the sensitivity of detection of the gold nanoparticles. Improvement of sensitivity will be the critical step for *in vivo* flow estimation.

CHAPTER 3 PHOTOACOUSTIC MOLECULAR IMAGING

In this chapter, bioconjugated gold nanorods are used for tumor targeting. Several types of bioconjugated gold nanorods, which are also called nanoprobe, are designed and formed by conjugating different biomolecules (e.g., antibody, peptide) on gold nanorods with various aspect ratios. These probes injected into the vessels are capable of binding on the surface of cancer cells depending on the specific antibody-antigen affinity, or directly binding at angiogenesis site through the peptide-integrin interaction on the surface of endothelial cells. The former provides molecular profiles of the targeted cancer cells for a better knowing of the oncogenes and information about heterogeneous cancer cells. Also, it can be expected that a well detection of the angiogenesis by combining angiogenesis targeting with flow estimation methods described in Chapter 2. Furthermore, mixed nanoprobe are used to demonstrate the simultaneous selective multiple targeting by simply tuning the laser wavelength for generation of photoacoustic signals corresponding to the peak optical absorption of the probes. The feasibility of photoacoustic molecular imaging with multiple selective targeting are tested on oral cancer cells both *in vitro* and *in vivo*.

3.1 Introduction

Molecular imaging refers to remote sensing the characteristics of biological process and interactions between molecules [56]. It has a great potential for the early detection and more effective treatment of diseases, because aberrations at the cellular and molecular levels occur much earlier than anatomic changes. In general, specific targeting employs an exogenous nanoprobe that has a high affinity to the molecule (i.e., the biomarker) associated with a specific type of disease, with the targeting of probes tracked using a suitable imaging system.

Molecular imaging methods have developed for many different imaging modalities. X. Gau et al. have developed nanoprobe based on semiconductor quantum dots for cancer targeting and fluorescence imaging in living mice [30]. For

ultrasound imaging, microbubbles targeted to $\alpha_v\beta_3$ -integrins expressed on the endothelium cells were used for imaging angiogenesis [31]. L. Josephson et al. have showed that peptide-conjugated magnetic nanoparticles can target lymph nodes and be the MR (Magnetic Resonance) contrast agent [32]. Furthermore, S. R. Cherry mentioned that several groups have considerable success in small animal imaging by using nuclear imaging system including PET (positron emission tomography) and SPECT (Single Photon Emission Computed Tomography) with the assist of radionuclides-labeled probes [33].

The goal of targeting cancer cells is to determine the expressions of oncogenic surface molecules, which will aid the prediction of clinical outcomes and treatment responses. For this it is necessary to image cancer lesions and obtain pathogenic information on them at the molecular level. However, most previous researches reported in the literature have employed only a single target. Therefore, the goal of this study was to realize *in vivo* photoacoustic imaging with simultaneous multiple selective targeting for cancer diagnosis. We have previously demonstrated *in vitro* multiple targeting [57], and the present study further demonstrates the *in vivo* imaging of small-animal models and extravasation of multiple molecular probes.

For molecular imaging applications, Chamberland et al. have found that the intrinsic contrast of rat tail joint in photoacoustic tomography images can be enhanced by administration of Etanercept-conjugated gold nanorods, which helps to monitor anti-tumor necrosis factor drug delivery [58]. Also, J. A. Copland et al. have used antibody-conjugated gold nanospheres for breast cancer cell targeting [59].

According to the present researches for molecular imaging, mostly only single target is used, while multiple targeting with photoacoustic method is the objective in this study. There are two main reasons why that multiple targeting is needed. First, multiple types of cancer cells with different protein expressions may be located in the same lesion, from which it is hard to distinguish different cells from the heterogeneous populations. Second, one type of cancer cells may own multiple molecular profiles reflecting aggressiveness, metastasis, drug resistance, and so on. Knowing as many the types and characteristics as possible helps to understand the cancer more and to achieve a better diagnosis and a more effective treatment. Cylindrical antibody-conjugated gold nanorods (AuNRs) were used as nanoprobe for photoacoustic imaging to achieve multiple selective targeting. The wavelength at which the optical absorption of gold nanorods is maximal increases with their aspect ratio [28], and AuNRs with different aspect ratios can be conjugated to different antibodies and detected by irradiation with laser pulses at appropriate wavelengths.

3.2 Multiple selective targeting using bioconjugated gold nanorods

The diagram of the process of multiple targeting with bioconjugated gold nanorods to cancer cells and photoacoustic detection is shown in Fig. 3-1. Different ligands (antibodies or peptides) are first conjugated to the surface of gold nanorods with different aspect ratios to form various types of nanoprobess (i.e., bioconjugated gold nanorods). Also, molecules of large molecular weight (PEG) are also conjugated on the surface of nanoprobess. The purpose of attaching blockers is to avoid non-specific bindings such as electrostatic bindings and endocytosis [60]. The nanoprobess are then able to recognize cells which has biomarkers specific to the conjugated ligands. The cells bound with bioconjugated gold nanorods can be detected by photoacoustic imaging. Consequently, different types of cancer cells can be recognized and multiple characteristics can be obtained with laser irradiation at wavelengths corresponding to the peak absorption wavelengths of the nanoprobess. The quantity of various nanoprobess targeted on cancer cells can be detected by comparing the photoacoustic signals at different wavelengths.

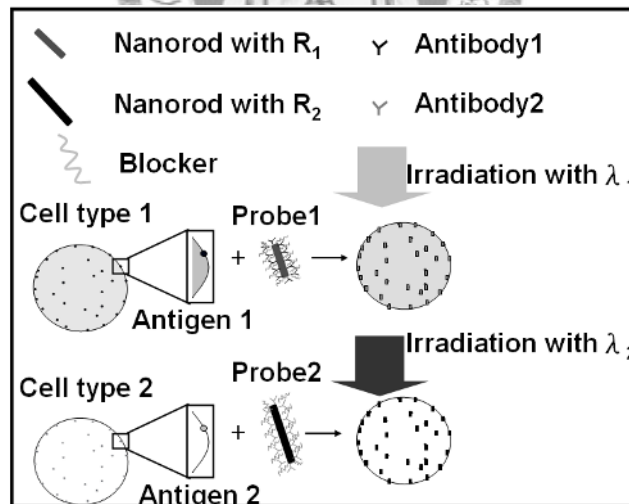


Figure 3-1. Diagram of multiple targeting of two cancer cells by using different nanoprobess with photoacoustic detection at different wavelengths.

Here two oral cancer were used, including OECM1 (oral squamous cell carcinoma) cells with HER2 (human epidermal growth factor receptor 2) overexpressed on the cell surface, and Cal27 (squamous cell carcinoma) cells with

EGFR (epidermal growth factor receptor) overexpressed on the cell surface. These two cell types, each with a specific cell–antibody pair, were adopted to demonstrate multiple selective targeting.

Several biomarkers which are our targets will be introduced as follows. HER2 (human epidermal growth factor receptor 2) expression is associated with growth characteristics and sensitivity to Herceptin chemotherapy, and is a member of the HER tyrosine kinase family that regulates cell growth and proliferation. HER2 has been associated with an aggressive phenotype and a poor prognosis, making it an appealing therapeutic target [61]. EGFR (epidermal growth factor receptor) expression is strongly correlated with tumor metastasis. It is overexpressed in several epithelial malignancies, including head and neck squamous cell carcinoma (HNSCC), with 90% of such tumors exhibiting EGFR overexpression. EGFR plays a critical role in HNSCC growth, invasion, metastasis, and angiogenesis [62]. The specific recognition of the antigens of CXCR4 (CXC-chemokine receptor 4) on the two selected cells was verified carefully by Western blot analysis. CXCR4 is highly expressed in tumor cells and plays an important role in tumor metastasis [63]. It also functions as coreceptors for human immunodeficiency virus (HIV) and is an attractive target for the development of anti-HIV drugs [64]. Extravasations of these antibody-conjugated nanoprobe are necessary for an effective targeting, which means that the probes need to penetrate through the vessel wall. Therefore, targeting angiogenesis is another way of increasing the binding numbers of probes and thus a better detection of the tumor.

To target angiogenesis, we found a peptide, RGD-4C. It is active peptide binds preferentially to $\alpha_v\beta_3$ integrins at sites of tumor angiogenesis and inflamed synovium *in-vivo*, and can be internalized into targeted cells [65]. RGD-4C has been used for target angiogenesis to monitor the growth of the tumor [66, 67]. Also, the peptide was designed a programmed cell death-inducing sequence with selective toxic to angiogenesis endothelial cells and showed anti-cancer ability [68]. With the assist of antibody-conjugated and peptide-conjugated gold nanorods, two types of nanoprobe can be formed: one can target the endothelial cell of angiogenesis, and the other can penetrate through the endothelial gap and bind on the cancer cells, as shown in Fig. 3-2.

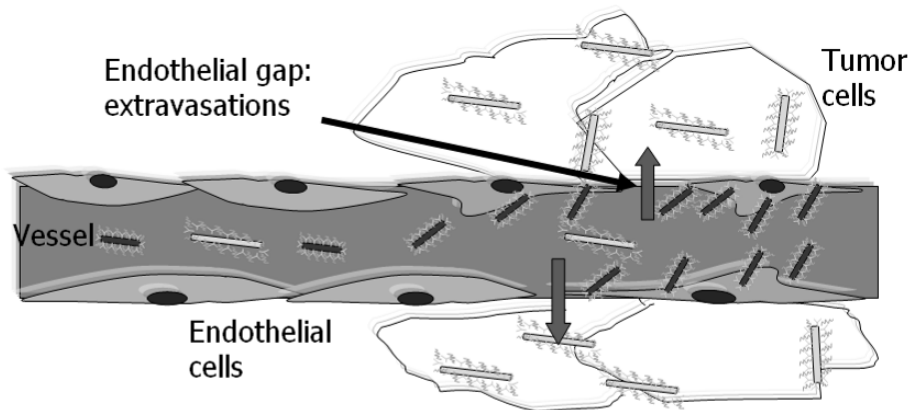


Figure 3-2. Diagram showing targeting of two types of nanoprobes on cancer cell region. One can directly target on endothelial cells at angiogenesis region, the other penetrates through the endothelial gap (extravasations) to target in cancer cells.

To demonstrate multiple targeting, multiple types of nanoprobes were prepared, including AuNR₈₀₀-antiHER2, AuNR₁₀₀₀-antiEGFR, AuNR₈₀₀-antiCXCR4, AuNR₁₀₀₀-antiHER2, and AuNR₈₀₀-RGD4C; where the subscripts represent the peak absorption wavelengths of two types of gold nanorods with mean aspect ratios of 3.7 (800 nm) and 5.9 (1000 nm). Fig. 3-3 shows the absorption spectra of the two nanorods measured by a spectrophotometer (HP 8453, HP, Palo Alto, CA) in Prof. C.-R.-C. Wang's lab in National Chung Cheng University. With these nanoprobes, several *in vitro* cell culture and *in vivo* small animal experiments were designed for demonstration of targeting efficacy of nanoprobes.

First, the targeting ability of two nanoprobes, AuNR₈₀₀-antiHER2 and AuNR₁₀₀₀-antiEGFR, were tested with different mouse bearing OECM1 and Cal27, respectively. Each probe and its control group (pure gold nanorods with only blockers conjugated) were respectively reacted with distinct cancer cells, each with a specific cell-antibody pair, *in vitro* and *in vivo* to demonstrate the multiple targeting relations.

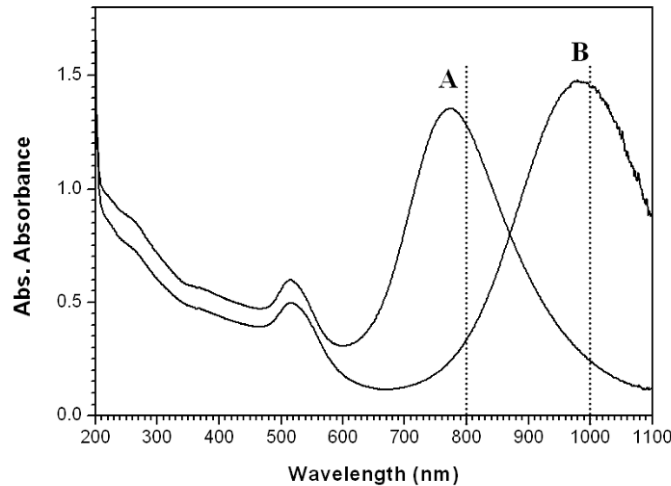


Figure 3-3. Absorption spectra of gold nanorods with two aspect ratios: (A) AuNR₈₀₀ and (B) AuNR₁₀₀₀. This figure was measured by Prof. Wang's lab in National Chung Cheng University.

The second part, multiple targeting on oral cancer cell line with two specific targets was performed. We conducted the multiple-target measurements on the OECM1 cells using the two different nanoprobe, AuNR₈₀₀-antiHER2 and AuNR₈₀₀-antiCXCR4, to cross examine the types and amount of the protein expressed.

Angiogenesis targeting was also demonstrated with RGD-4C conjugated nanoprobe. The chosen tumor was OECM1 tumor, in which angiogenesis has developed from the pre-existing vessels for supplying the tumor.

The simultaneous selective targeting was demonstrated in the last part of this chapter, in which mixed probes (i.e., AuNR₁₀₀₀-antiHER2 and AuNR₈₀₀-RGD4C) to recognize different biomarkers associated with tumor characteristics. The mixed probes were injected into one mouse and the bearing tumor was imaged at distinct laser wavelengths to examine the expression level of the targeted nanoprobe.

3.3 *In vitro* cell culture study

Before performing *in vivo* animal experiments, *in vitro* experiments with cell cultures were performed to verify the targeting ability of the bioconjugated gold nanorods to cancer cells. The cells were collected into a centrifuge tube and the cell number was adjusted to 1.2×10^6 in the endorff tube. Then PBS containing 10%

FBS (fetal bovine serum) plus probes or non-conjugated nanorods were added into the cells for binding reaction. The ependorff tubes were shaken in 4 °C for one hour. After the incubation, those unbinding nanorods were removed by washing in PBS and centrifuging in 2850 rpm for three times. The samples were placed in a phantom made from transparent plastic (Rexolite 1422, San Diego Plastics, CA). The phantom was 4 cm × 4 cm × 3 cm in size and contained several tubes with an internal diameter of 2.5 mm.

3.3.1 Cell culture

In preparation of the cell culture, OECM1 cells were maintained in 90% RPMI1640 and 10% FBS (fetal bovine serum), and Cal27 cells were cultured in 90% DMEM and 10% FBS. All of the cell lines were maintained in a 37°C incubator with a humidified environment of 5% CO₂ in air. The cell culture was prepared by Dr. Shieh's lab in National Cheng Kung University.

3.3.2 Antibody and peptide preparation

EGFR antibody was purchased from Thermo Fisher Scientific (MA, USA). HER2 antibody was purified from the A-HER2 hybridoma (CRL-10463) by GlycoNex (Taiwan). The antibodies were prepared by Dr. Shieh's lab in National Cheng Kung University.

3.3.3 Nanoprobes conjugation

The synthesis and conjugation of gold nanoprobes were accomplished by Prof. C.-R.C. Wang's lab in National Chung Cheng University. Gold nanorods were synthesized by the electrochemical conversion of an anodic gold material into particles within an electrolytic cosurfactant system, which is a procedure that have been developed previously [69]. The cationic surfactants used were CTABr (hexadecyltrimethylammonium bromide) and TDABr (tetradodecylammonium bromide). The particle shape was successfully controlled using cationic cosurfactant micelles that included several other ingredients such as cyclohexane and trace amount of silver ions [70]. The gold nanorods were then well dispersed in aqueous solutions. Multiple-target studies were achieved using two nanorod samples and a gold-nanosphere system exhibiting surface plasmon resonances at approximately 800 and 1000 nm for the subsequent antibody conjugation and cell binding.

In addition to successful and stable conjugation of the recognition unit to the AuNRs through chemical bonding, it was also necessary that the nanoprobe exhibited high dispersity prior to binding to cancer cells. To achieve these goals, we adopted a conjugation protocol involving a 1-ethyl-3-(3-dimethylaminopropyl) carbodiimide hydrochloride (EDC-mediated coupling reaction and subsequent attachment of a blocking agent (mPEG-SH, a thiol-terminated methoxypoly (ethyleneglycol)) at nonspecific adsorption sites on the AuNRs [71, 72].

Briefly, using HER2 as an example, the absorbance of a 1-ml aliquot of the AuNR solution was adjusted to 0.8, as measured under a 2-mm optical path length at the resonance. Five milliliters of 0.4 M cysteamine dihydrochloride and 10 ml of 16 mM HNO₃ were then added, and the solution was aged for 30 min before being centrifuged at 5500 rpm for 15 min and redispersed into 1 ml of deionized water to remove any excess cysteamine. In a separate vial, an EDC-mediated solution was prepared by adding 0.02 g of EDC to 100 μ l of aqueous 1.04 M NHS (N-hydroxysuccinimide) solution and then aging the mixture for 10 min. A 2-ml aliquot of the EDC-mediated solution was mixed with 2 ml of an 8 mg/ml solution of HER2 monoclonal antibody (mAb) in 10 mM PBS in a microcentrifugation tube and then aged for 1 hour at 4 °C. To complete the conjugation process, this modified HER2 mAb solution was then added into the previously prepared cysteamine-modified AuNR solution (1 ml) and aged for 1 hour at 4 °C. This AuNR-HER2 mAb solution was flocculated by centrifugation at 5500 rpm for 15 min and then redispersed into 1 ml of aqueous 1.04 mM mPEG-SH (MW = 5000; Nektar) solution. The dispersed solution was then aged for either 1 hour or overnight. The final solution was again centrifuged at 5500 rpm for 15 min to remove any excess mPEG-SH. The flocculates were then redispersed into a 10 mM PBS solution to produce the nanoprobe. The aqueous nanoprobe solutions remained well dispersed for at least 1 month when stored at 4 °C. The absorption spectra of the nanoprobe were measured by the spectrophotometer and showed that there was no apparent absorption peak wavelength shift from the nanorods before conjugation, thus indicating the absorption property of the nanorods will not change before/after the conjugation.

3.3.4 Western blot

Western blot analysis can detect specific protein in a mixture while giving the information about the size of the protein. The process is listed as follows. Subconfluent cells were lysed in ErbB lysis buffer (50 mM HEPES, 150 mM NaCl, 10% glycerol, 1% Triton X-100, 50 mM sodium fluoride, 10 mM sodium

pyrophosphate, 2 mM EDTA, 2 mM EGTA, 2 mM sodium orthovanadate, and a protease inhibitor mixture tablet (Roche Molecular Biochemicals)). Protein concentration was determined by the BCA protein assay (Pierce). Total protein samples were separated on a 10% SDS-polyacrylamide gel (PAGE) and transferred to a polyvinylidene difluoride (PVDF) membrane (Immobilon-P, Millipore, Bedford, MA). The membrane was blocked in 5% non-fat milk in PBS overnight at 4 °C. Membranes were probed with mouse anti-ErbB2 antibody (Calbiochem, Cat. No. OP15), mouse anti-Hepatitis B Virus Surface antigen antibody, or rabbit anti-CXCR4 antibody, which was solved in 1% non-fat milk in PBS for 1 hour at room temperature, washed three times in PBST (PBS with 0.1% Tween20), incubated with goat anti-mouse horseradish peroxidase labeled antibody diluted 1:5000 in 1% non-fat milk in PBS for 1 hour at room temperature, and then washed three times in PBST. The signal was visualized by an enhanced chemiluminescence solution (ECL Plus, Amersham Pharmacia Biotech) and documented by Las-3000.

For multi-target molecular photoacoustic imaging and photothermal therapy, the cancer cell line bank has been screened for appropriate model cells (Fig. 3-4). The results were accomplished by Dr. D.-B. Shieh's lab in National Cheng Kung University. OECM1 presents overexpression of Her2 and relatively lower expression of EGFR, while Cal27 does the opposite way. For both cells, high expressions of CXCR4 were found.

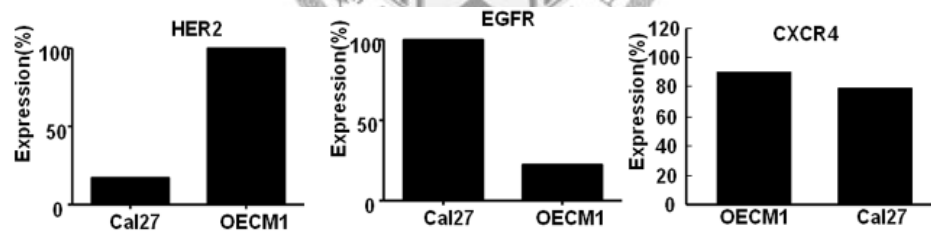


Figure 3-4. Western blot analysis reveals over expression of Her2 in OECM1 cell, EGFR in Cal27, and CXCR4 in both cells. The results were from Dr. D.-B. Shieh's lab in National Cheng Kung University.

3.3.5 Transmission electron microscopy image

Prior to photoacoustic measurements, the binding efficiency of cells with bioconjugated gold nanorods was examined in a transmission electron microscopy (TEM) (JEM 2010, JEOL, Japan) at 200 kV. Fig. 3-5 represents the TEM images of OECM1 cells slice with thickness smaller than 100 nm from Dr. D.-B. Shieh's lab in National Cheng Kung University. The bioconjugated gold nanorods attached on the

surface of the cell are observed in the cells. Hence, the specific binding function of bioconjugated gold nanorods is demonstrated.

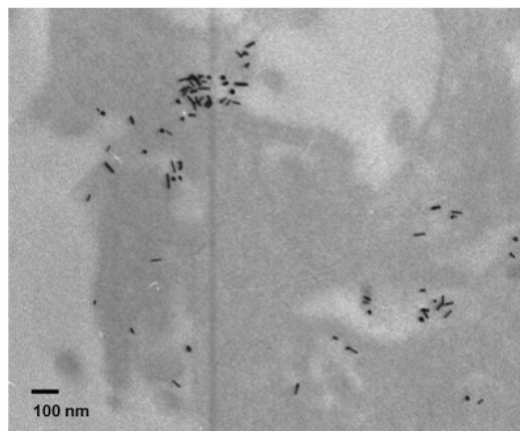


Figure 3-5. Electron micrograph of a portion of an OECM1 cell targeted with mixed nanoprobe, AuNR₈₀₀-antiHER2 and AuNR₁₀₀₀-antiCXCR4, clearly showing the presence of the gold nanorods (black cylinders) attached around the border of the cell. The results were from Dr. D.-B. Shieh's lab in National Cheng Kung University.

3.3.6 Photoacoustic measurement

To demonstrate multiple targeting of bioconjugated gold nanorods, the two wavelengths chosen to irradiate the samples for generating photoacoustic signals (one close to and the other far from the peak absorption of the specific target probes) were 800 and 1064 nm, corresponding to the peak absorption wavelengths of the AuNR₈₀₀-antiHER2 and AuNR₁₀₀₀-antiEGFR probes. The samples in the phantom were imaged in cross-sectional direction by the same photoacoustic imaging system in Fig. 3-6 with a scan step of 0.02 mm. The figure cascades the two images obtained at the two wavelengths on the same absolute scale to compare the absolute intensity of the samples obtained at different laser wavelengths. Results showed that the image intensities of the experimental groups were generally about 10 dB higher than those in the control groups. In other words, the targeting ability of specific probes to cancer cells and the wavelength selectivity of photoacoustic detection are clearly demonstrated.

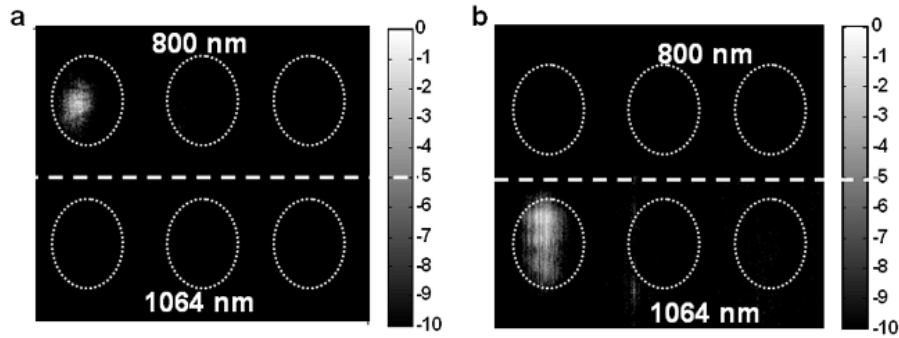


Figure 3-6. (a) Images of OE2M1 cells obtained at 800 and 1064 nm. OE2M1 cells were with AuNR₈₀₀-antiHER2, AuNR₁₀₀₀-antiEGFR, and AuNR₈₀₀ (from left to right) (b) Images of Cal27 cells obtained at 800 and 1064 nm. Cal27 cells were with AuNR₁₀₀₀-antiEGFR, AuNR₈₀₀-antiHER2, and AuNR₁₀₀₀ (from left to right). The images are displayed with a dynamic range of 10 dB.

3.4 *In vivo* small animal study

For *in vivo* studies, the cancer cells were induced on the back of NOD-scid male mice by the subcutaneous injection of 10⁷ cells. The tumors were measured by the photoacoustic technique after 10–15 days of growth, and were typically 5 mm in diameter and 2–3 mm thick.

3.4.1 Targeting cancer cell with antibody-conjugated nanoprobe

The optical irradiation was delivered by a widely tunable pulsed Ti:sapphire laser (CF-125, SOLAR TII, Minsk, Republic of Belarus) lasing 800 nm laser and an Nd:YAG laser (LS-2132 U, LOTIS TII, Minsk, Belarus) lasing 1064 nm laser, respectively. These wavelengths were chosen according to the peak absorptions of the gold nanoprobe. The pulse repetition rate was 10 Hz. A homemade photoacoustic transducer made of lithium niobate (LiNbO₃) material with a center frequency of 20 MHz and a focal depth of 9.5 mm was used for signal detection. The transducer had a diameter of 6 mm and a 0.65 mm hole in the center of the transducer surface for insertion of optical fiber that can solve conventional device-placing problem. Thus, the transducer can be integrated with a single fiber (FT-600-UMT, Thorlabs, Newton, NJ) with a diameter of 600 μm through the hole to achieve registered irradiation and detection. The integrated photoacoustic transducer was driven by a precision

translation stage (HR8, Nanomotion, Yokneam, Israel) to perform one-dimensional cross-sectional scans of the tumor with a step size of 0.2 mm. The received acoustic waveforms were amplified by an ultrasonic receiver (5077PR, Panametrics, Waltham, MA) and then recorded at a sampling rate of 200 Msamples/second by a data acquisition card (CompuScope 14200, Gage, Lachine, QC, Canada).

Mice with tumor cells were anesthetized with halothane vapor using a vaporizer system (Fluosorber, Market Supply, UK), placed on a plate stage, and illuminated with an incandescent bulb to keep the mouse warm. Transparent ultrasonic gel (ECGEL 4000, Hometech, Taiwan) was added between the tumor region and the transducer to improve acoustic wave propagation. For mice with the OECM1 tumor, a 100- μ l mixture of AuNR₈₀₀-antiHER2 and AuNR₈₀₀ at a concentration of 30 nM was prepared for injection, and the irradiating wavelength was 800 nm. For Cal27 tumors, a 100- μ l mixture of AuNR₁₀₀₀-antiEGFR and AuNR₁₀₀₀ at a concentration of 30 nM was prepared for injection, and the irradiating wavelength was 1064 nm.

The photoacoustic experimental setup for *in vivo* imaging (Fig. 3-7) consisted of an optical irradiating system, a precision translation stage, a homemade animal stage, and a data acquisition card. The nanoprobes and gold nanorods (control group) were injected into the tail veins of two mice. In each mouse the targeting process was monitored at multiple time points within 24 hours after nanorod injection. At each measurement time point, the tumor was imaged in three cross sections to calculate the averaged photoacoustic intensity within the tumor region. After each photoacoustic scanning procedure, an ultrasound image was also acquired in the same region to show anatomic information. Ultrasound images displayed on a grayscale were superimposed with the corresponding photoacoustic images displayed in red pseudocolor.

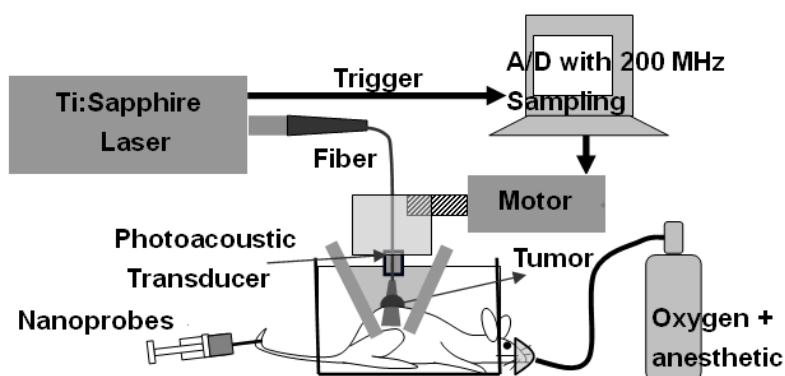


Figure 3-7. Schematic diagram of the experimental setup for *in vivo* photoacoustic imaging.

The photoacoustic images of a Cal27 tumor for injections with AuNR₁₀₀₀ and AuNR₁₀₀₀-antiEGFR in Fig. 3-8 demonstrate the specific targeting ability of the AuNR₁₀₀₀-antiEGFR probe. The contour of the tumor region can be clearly seen in the fusion images of photoacoustic and ultrasound images shown in Fig. 3-8(a) and Fig. 3-8(c). Also, photoacoustic images obtained at different time points post injection were shown in the same scale (25 dB dynamic range). The contrast is higher for the AuNR₁₀₀₀-EGFR data post-injection (7 hours after injection) photoacoustic image within the tumor region than for the pre-injection image, while there is no apparent difference between the pre- and post-injection images for the AuNR₁₀₀₀ injection (Fig. 3-8(b) and (d)).

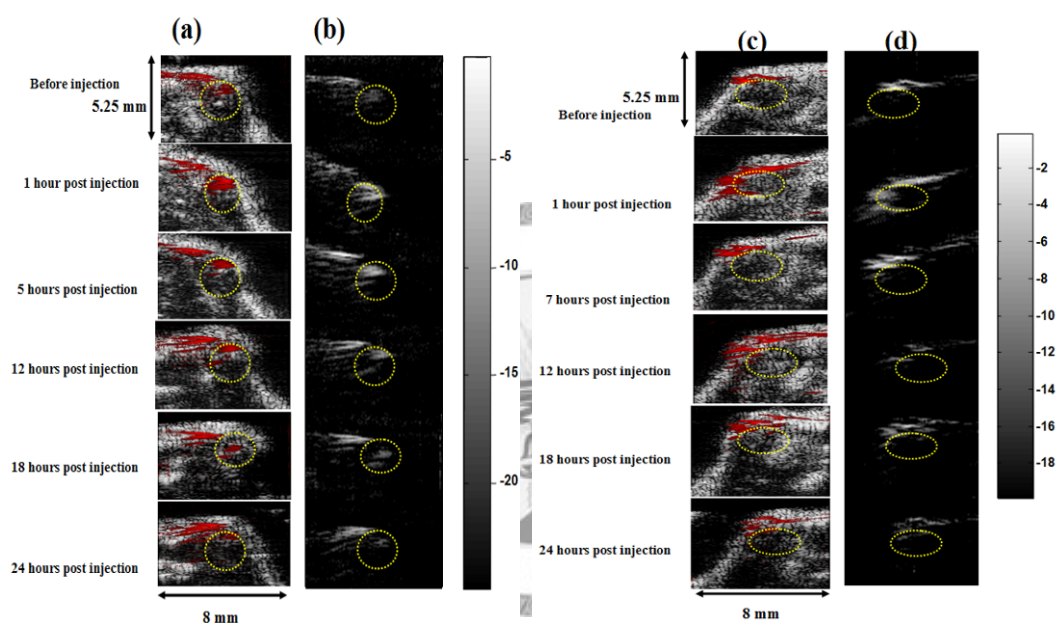


Figure 3-8. Images of a Cal27 tumor before and after the injection of AuNR₁₀₀₀ and AuNR₁₀₀₀-antiEGFR. Ellipses indicate the tumor regions. (a) Fusion images before/after AuNR₁₀₀₀-antiEGFR injection at different time points. The ultrasound images are displayed on a grayscale, and the superimposed photoacoustic images obtained at an optical wavelength of 1064 nm are displayed in red pseudocolor. (b) Photoacoustic images before/after AuNR₁₀₀₀-antiEGFR injection shown in the same scale. (c) Fusion images before/after AuNR₁₀₀₀ injection at different time points. The ultrasound images are displayed on a grayscale, and the superimposed photoacoustic images obtained at an optical wavelength of 1064 nm are displayed in red pseudocolor. (d) Photoacoustic images before/after AuNR₁₀₀₀ injection shown in the same scale.

The photoacoustic images of OECM1 tumors in Fig. 3-9(a)–(d) also demonstrate the other specific cell–antibody binding relations. The post-injection images for AuNR₈₀₀-antiHER2 exhibited evident increased photoacoustic intensity from 1 hour

to 17 hours after injection relative to the pre-injection image (Fig. 3-9(a), (b)). The decrease of the intensity may be due to the washout of the probes. In contrast, the pre- and post-injection images of the control group (i.e., injection of AuNR₈₀₀) showed no obvious changes in signal intensity (Fig. 3-9(c), (d)).

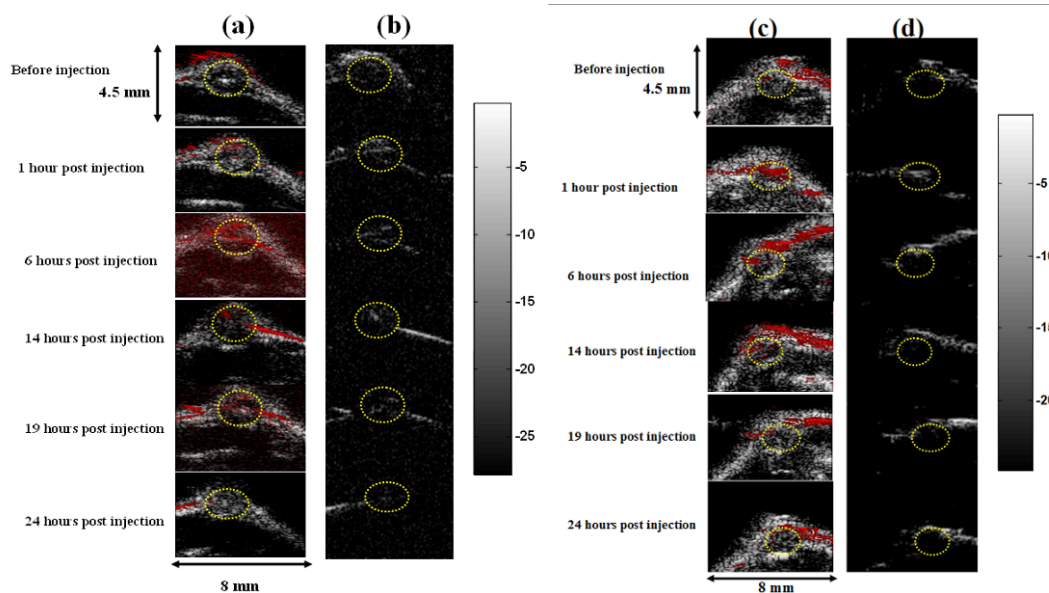


Figure 3-9. Images of OECM1 tumor before and after the injection of AuNR₈₀₀ and AuNR₈₀₀-antiHER2. Ellipses indicate the tumor regions. (a) Fusion images before/after AuNR₈₀₀-antiHER2 injection at different time points. The ultrasound images are displayed on a grayscale, and the superimposed photoacoustic images obtained at an optical wavelength of 800 nm are displayed in red pseudocolor. (b) Photoacoustic images before/after AuNR₈₀₀-antiHER2 injection shown in the same scale. (c) Fusion images before/after AuNR₈₀₀ injection at different time points. The ultrasound images are displayed on a grayscale, and the superimposed photoacoustic images obtained at an optical wavelength of 800 nm are displayed in red pseudocolor. (d) Photoacoustic images before/after AuNR₈₀₀ injection shown in the same scale.

The results of multiple targeting of OECM1 tumor with AuNR₈₀₀-antiHER2 and AuNR₈₀₀-antiCXCR4 are shown in Fig. 3-10, which reveals an enhanced contrast between the tumor region and surrounding tissues. After the probes injection, the tumor region exhibits conspicuous photoacoustic signals and the high intensity remains to 24 hours. The results demonstrate that multiple targeting of single type of cancer cells is achieved with mixed nanoprobes. If the two antibodies, HER2 and CXCR4, are conjugated with gold nanorods with different aspect ratios, two protein expressions of OECM1 cells can be obtained by using photoacoustic measurements with different irradiating wavelengths.

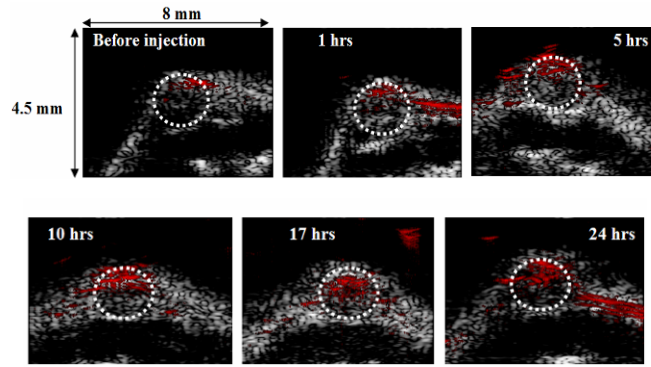


Figure 3-10. Images of OECM1 cells obtained at various time points after injection of AuNR₈₀₀-antiHER2 + AuNR₈₀₀-antiCXCR4.

The intensities of three cross-sectional photoacoustic images of the tumor region were averaged and normalized relative to the pre-injection averaged intensity of the tumor region in order to quantitatively measure the targeting efficacy. As shown in Fig. 3-11(a), the contrast between the experimental group (AuNR₁₀₀₀-antiEGFR injection) and the control group (AuNR₁₀₀₀ injection) was maximally about 3.5 dB at 7 hours after the injection, indicating the specific targeting of AuNR₁₀₀₀-antiEGFR to Cal27 cells. The increased intensities at 1 hour post-injection in both cases might indicate nonspecific binding due to accumulation in the circulation [73]. Fig. 3-11(b) shows normalized averaged image intensities within the OECM1 tumor regions plotted as a function of the observation time. The intensity contrast between the tumor with AuNR₈₀₀-antiHER2 injection (solid line) and the tumor with AuNR₈₀₀ injection (dashed line) was more than 2 dB at 14 hours, while multiple targeting with AuNR₈₀₀-antiHER2 and AuNR₈₀₀-antiCXCR4 shows a maximum contrast of 4 dB at 10 hours and 3 dB at 24 hours. The results have not only demonstrated the targeting ability of AuNR₈₀₀-antiHER2 to OECM1 but also the effectiveness of the multiple targeting with mixing two nanoprobes.

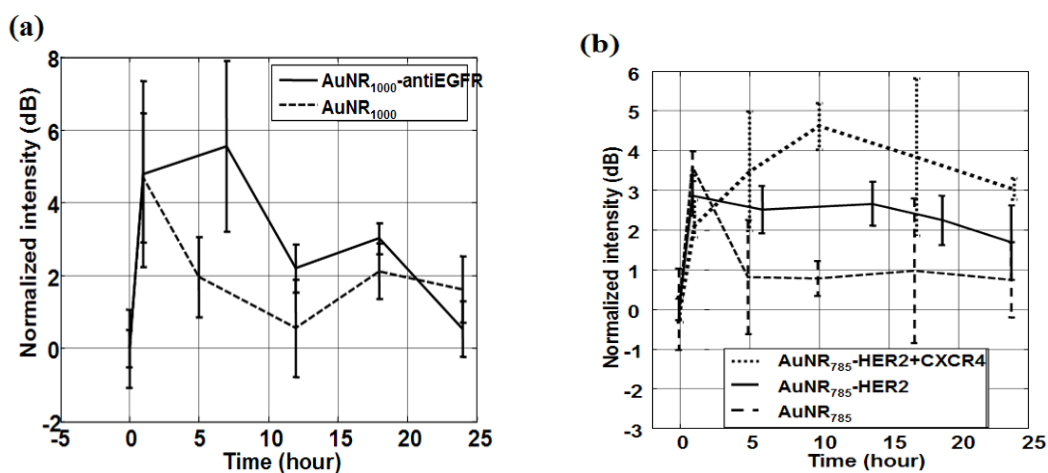


Figure 3-11. (a) Averaged image intensities within the tumor region versus time after injections with AuNR₁₀₀₀-antiEGFR (solid line) and AuNR₁₀₀₀ (dashed line). (b) Averaged image intensities within the tumor region versus time after injection with AuNR₈₀₀-antiHER2 (solid line), AuNR₈₀₀ (dashed line), and AuNR₈₀₀-antiHER2 + AuNR₈₀₀-antiCXCR4 (dotted line). The averages were calculated from three cross-sectional images. Error bars indicate standard deviations.

Atomic absorption (AA) spectroscopy analysis was used to confirm the targeting efficacy of HER2-probes. After photoacoustic imaging, the tumor tissues were surgically harvested from the mouse. The time point was 6 hours post-injection. The tumor tissues were scaled weight, homogenized, and then placed into a centrifuge tube containing 30 ml of nitric acid (12 M) for incubation for 3 days to permit complete dissolution of the tissue. The obtained liquid through was subjected to AA (UNICAM Solaar M6 series) analysis. The AA spectroscopy analysis results indicate that the Au ion within tumor tissues with HER2-probe injection is 9.1 $\mu\text{g au+}$ per gram tissue weight, while that with AuNR₈₀₀ (control group) injection is 1.23 $\mu\text{g au+}$ per gram tissue weight.

3.4.2 Targeting angiogenesis with peptide-conjugated nanoprobes

Fig. 3-12 show the *in vivo* results for OECM1 cells with RGD4C probes injection at the wavelength corresponding to the peak absorption wavelength of the specific nanoprobes, 800 nm. The photoacoustic intensity is displayed in yellow pseudo-color overlapped with ultrasound image in gray scale. Fig. 3-12(a) and (c) are the pre-injection and 4 hours post-injection control group (pure gold nanorods injection) results. The contrast of the tumor is not detectable, indicating there is no specific targeting of pure gold nanorods. Fig. 3-12(b) and (d) show the results for OECM1 cells

with AuNR₈₀₀-RGD4C injection. Compared to the pure nanorods injection, the intensity of image with RGD4C probe injected increases at 4 hours after injection. This can be the evidence of the specific targeting of RGD4C probes to angiogenesis.

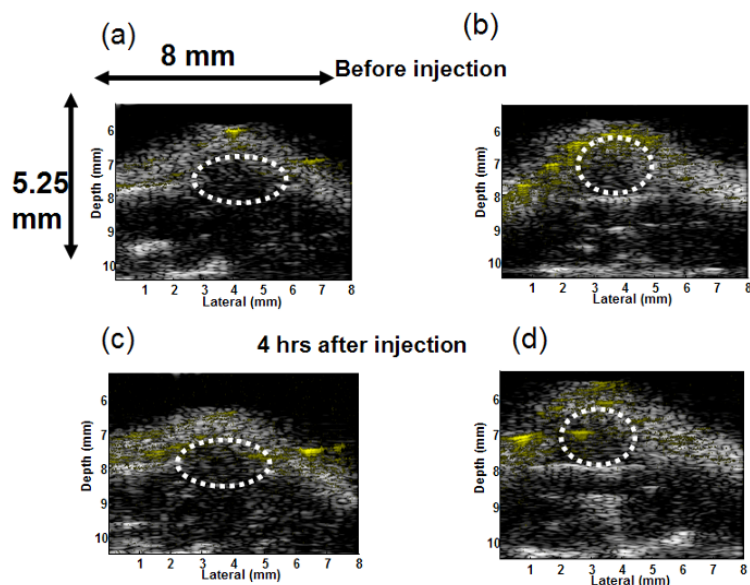


Figure 3-12. Images of OECM1 cells with AuNR₈₀₀ (control group) and AuNR₈₀₀-RGD4C injection obtained at 800 nm. (a) Before AuNR₈₀₀ injection. (b) Before AuNR₈₀₀-RGD4C injection. (c) 4 hours after AuNR₈₀₀ injection. (d) 4 hours after AuNR₈₀₀-RGD4C injection.

The targeting of RGD4C probes can be detailed examined. Fig. 3-13 shows the images from 10 minutes to 4 hours of OECM1 tumor after injection. From the images, the intensity of a small same region (dotted rectangular) is increasing as time. The region may be the cross section of big vessel of the angiogenesis within the tumor, and the probes diffused from the vessel to target endothelial cells on surrounding capillaries. The intensity can be up to 10 dB (Fig. 3-14) at 4 hours after injection, indicating the targeting efficacy of RGD4C probes on angiogenesis.

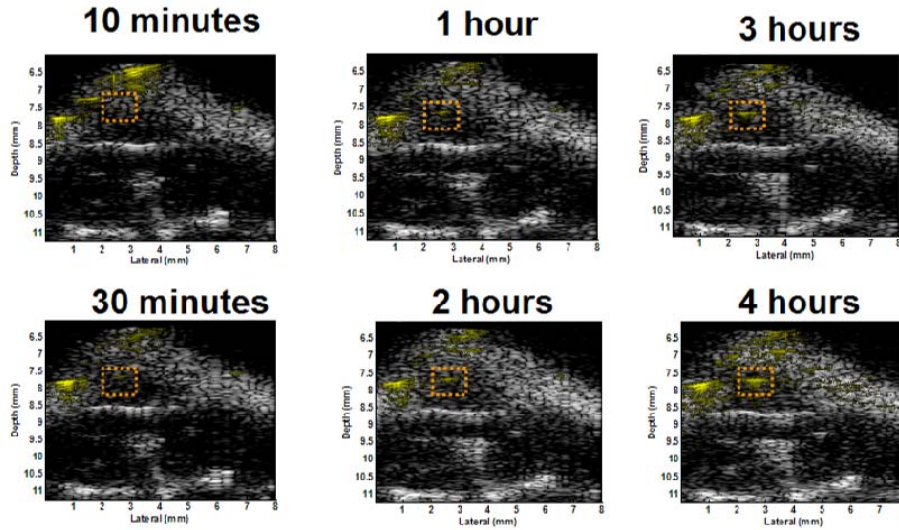


Figure 3-13. Images of RGD4C-probe injection from 10 minutes to 4 hours after injection.

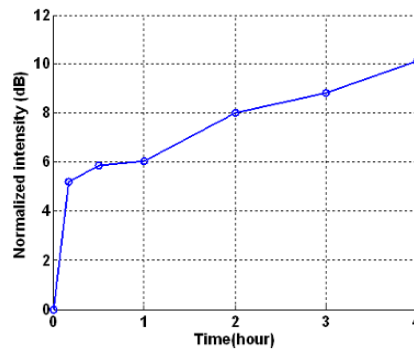


Figure 3-14. Normalized photoacoustic intensity within tumor region with RGD4C probes injection versus observation time.

3.4.3 Simultaneous targeting with mixed nanoprobe

Two types of probes, AuNR₈₀₀-RGD4C and AuNR₁₀₀₀-antiHER2, are injected into the mouse through the tail vein. The respective concentration of the two probes is 30 nM and the volume was 50 μ l, resulting in a mixed probe with a concentration of 30 nM and a volume of 100 μ l. Pure gold nanorods with the same concentration were injected into another mouse as a control. In order to monitor the targeting process, each mouse was imaged at several time points within 24 hours after injections. At each time point, an ultrasound image, and photoacoustic images at 800 nm and 1064 nm corresponding to the peak absorption wavelengths were acquired.

The right panel in Fig. 3-15 shows the US images obtained at different time

points. The outline of the mouse and the tumor area can be clearly seen in the ultrasound image, which reveals a darker intensity than the surrounding tissue. As for the photoacoustic images at 800 nm in the left panel of Fig. 3-15, it represents the binding of RGD4C probes. The photoacoustic intensity reaches its maximum at 6 hours. This can be the evidence of the specific targeting of RGD4C probes to angiogenesis. For images in the center panel, the intensity of images obtained at 1064 nm keeps increasing to 24 hours after injection, indicating the targeting of antiHER2 probes on OECM1 cells.

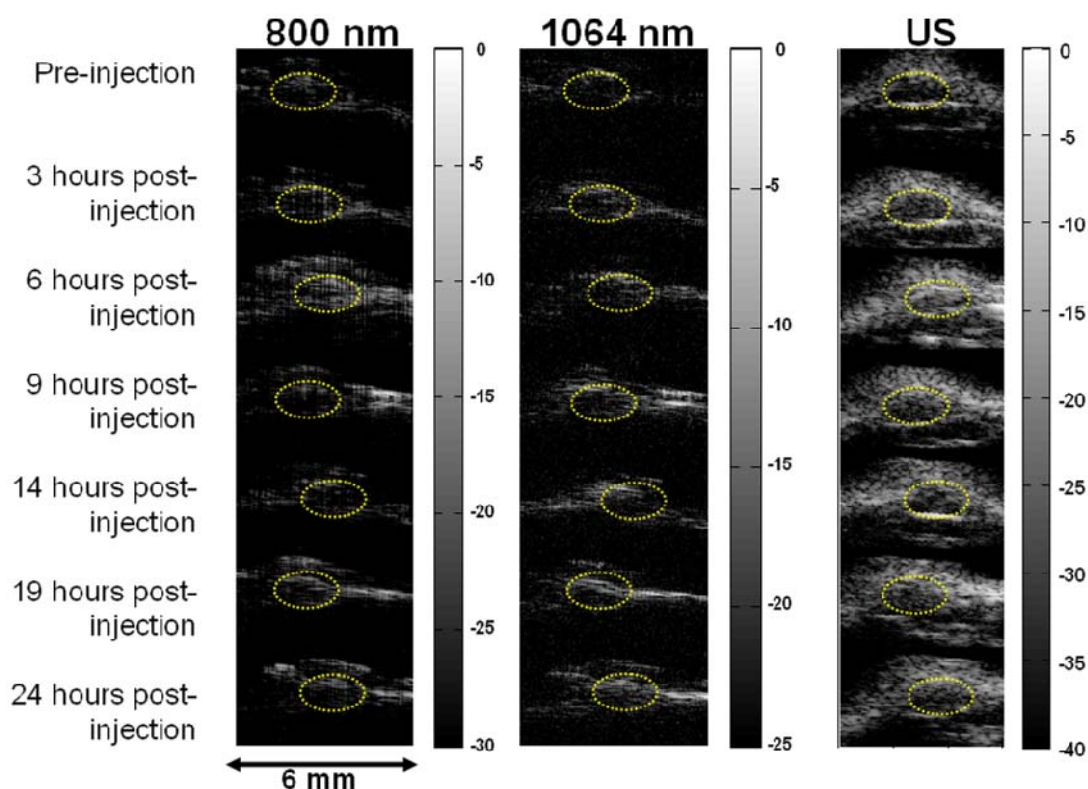


Figure 3-15. Ultrasound and 800 nm and 1064 nm photoacoustic images at different time points after mixed probes injection.

Fig. 3-16 shows the normalized photoacoustic intensity within tumor region versus observation time. As for the control group (AuNR₈₀₀ and AuNR₁₀₀₀ injection) shown in 3-16(b), the intensity decreases to the baseline after 5 hours post-injection, while the intensity of mixed probes injection image (Fig. 3-16(a)) at 800 nm shows a maximum of 6 dB at 5 hours and the image intensity at 1064 nm keeps increasing to 24 hours. The contrast between the mixed probes injection and the control group demonstrated the targeting ability of the probes on cancer cells. The increasing of 1064 nm photoacoustic intensity of mixed probes injection at 14 and 19 hours after injection maybe due to the cross influence between the two probes. It has been found

that the two probes own opposite electrical charges, so one targeting probe may lead to another due to the electrical binding.

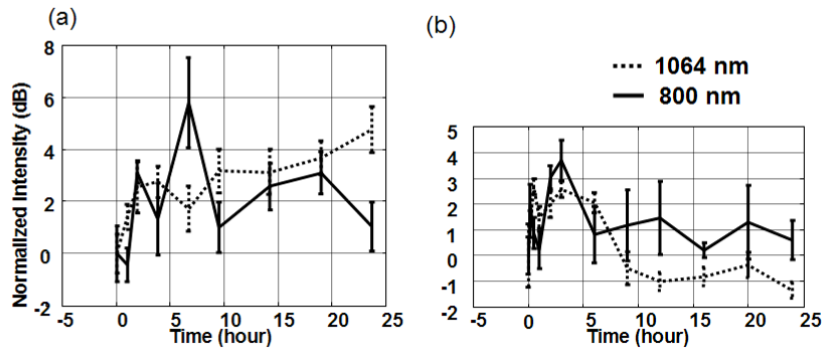


Figure 3-16. Normalized photoacoustic intensity within tumor region with mixed probes injection versus observation time. (a) Mixed probes injection: AuNR₈₀₀-RGD4C and AuNR₁₀₀₀-antiHER2. (b) Mixed pure gold nanorods injection: AuNR₈₀₀ and AuNR₁₀₀₀.

3.5 Discussion

3.5.1 Photoacoustic signals outside tumor

The photoacoustic signals outside of the tumor region that can be seen in Fig. 3-8, Fig. 3-9, Fig. 3-10 and Fig. 3-15 may be due to the signals from dermis (near the skin surface) and the fascia (with a layered appearance). The optical absorption of the dermis ranges from 2 to 10 cm^{-1} and may generate non-negligible photoacoustic signals [74]. Likewise, the fascia is between the subcutis and the muscle, and its location as shown in the histology (Fig. 3-17) correlates well with the photoacoustic images

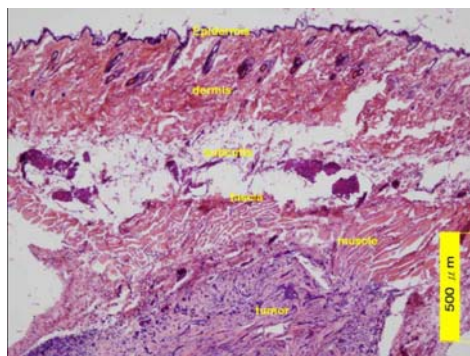


Figure 3-17. Histology with a scale bar of 500 μm. Epidermis, dermis, subcutis, fascia, and muscular layers were on the top of the tumor.

3.5.2 Concentration of targeted nanoprobe on tumor

The concentration of targeted gold nanorods can be estimated with the intensity increase of photoacoustic signals within the tumor region. The estimation is valid under the assumptions of linear relation between concentration and photoacoustic signal amplitude and negligible level of tumor signal intensity. From the mixed probes (50 μl, 30 nM AuNR₁₀₀₀-antiHER2 and 50 μl, 30 nM AuNR₈₀₀-RGD4C) injection result in Fig. 3-16, the intensity at 24 hours after injection increases by 4.19 dB. The effective concentration of AuNR₁₀₀₀-antiHER2 is 15 nM. Also, the intensity of tumor with subcutaneously injection of 30 nM AuNR₁₀₀₀ increases by 5.61 dB. Thus, the concentration of targeted AuNR₁₀₀₀-antiHER2 on tumor cell can be calculated as

$$4.19 \text{ dB} / 5.61 \text{ dB} \times 3 \text{ nM} = 1.62 / 1.91 \times 3 \text{ nM} = 2.54 \text{ nM}. \quad (3-1)$$

The percentage of targeted nanoprobe to the original injected nanoprobe is

$$2.54 \text{ nM} / 15 \text{ nM} = 16.96 \%. \quad (3-2)$$

Comparing to biodistribution result of taken out tumor at 24 hours after 30 nM AuNR₈₀₀-antiHER2 injection by Dr. D.-B. Shieh's lab in National Cheng Kung University, the percentage of nanoprobe in tumor to the injected amount is 18 %, which is close to the estimated result in (3-2). However, the aspect ratios and concentration of the nanoprobe used in photoacoustic measurement and biodistribution were different. More experiments need to be performed for obtaining a more accurate estimation of the quantity of targeted nanoprobe.

Atomic absorption (AA) spectroscopy analysis was also used to confirm the targeting efficacy of HER2-probes. After imaging, the tumor tissues with

AuNR₈₀₀-HER2 injection were surgically harvested from the mouse. The time point was 6 hours post-injection. The tumor tissues were scaled weight, homogenized, and then placed into a centrifuge tube containing 30 ml of nitric acid (12 M) for incubation for 3 days to permit complete dissolution of the tissue. The obtained liquid through was subjected to AA (UNICAM Solaar M6 series) analysis. The AA spectroscopy analysis results indicate that the Au ion within tumor tissues with HER2-probe injection is 9.1 $\mu\text{g au}^+$ per gram tissue weight, while that with AuNR₈₀₀ (control group) injection is 1.23 $\mu\text{g au}^+$ per gram tissue weight.

3.6 Concluding remarks

Utilizing the tunable optical absorption property of AuNRs, photoacoustic molecular imaging with multiple selective targeting has been demonstrated on oral cancer cells both *in vitro* and *in vivo*. The results reveal that information about multiple oncogene surface molecules of cancer cells can be obtained with photoacoustic techniques, which will help to improve our understanding of cancer cells better and to develop effective diagnosis tools as well as indications for effective treatments. This is considered as an improvement in molecular imaging compared to previous works on single targeting imaging. Note that multiple selective targeting can also be used to determine heterogeneous population of cancer cells in a lesion. Moreover, peptide RGD4C can be used to be conjugated with gold nanorods for angiogenesis targeting. The advantage of using this probe is that the probe can directly bind at tumor angiogenesis without extravasations from the capillaries, which is necessary for antibody conjugated probes to bind the cancer cells. The RGD4C targeted image can be combined with the flow estimation results by wash-in methods introduced in section 2.3 or ultrasound Doppler image for evaluating angiogenesis development. Simultaneous multiple selective targeting was performed utilizing mixed nanoprobe (i.e., AuNR₈₀₀-antiRGD4C and AuNR₁₀₀₀-antiHER2) in the same mouse by obtained photoacoustic image at respective laser wavelength corresponding to the peak absorption of the mixed two probes. The multiple targeting helps to recognize different cancer cells (e.g., OCEM1 and Cal27) because different cancer cells own different expressions to the probes. Finally, safe and effective gold-nanoparticle-based cancer diagnoses have great potential in the pharmaceutical industry and could also make significant contributions in the biomedical field.

CHAPTER 4 PHOTOACOUSTIC THERMAL IMAGING OF TARGETED THERMAL THERAPY

4.1 Gold nanoparticles assisted targeted thermal therapy

In chapter 3, bio-conjugated gold nanorods have been used to target cancer cells or angiogenesis for diagnosis in both morphology detection and oncogene sensing in molecular level. For treatment, a targeted thermotherapy method by heating the region of interest with the assist of gold nanorods was developed in this chapter. This can be achieved directly by irradiating the targeted nanoprobe on the cancer cells or angiogenesis with laser at wavelength corresponding to the peak absorption of the nanoprobe. The nanoprobe absorb the light energy and can heat the local region to tens of degree Celsius to reach hyperthermia of tumor [75], but without harming surrounding normal tissues on which no targeted nanoprobe. Gold nanorods based targeted photothermal therapy, which is also called laser-induced thermotherapy (LIT), has been demonstrated in cell cultures. Fig. 4-1 shows an optical microscopic image of LIT measurements of the OECM1 cells with HER2 expressions were targeted by AuNR₈₀₀-antiHER2 nanoprobe. The image was captured by Prof. C.-R.-C. Wang's lab in National Chung Cheng University. LIT was performed to evaluate effectiveness with a continuous solid-state laser with outputs at 785 nm. Damage to the cells was readily visualized by searching for any color change caused by staining with trypan blue upon cell death.



Figure 4-1. Optical microscopic images of LIT measurements. The cells within the laser beam

were dyed in blue with trypan, indicating the cells were killed by the hyperthermia caused by irradiating the targeted nanoprobe. The image was from Prof. C.-R.-C. Wang's lab in National Chung Cheng University.

4.2 Photoacoustic temperature monitoring

During the thermotherapy, monitoring the temperature changes of the tissues continuously is necessary to determine the treatment dosage for safety and efficacy concern. The demand of the monitoring system should achieve sub-millimeter in spatial resolution and accuracy less than 1 degree Celsius in temperature resolution [76]. Also, the system should be able to monitor the temperature continuously and in real-time. Direct measurement of the temperature using a thermocouple is the most accurate method, but it is invasive and is not suitable to apply on animals or human. Several non-invasive methods have also been proposed, including optics thermography, Magnetic resonance, and ultrasound. Optics thermography by using infrared light source can reach 0.1 degree Celsius in temperature resolution and real-time monitoring, but only superficial changes can be detected due to the limited penetration of optical energy. Magnetic resonance system has high spatial and temperature resolution, but it is not real-time [76]. Ultrasound provides a good spatial resolution, excellent penetration, and real-time monitoring, but the temperature resolution is not accurate (> 5 degree Celsius) [77].

Photoacoustic methods for temperature monitoring have been developed in the applications including ophthalmologic laser surgery [78], and cancer therapy [79]. In the study, the goal is to integrate the photoacoustic imaging system for temperature monitoring and the photothermal therapy system in small animal models.

4.2.1 Linearity between photoacoustic amplitude and temperature

The intensity of photoacoustic signals and the temperature of the region of interest have been found linearity correlated in an *in vitro* study [78, 79]. Recalling equation (1-7), the initial photoacoustic pressure rise ($t = 0$) $P(z)$ can be written as:

$$P(z) = \left(\frac{\beta c_s^2}{\rho C_p} \right) \mu_a \Phi(z) = \Gamma \mu_a \Phi(z), \quad (4-1)$$

where the thermal volume expansion coefficient β , the speed of sound c_s , and the heat

capacity at constant pressure C_p can be integrated into a dimensionless Grüneisen parameter Γ . The thermal expansion coefficient of volume is a linear function of temperature for water-based tissue in the range of 10 and 55 °C [79] and the speed of sound and the heat capacity are also functions of temperature. The resulting Grüneisen parameter of water is linearly proportional to the temperature T [76], which can be represented as

$$\Gamma = (A + BT), \quad (4-2)$$

where A and B are constants. The equation (4-1) can be rewritten as:

$$P(z) = (A + BT(z))\mu_a\Phi(z), \quad (4-3)$$

and this can be rearranged as

$$T(z) = -\frac{A}{B} + \frac{P(z)}{B\mu_a\Phi(z)} = C + D\frac{P(z)}{P(z,t_0)}, \quad (4-4)$$

where $C = -\frac{A}{B}$, $D = \frac{A + Bt_0}{B}$, $P(z,t_0)$ is the photoacoustic signal recorded at an initial known temperature. Equation (4-4) means that the temperature is linearly correlated with photoacoustic signal amplitude, and once the initial temperature t_0 is known, the temperature distribution $T(z)$ can be evaluated from the recorded photoacoustic signal $P(z)$ and $P(z,t_0)$ during thermotherapy.

Fig. 4-2 is the Grüneisen parameter of water at different temperature (solid line) and the linear fit result (dotted line), in which the constant A and B for water in equation (4-2) were found 0.016 and 0.0046, respectively. In the subsequent experiments, soft tissues (eq., tumor) with water as their mainly composition (more than 70%) is our focus. Therefore, A and B of water will be adopted in equation (4-4) for calculation of temperature distribution.

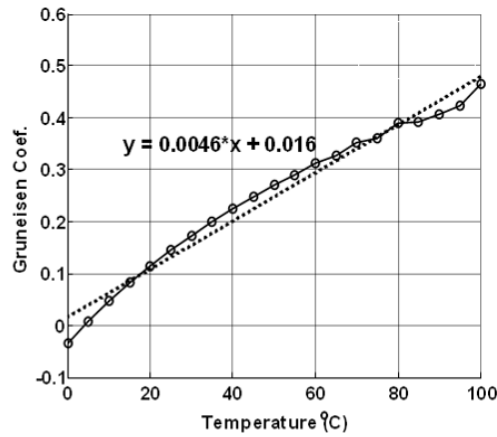


Figure 4-2. Grüneisen parameter of water versus temperature (solid line) and the linear fit (dotted line).

The relation between photoacoustic signal amplitude and temperature was also verified experimentally. Fig. 4-3 [80] reveals good linear relationship between the temperature and photoacoustic amplitude of gold nanoparticles, but there is a deviation when the temperature was higher than 65 °C. The deviation when the temperature is above 65 °C may be due to the property of the thermal volume expansion coefficient, which will not be a linear function of temperature if the temperature goes beyond the range of 10 and 55 °C [79]. However, the end point of temperature for thermotherapy are generally in the range of 41-47 °C, which is much lower than 65°C. Therefore, this non-linear deviation of the photoacoustic pressure profile would not affect the applicability of this study.

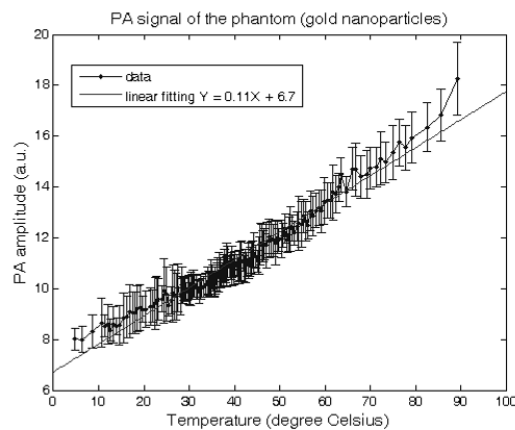


Figure 4-3. The linear relation between temperature and photoacoustic amplitude of gold nanoparticles [80].

4.2.2 Integration of photoacoustic imaging system and photothermal

therapy system

The diagram of the integration system is shown in Fig. 4-4, which consists of a photoacoustic imaging system using pulsed wave (PW) laser (CF-125, SOLAR TII, Minsk, Republic of Belarus) and a photothermal therapy system using a continuous wave (CW) diode laser (808 nm, Newport, CA, USA) to heat the tumor for treatment of tumor. The power of the laser can be adjusted by a driver (5600-65, Newport, CA, USA) to a maximum of 10 W. The photoacoustic imaging system is close to the setup for *in vivo* imaging in Fig. 3-7, while the photothermal therapy system uses diode lasers, whose operating wavelength can be chosen according to the peak absorption wavelength of the targeted gold nanorods. The diode laser can deliver laser power up to 10 watt. Both PW and CW laser beams will be coupled into fibers. The PW laser fiber was fixed in a stage that can be driven by a motor for image scanning. The CW laser beam is designed to be about 5 mm in diameter in order to illuminate the whole tumor area (< 5 mm in diameter). During thermotherapy, the position of the mouse was fixed under general anesthesia with supply of mixture gas of isoflurane/ oxygen.

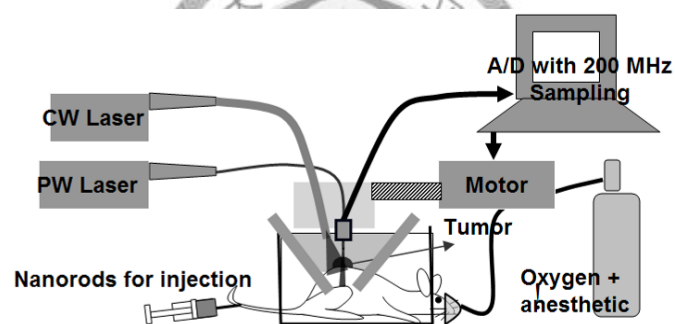


Figure 4-4. Integrated system with photoacoustic imaging system and laser thermal therapy system.

4.3 Photoacoustic quantitative thermal imaging

To obtain quantitative temperature distribution during photothermal therapy, two photoacoustic images of tumor when CW laser turned off (pre-treatment) and on (during treatment) were recorded. The image when CW laser turned on was acquired after about 1 to 2 minutes of irradiation for the temperature within the tumor reaching a stable level. An ultrasound image of the tumor was also acquired to recognize the tumor outlines. Oral cancer cell, OECM1, induced on the back of Nod-scid mice was adopted as the tested animal model, and nanorods/nanoprobes to be injected were

AuNR₈₀₀-antiHER2, which has been demonstrated that its specific binding ability to OECM1 cells. The optical irradiation wavelengths were 800 nm for PW laser and 808 nm for CW laser, respectively. In calculating temperature distribution, the initial (pre-treatment) temperature t_0 was measured at the region of interest (i.e., tumor) by a needle thermocouple (EDL NCF-06GS4TL3M, Danville, VA, USA) and a digital multimeter (Fluke Model 189 True RMS Multimeter, Everett, WA) with accuracy of 0.1 °C. And it was assumed that the initial temperature was uniformly distributed within the tumor region. With this assumption, C and D in equation (4-4) can be obtained. Therefore, the temperature distribution can be calculated with equation (4-4) by recording pre-treatment image (i.e., $P(z, t_0)$) and image during treatment (i.e., $P(z)$). Also, the temperature of the tumor region during thermal therapy was recorded with the thermocouple to be compared with the calculation results from the photoacoustic signals.

In section 4.3.1, pure (i.e., non-conjugated) gold nanorods, AuNR₈₀₀, were directly injected subcutaneously into the tumor. The targeted photoacoustic imaging and targeted photothermal therapy were performed by injection of AuNR₈₀₀-antiHER2 through the tail vein in section 4.3.2.

4.3.1 *In vivo* studies: subcutaneous injection

For subcutaneous injection, pure gold nanorods, AuNR₈₀₀, were directly injected into the tumor with a concentration of 3 nM and a volume of 20 μ l. CW laser power was 0.76 W/cm². Fig. 4-5 shows the four photoacoustic images of the tumor at different conditions. Fig. 4-5(a) and (b) were respectively obtained at CW laser turned off and on before the gold nanorods injection, while Fig. 4-5(c) and (d) were obtained after injection, CW laser turned off and on, respectively. The dotted circles indicate the tumor region to be concerned. The intensities within tumor region in Fig. 4-5(a) and (b) exhibit no apparent difference, indicating the tissue temperature did not rise due the heating by CW laser when there is no effective optical absorbers, gold nanorods. Fig. 4-5(c) shows a noticeable increasing in photoacoustic signals, including not only the tumor region but also the skin surface and surrounding tissue outside the tumor region (arrows) resulted from the existing of gold nanorods. The increasing at region outside tumor may be due to the leakage of the injected gold nanorods. In Fig. 4-5(d), the intensity further increase, reflecting the temperature rise dependent signal change. Some multi-reflection of the acoustic signal within the tumor and tissue can be observed under the tumor region.

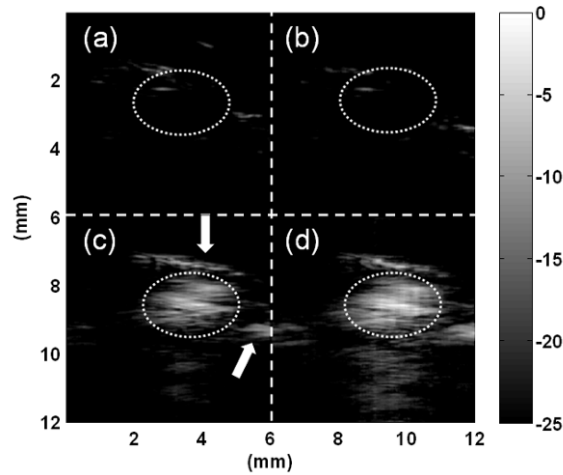


Figure 4-5. Photoacoustic images of tumor with subcutaneous injection of gold nanorods. (a) Before nanorods injection, CW laser off. (b) Before nanorods injection, CW laser on. (c) After nanorods injection, CW laser off. (d) After nanorods injection, CW laser on.

In obtaining temperature distribution by using equation (4-4), the ratio of signal amplitude during treatment $P(z)$ to signal before treatment $P(z, t_0)$ was calculated with pixel-to-pixel corresponding to the same site in the two images. However, the location of the tumor may slightly vary due to the motion of the animal during the image acquisition, and discrepancy between the two images may occur. Also, optical energy of PW for photoacoustic generation may vary. Thus, the signal amplitudes at corresponding region of the pre-treatment image and image during treatment differ due to not only the temperature change but also the location and optical energy variation, and error occurs in temperature calculation. To reduce this error, the ratio of $P(z)$ to $P(z, t_0)$ was obtained by using a small region mean amplitude calculation instead of pixel-to-pixel calculation (0.0075 mm and 0.02 mm in axial and lateral direction, respectively). For example, the mean amplitude of a 3-times-3 square region of the image was used as the amplitude at the center pixel of the square region in calculating the ratio. This action is like averaging the image intensity with neighboring region to reduce the calculation error

.Fig. 4-6 shows the quantitative temperature distributions of the tumor with gold nanorods injection during the thermal therapy by using Fig. 4-5(c) and (d). The thermal images were multiplied by a threshold map determined from the signal amplitude in Fig. 4-5(c), so most photoacoustic signals distributed within the tumor region will be presented and those outside the tumor will be displayed at zero level. Fig. 4-6(a) is the pixel-to-pixel calculation result, which exhibits a temperature distribution mostly at range 30 to 60 °C and maximum value above 120 °C at several small regions. The result is not reasonable because the temperature during

thermal therapy was measured as $40\text{ }^{\circ}\text{C}$, and these unreasonable high values are caused by the location and optical energy variation mentioned previously. Fig. 4-6(b) and (c) are the results of 3-times-3 and 5-times-5 region ($0.0225\text{ mm} \times 0.06\text{ mm}$ and $0.0375\text{ mm} \times 0.1\text{ mm}$ in axial and lateral direction) mean amplitude calculation, respectively. The maximum calculated temperatures decrease to about $100\text{ }^{\circ}\text{C}$, indicating the eliminating of the errors by small region averaging. However, the results were not satisfying because some region still exhibited temperature above $100\text{ }^{\circ}\text{C}$, which will cause the denaturalization of tissues but not observed in the tumor region.

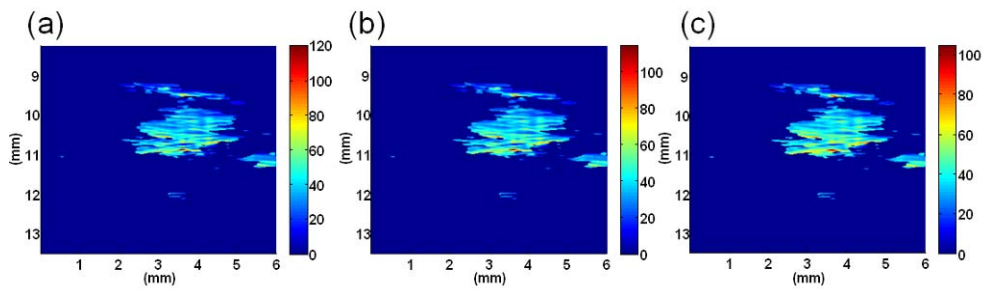


Figure 4-6. Thermal imaging calculated from Fig. 4-5(c) and (d). The images are under threshold by signal intensity in Fig. 4-5(c). Colorbars show the temperature in Celsius. (a) Temperature distribution using pixel-to-pixel calculation. (b) Temperature distribution using 3-times-3 window calculation. (c) Temperature distribution using 3-times-3 window calculation.

To further eliminate the calculation error, the original images, $P(z)$ and $P(z, t_0)$, were convoluted with lowpass filters in axial and lateral direction. The lowpass filtering is also an averaging action that will reduce the influence of the variation. The images at the four conditions in Fig. 4-5 after lowpass filtering are shown in Fig. 4-7. Fig. 4-7(a) and (b) show no significant signal as Fig. 4-5(a) and (b). Fig. 4-7(c) and (d) reveal blurred versions of the original images after gold nanorods injection in Fig. 4-5(c) and (d).

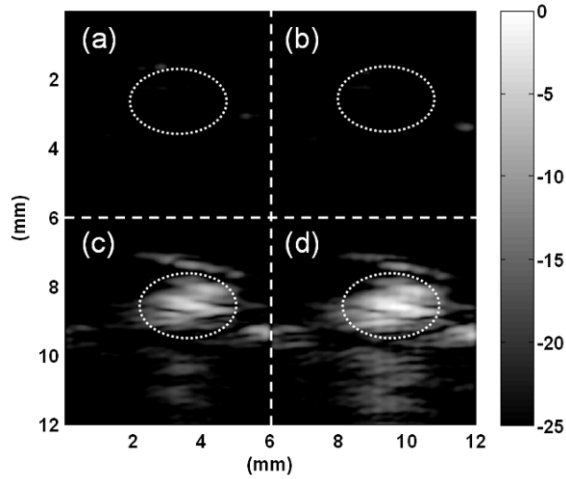


Figure 4-7. Lowpass filtered photoacoustic images of tumor with subcutaneous injection of gold nanorods. (a) Before nanorods injection, CW laser off. (b) Before nanorods injection, CW laser on. (c) After nanorods injection, CW laser off. (d) After nanorods injection, CW laser on.

Fig. 4-8 illustrates the thermal imaging calculated by using blurred photoacoustic images in Fig. 4-7(c) and (d). The pixel-to-pixel, 3-times-3, and 5-times-5 small region amplitude calculation results exhibit similar results, where the maximum temperature is about 80 °C and most tumor region show a temperature range of 40 to 50 °C. The results coincide with the temperature measured by thermocouple during CW laser irradiation. According to these results, the lowpass filtering will be used in the following section for quantitative temperature calculation.

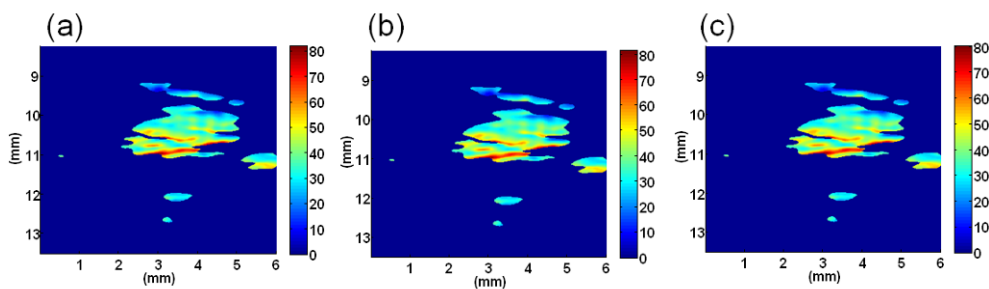


Figure 4-8. Thermal imaging calculated from Fig. 4-7(c) and (d). The images are under threshold by signal intensity in Fig. 4-7(c). Colorbars show the temperature in Celsius. (a) Temperature distribution using pixel-to-pixel calculation. (b) Temperature distribution using 3-times-3 window calculation. (c) Temperature distribution using 3-times-3 window calculation.

4.3.2 *In vivo* studies: tail vein injection

The real targeted photoacoustic imaging and targeted thermal therapy need tail injection of the nanoprobes. The free nanoprobes within the circulatory system of small animal will find and bind at tumor region for subsequent imaging and therapy. In this section, Nod-scid mice bearing OECM1 cancer cells and AuNR₈₀₀-antiHER2 were used as in chapter 3 to verify the capability of the integrated imaging and therapy system illustrated in Fig. 4-4. The CW laser power was 0.32 W/cm².

The tumor was imaged at CW laser turned off and on before the nanoprobes injection. Then AuNR₈₀₀-antiHER2 with a concentration of 30 nM and a volume of 100 μ l were injected into the mouse through the tail vein. After 24 hours, the tumor was imaged again at CW laser turned off and on. The measurement time point, 24 hour post-injection, was chosen according to the result in Fig. 3-16. The targeting number of nanoprobes on tumor was found reaching its maximum and thus the best treatment time point.

Fig. 4-9 is the fusion image of ultrasound (grayscale) and photoacoustic (pseudo-color) images. The images obtained at four different conditions were cascaded to be compared. No significant difference between the tumor regions (yellow dotted circles) of the two images before nanoprobe injection whether the CW laser was turned off or on (Fig. 4-9(a) and (b)). It inferred that no hyperthermia effect can be achieved if no nanoprobe exists within the tumor. In the other way, a significant increase in the photoacoustic amplitude was noted between Fig. 4-9(c), image at 24 hours post-injection and CW laser off, and the two foregoing images. This result indicated that the targeting of nanoprobes on the tumor and increasing in photoacoustic signal amplitude. Prominent difference existed between Fig. 4-9(c) and (d), which was due to CW mode laser irradiation to provoke temperature rise and resulted in tissue hyperthermia. After the CW laser was turned off again, the photoacoustic intensity within tumor slightly decreases, indicating the temperature decreases because of the removal of heating source.

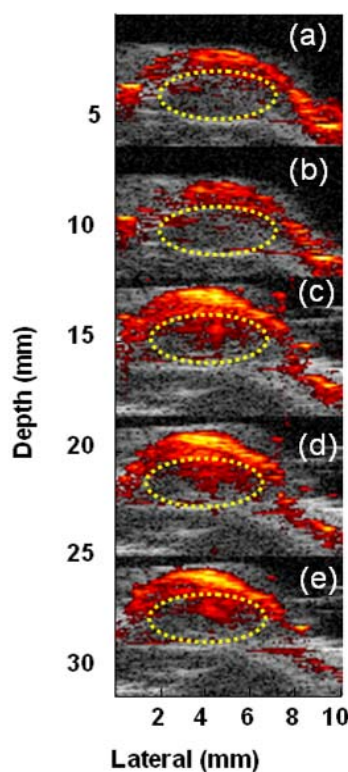


Figure 4-9. Fusion result of ultrasound pulse/echo (gray) and photoacoustic (pseudo color) images obtained at different conditions. (a) Before injection, CW laser off. (b) Before injection CW laser on. (c) 24 hours post injection, CW laser off. (d) 24 hours post injection, CW laser on. (e) 24 hours post injection, CW laser re-off.

The intensities within the tumor region were compared by averaging the intensities of three distinct slices of the tumor. The mean value and the standard deviation were plotted in Fig. 4-10, in which the four cases correspond to Fig. 4-9(a)-(e). The intensities were normalized to that of case 1 (subtracting the mean intensity) to reveal the intensity difference between cases. The image intensity of pre-injection, CW laser on case (case 2) is slightly lower than that of CW laser off case maybe due to optical energy deviation of PW laser. Nevertheless, the intensities of case 1 and 2 are basically not distinguishable because of the overlap of their standard deviations, inferring no temperature rise. The intensity of case 3 increases by about 4 dB from case 1, indicating the enhanced photoacoustic signal from targeted nanoprobes. There is further intensity increase from case 3 to case 4, which results from the photothermal effect on tumor tissues. The intensity decreases by 1 dB from case 4 to case 5 due to the CW laser turned off. The overshoot decreasing may be caused by the variation of pulsed laser energy.

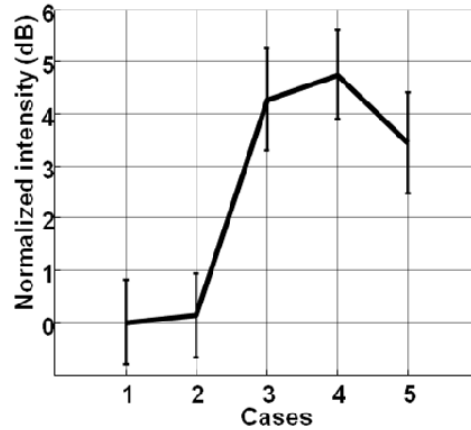


Figure 4-10. Averaged image intensity at different conditions in Fig. 4-10. Case (1): Before injection, CW laser off. Case (2): Before injection CW laser on. Case (3): 24 hours post injection, CW laser off. Case (4): 24 hours post injection CW laser on. Case (5): 24 hours post injection CW laser re-off.

Fig. 4-9(c), (d) and (e) were used for temperature calculation during thermal therapy with targeted gold nanoprobes. The temperature distribution of the tumor region was calculated by equation (4-4) with pre-treatment temperature of 26 °C measured by thermocouple. The result from Fig. 4-9(c) (CW laser off) and Fig. 4-9(d) (CW laser on) was shown in Fig. 4-11, which reveals a maximum temperature above 40 °C at the center of tumor region (dotted circle) and generally higher temperature (30 to 40 °C) within the tumor than outside region. Fig. 4-11(b) is the thermal image from Fig. 4-9(c) (CW laser off) and Fig. 4-9(e) (CW laser re-off), showing a generally lower temperature distribution within the tumor than Fig. 4-11(a).

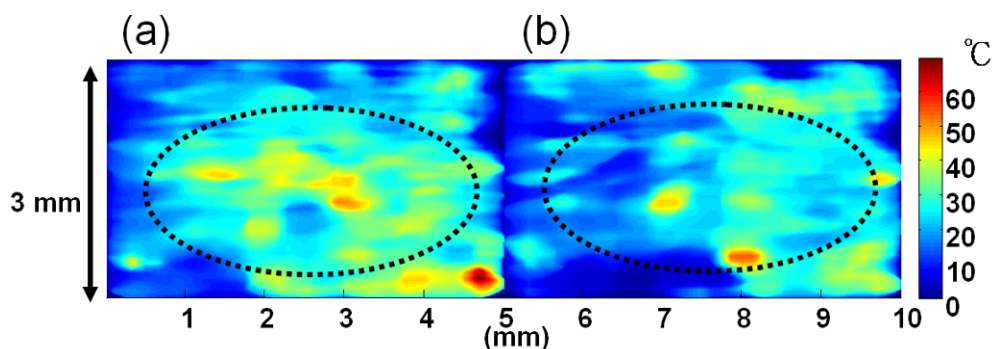


Figure 4-11. Thermal image of tumor with targeted gold nanorods. Dotted circle indicates the tumor region, and colorbar represents temperature in Celsius. (a) Thermal image from Fig. 4-9(c) and (d). (b) Thermal image from Fig. 4-9(c) and (e).

The tumor after the experiments was taken out for pathologic analysis. The

results show the necrosis of the tumor cell, in which the cell nuclei are reduced or vanished (red arrows in Figure 4-12(a) and (b)), while the fibroblast cells (yellow arrows in Figure 4-12(a)) around the tumor and peripheral follicles (green arrows in Figure 4-12(b)) beneath the tumor are preserved. Figure 4-13 compares the pathologic results of tumor without treatment (Figure 4-13(a)) and tumor after the targeted thermal therapy (Figure 4-13(b)). The former one exhibits a complete contour while numerous cavities can be found in the later one after the therapy. The results in Figure 4-12 and Figure 4-13 demonstrated the efficacy of target thermal therapy to tumor cells without damaging other normal tissues.

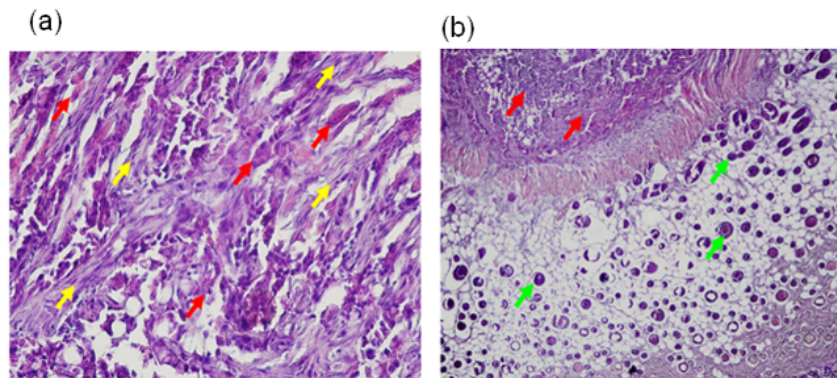


Figure 4-12. Pathology of tumor [80]. (a) The necrosis of tumor cells (red arrows) and preservation of the fibroblast cells (yellow arrows). (b) The necrosis of tumor cells (red arrows) and preservation of the peripheral follicles (green arrows).

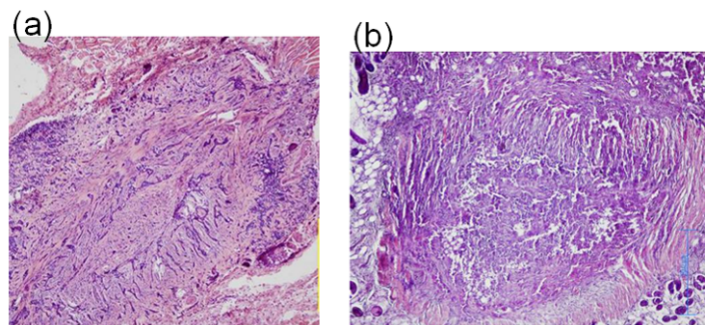


Figure 4-13. Pathology of tumor [80]. (a) Tumor without treatment. (b) Tumor after targeted thermal therapy.

4.4 Discussion

There are several problems that need to be fixed in obtaining quantitative thermal

imaging. First, the initial temperature t_0 , which is measured by a thermocouple at one point within the tumor, is actually position dependent. The assumption of a uniform distribution of temperature may be not valid in practice. Second, the constant A and B in equation (4-2), which relate temperature and Grüneisen parameter, should be for real tissues (e.g., tumor tissues), not for water. A calibration experiment according to equation (4-3) needs to be performed to obtain A and B of real tissues by measuring photoacoustic signal of real tissues at different temperatures. A precise quantitative temperature distribution can be expected. Third, breath caused motion of tumor between pre-treatment and during-treatment acquisition is hard to avoid. Correlation coefficients between the two images have been calculated for correction of the motion. The maximum moving correlation coefficient between Fig. 4-10(c) and (d) was 0.69, indicating there may be some motion out image plane. A faster (high frame rate) system is required to acquire the two images in shorter period to reduce the motion influence.

4.5 Concluding remarks

A non-invasive real-time photoacoustic technique allowing for combined photoacoustic imaging and thermal therapy system is presented. This integrated system can image the targeted nanoprobe on tumor, and provide targeted thermal therapy on tumor without harming surrounding normal tissues. Furthermore, the recorded photoacoustic signal can be used to measure the temperature during photothermal therapy before and during treatment. It can assure the efficacy and control the safety of thermotherapy. In both *in vivo* study with subcutaneous injection and tail vein injection, the photoacoustic intensity within the tumor region was found correlated with the temperature of measured area. Quantitative thermal imaging was also obtained. The temperature rise of the tumor with the targeted gold nanorods irradiating by CW laser was apparently more enhanced than that of tumor by the same CW laser irradiation before nanoprobe injection. The temperature rise shown in the thermal imaging can achieve hyperthermia of tumor cells, and pathological results of the taken out tumor after therapy also confirm the necrosis of tumor cells but preservation of normal tissue. Targeted thermal therapy and photoacoustic temperature monitoring were both demonstrated. The results of this study suggest that photoacoustic signal can be used not only for imaging purpose but also to monitor the temperature during photothermal therapy in real time.

CHAPTER 5 PHOTOACOUSTIC SUBBAND IMAGING FOR CONTRAST IMPROVEMENT

5.1 Introduction

In this chapter, a subband based method that can further enhance the contrast between the contrast agent and the tissue is proposed. For example, the detection sensitivity of gold nanoparticles within vessels for flow estimation and bio-conjugated gold nanorods targeted on tumor will be degraded due to the penetration dependent incident optical energy decay, which results from the optical absorption of blood hemoglobin, epidermis, dermis, subcutaneous tissues, and so on. Also, high optical scattering in tissues will decrease the optical energy of incident laser pulses when arriving on the region of interest. The principle of the subband method is explained as follows. The absorption difference not only determines the contrast but also results in various frequency components, which can be employed to suppress the tissue signal. When laser pulses irradiate the optical absorber, the energy is absorbed and decays with the distance from the irradiation. It can be comprehended that the laser energy decays more rapidly if the absorber has a higher absorption. The decay profile along the depth infers the pressure distribution, which forms the acoustic waveform to propagate outward. As a result, the propagated photoacoustic signal from object with higher absorption will contain higher frequency portions since the pressure waveform which decays rapidly represents higher frequency. Thus, the photoacoustic signal can be detected by a wideband detector and its frequency spectrum can be divided into several subbands. The contrast can be enhanced by choosing the subbands in which the frequency components of the object with higher absorption are larger than those with lower absorption.

Simulations and experiments of the photoacoustic signals from various absorptions are performed, and both forward mode and backward mode for detection are adopted. In addition, a proposed method of summing weighted subband images for contrast enhancement⁶ is used on the experimental data. At last, the two detection modes are compared to clarify the influence of the directivity of the wave propagation

on the frequency portions of the received signals, and the possibility to reconstruct the absorption coefficients by using the frequency information will be discussed.

5.2 Relation between optical absorption and photoacoustic signal frequency

5.2.1 Numerical simulations

Simulations have been performed to verify the relation between the frequency spectrums of the photoacoustic signal of absorbers and their absorptions. To simulate the detected photoacoustic signals, a diffusion equation describing the optical transport and the following wave equation were utilized. The diffusion equation was given by [81]:

$$\nabla \cdot \kappa(r) \nabla \Phi(r) + \mu_a(r) \Phi(r) = q_0(r). \quad (5-1)$$

$\kappa(r) = 1/(3\mu_a(r) + 3\mu'_s(r))$ is the diffusion coefficient, $\mu_a(r)$ and $\mu'_s(r)$ are the absorption and reduced scattering coefficients, respectively, $q_0(r)$ is the isotropic light source from the laser. After the resulting laser fluence and the further energy deposition, wave equation was applied to achieve the simulation. The wave equation can be represented as [82]

$$\frac{\partial^2 p(r;t)}{\partial t^2} = c_s^2 \rho \frac{\partial^2 p(r;t)}{\partial r^2}. \quad (5-2)$$

Based on the characteristics of water, the sound velocity c_s was 1500 m/s, the density ρ was 1, and the Grüneisen coefficient was set to be 0.11. Rectangular optical absorbers with size of 1.5 mm in width and 4.5 mm in thickness were placed at 1.5 mm in depth from the laser irradiation surface. Absorbers with three various absorption coefficients were simulated: 20 cm⁻¹, 8 cm⁻¹, and 2 cm⁻¹, and the scattering coefficient was set to 50 cm⁻¹. The background region, which simulates the biological tissues, was set to be 50 cm⁻¹ in scattering and 0.01 cm⁻¹ in absorption. The anisotropic factor was set to be 0.9. The propagated photoacoustic signals were recorded with a sampling rate of 200 MHz by a point detector located at center in lateral and 7.5 mm in depth for forward detection and 0 mm (i.e., at the irradiated surface) for backward detection. The diagram of the absorber and the point detector

distribution is shown in Fig. 5-1.

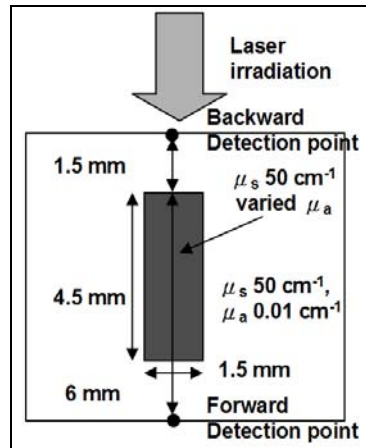


Figure 5-1. The diagram of the absorber and the detection point for simulating the photoacoustic signal propagation.

Fig. 5-2 shows the simulation results of objects with varied absorption coefficients. Objects with homogeneous absorption were simulated to observe the effects of varied absorptions on the energy depositions, signal profiles, and frequency spectrums. Fig. 5-2(a), (b), and (c) are the normalized energy depositions of rectangular objects with absorption coefficients of 20 cm^{-1} , 8 cm^{-1} , and 2 cm^{-1} , respectively. The optical illumination is from the top and the energy decays downward.

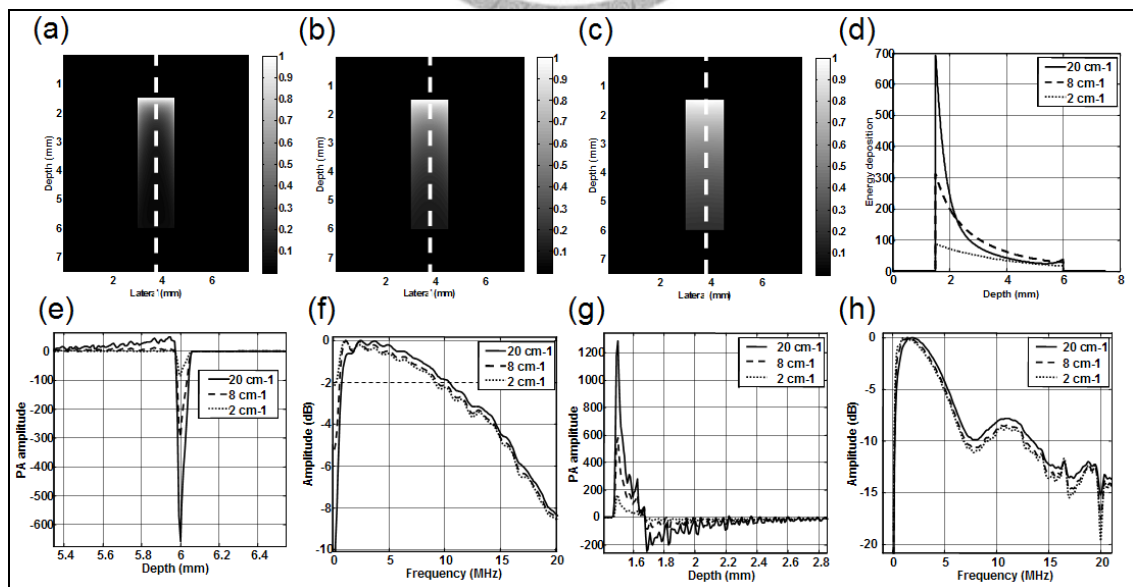


Figure 5-2. The simulation results of phantoms of varied absorption. (a) Normalized energy

deposition of an absorber with absorption 20 cm^{-1} . (b) Normalized energy deposition of an absorber with absorption 8 cm^{-1} . (c) Normalized energy deposition of an absorber with absorption 2 cm^{-1} . (d) Energy deposition profiles along the dashed lines in (a), (b), and (c). (e) Propagated photoacoustic signals detected by using forward mode. (f) Frequency spectrums of the three absorbers in forward mode. (g) Propagated photoacoustic signals detected by using backward mode. (h) Frequency spectrums of the three absorbers in backward mode.

Fig. 5-2(d) shows the profiles along the dashed lines in Fig. 5-2(a) to (c) before the amplitude normalization. It is obvious to find that the rates of decay increase as the absorption coefficients. Fig. 5-2(e) shows the photoacoustic profiles detected by forward mode, where the receiver was located at about 7.5 mm away from the irradiation surface. The absorption variations influence not only the amplitudes of the signals but also the waveforms. The difference in waveforms implies various frequency decompositions. To verify the relation between frequency and absorption, the photoacoustic waveforms were analyzed in frequency domain. Fig. 5-2(f) is the result of the frequency domain analysis, which shows that the spectrums of the photoacoustic signals obtained from varied absorption have distinctions in peak frequency (i.e., the frequency where the amplitude is maximal) and the bandwidth. Fig. 5-2(g) and (h) are the photoacoustic waveforms detected by using backward mode and the corresponding frequency spectrums, which also verify the relation between the absorption and the frequency component. Therefore, subband images can improve contrast by choosing proper band-pass filters, in which the spectrum difference is apparent in the chosen bands.

The frequency-absorption relation by numerical simulation is shown in Fig. 5-3. The positive parts of time-domain profiles in Fig. 5-3(a) reveal the signal waveform deference from different optical absorption. The profiles of higher absorptions have a more pronounced positive rise than those of lower absorptions. The frequency spectra in Fig. 5-3(b) show larger peak frequencies and wider bandwidths of higher absorptions than lower ones. The calculated peak frequencies, -6 dB and -20 dB bandwidths are plotted as a function of optical absorption coefficients in Fig. 5-3(c), which demonstrates the hypothesis that higher absorption leads to higher frequency (larger peak frequency and wider bandwidth) photoacoustic signals.

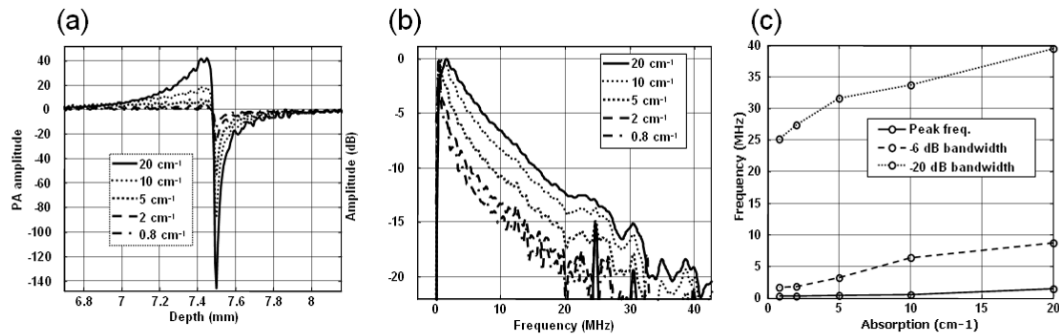


Figure 5-3. The simulation (forward mode) results of phantoms of varied absorption. (a) Photoacoustic signals detected by hydrophone. (b) Frequency spectra of the photoacoustic signals. (c) Peak frequencies, -6 dB, and -20 dB bandwidths vs. absorption coefficients.

5.2.2 Phantom experiments

The schematic diagram of the photoacoustic experimental setup is shown in Fig. 5-4. The phantoms were made of agar, which has similar characteristics to biological tissue with sound velocity of 1500 m/s. The phantom was manufactured by first preparing a pure 2 % agar (0710, Amresco, OH, USA), which has absorption coefficient close to 0 cm⁻¹ at 1064 nm and was used as a bed. Then, small pieces of agar with added graphite powder (282863, Aldrich, WI, USA) of various mass (thus various concentrations and absorption coefficients in the phantom) were arranged on the bed. The final step was to put a cover over by pure agar phantom to finish the manufacturing. The diagram of manufacturing process is shown in Fig. 5-4(a). The absorption coefficients at 1064 nm of the agars with graphite powder were from 0.84 cm⁻¹ to 100 cm⁻¹, which were measured by a spectrophotometer (v570, Jasco, MD, USA).

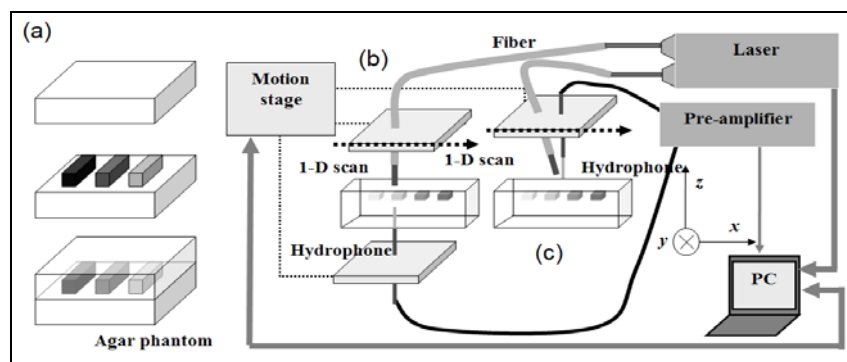


Figure 5-4. The diagram of experimental setup for photoacoustic imaging. (a) Phantom manufacture. (b) Forward mode. (c) Backward mode.

Here two detection modes, forward mode and backward mode, were used to acquire photoacoustic signals. In forward mode (as shown in Fig. 5-4(b)), the detector and the irradiating light source were aligned along the z-axis to be face to face vertically, so the phantom to be imaged could be placed between the detector and the light source to be scanned along the x-direction. In backward mode (Fig. 5-4(c)), the detector was placed along the z-axis, and the light source was arranged to have a small angle off the detector for achieving a confocal statement of the detection pattern and the illuminated volume on the samples along the x-axis. In both modes, the detector and the light source were fixed with a holder to be moved simultaneously.

A frequency-doubled Nd:YAG laser (LS-2132U, LOTIS TII, Minsk, Belarus) operating at 1064 nm with a pulse duration of 5 ns was used for optical excitation. The pulse repetition rate was 15 Hz. The laser beam was coupled into a 1000- μm fiber (FT-1.0-UMT, Thorlabs, Newton, NJ, USA) to irradiate a round light area of diameter about 3 mm. The irradiated laser energy density was 4.72 mJ/cm². A high sensitivity hydrophone (MH28, Force technology, Denmark) with flat spectrum from 0 to 20 MHz was used for photoacoustic signal detection. A precision ultrasonic motor (NR-8, Nanomotion, Israel) controlled by a personal computer was used for image scan with a step size of 0.1 mm. The agar phantom was immersed in a water tank filled with deionized water for photoacoustic measurements. The acoustic waveforms were amplified by an acoustic amplifier (5073PR, Panametrics, Waltham, MA, USA) and then recorded by a data acquisition card (CompuScope 14200, Gage, Lachine, QC, Canada) at a 200-MHz sampling rate. The acquired data were stored in a personal computer for subsequent data analysis.

Fig. 5-5 shows the photoacoustic measurement results using the architecture shown in Fig. 5-4(b), where forward mode was used. Like the results obtained by simulations, the photoacoustic profiles shown in Fig. 5-5(a), differ not only in amplitude, which results from the varied absorption (i.e., varied concentration of graphite), but also in waveforms (i.e., durations). The frequency (magnitude) spectrums and the analysis of the spectrums are shown in Fig. 5-5(b) and (c), respectively. In Fig. 5-5(b), the spectrums of photoacoustic signals with higher absorption have larger peak frequency and broader bandwidth. The peak frequencies, -6 dB, and -20 dB bandwidths versus absorptions are summarized in Fig. 5-5(c). The three parameters increase as the absorption from 1.17 to 3.83 MHz, 2.17 to 7.58 MHz, and 5.58 to 13.17 MHz, respectively.

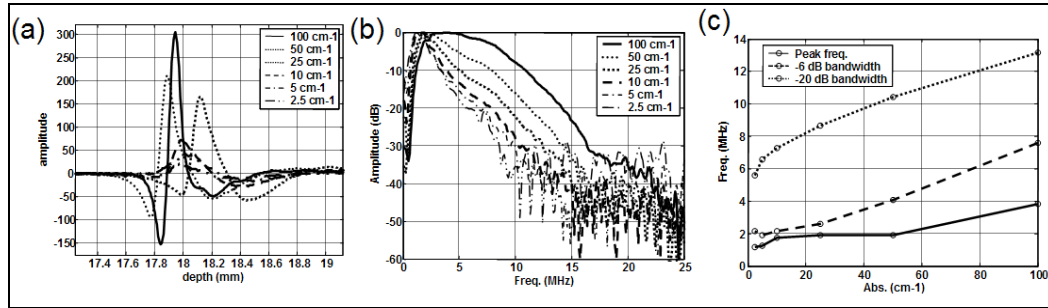


Figure 5-5. The experimental (forward mode) results of phantoms of varied absorption. (a) Photoacoustic signals detected by hydrophone. (b) Frequency spectra of the photoacoustic signals. (c) Peak frequencies, -6 dB, and -20 dB bandwidths vs. absorption coefficients.

The photoacoustic profiles received by backward mode and the analysis in frequency domain are shown in Fig. 5-6. In Fig. 5-6(a), the amplitudes of the profiles increase as the absorption coefficients, but the waveforms do not change as much as those detected by forward mode. The unapparent variation of the waveforms indicates that the frequency spectrums will differ slightly, as shown in Fig. 5-6(b). The relations between peak frequencies, -6 dB and -20 dB bandwidths and the absorption coefficients are summed up in Fig. 5-6(c). The irregularly large -6 dB bandwidth of the 2.5 cm⁻¹ absorber is probably caused by the close spectrums and the interference of noise in analyzing the spectrums. The peak frequencies, -6 dB and -20 dB bandwidths increase from 1.00 to 1.75 MHz, 1.58 (5 cm⁻¹) to 1.83 MHz, and 3.17 to 3.58 MHz, respectively.

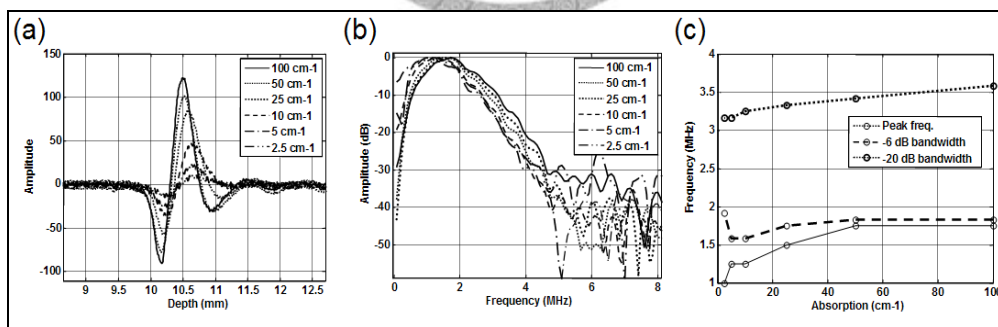


Figure 5-6. The experimental (backward mode) results of phantoms of varied absorption. (a) Photoacoustic signals detected by hydrophone. (b) Frequency spectra of the photoacoustic signals. (c) Peak frequencies, -6 dB, and -20 dB bandwidths vs. absorption coefficients.

5.3 Subband imaging

5.3.1 Phantom experimental results

Fig. 5-7(a) shows the 1-D scanned (forward mode detection) image of two agar phantoms with absorption coefficients of 41.75 cm^{-1} and 5.01 cm^{-1} . Fig. 5-7(b) and (c) illustrate that the magnitude spectrums and the peak frequencies of the each scanned line of the original image, respectively. In Fig. 5-7(b), the spectrum of the phantom with higher absorption extends to about 14 MHz within 10 dB amplitude decay, while the spectrum with lower absorption decreases to below 20 dB at 7 MHz. Fig. 5-7(c) exhibits the up-shift of the peak frequency for phantom with higher absorption from that with lower absorption. The peak frequencies of the 41.75 cm^{-1} phantom are almost larger than 3 MHz, but those of the 5.01 cm^{-1} phantom are lower than 3 MHz, except for those at 30-35 mm in lateral. This discrepancy may be due to the non-uniform concentration of graphite (thus non-uniform absorption) because the phantom was not well mixed during the manufacturing process. To get subband images, three non-overlapping filters, whose magnitude spectrums are shown in Fig. 5-7(d), are designed by using filter design and analysis tool of MATLAB (fdatool). The union of the three bands occupies the whole bandwidth of the receiving hydrophone (i.e., 0-20 MHz).

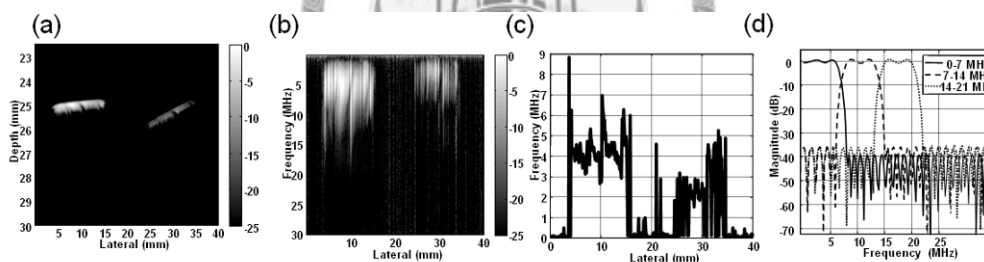


Figure 5-7. (a) Image of agar phantom with absorption coefficients 41.75 cm^{-1} (left) and 5.01 cm^{-1} (right), respectively. (b) Frequency (magnitude) spectrums of the photoacoustic signals of each line. (c) The peak frequencies of each line. (d) Frequency (magnitude) spectrums of three filters for subband images.

The subband images, which are the convolution results of the filters illustrated as Fig. 5-7(d) and the original image (Fig. 5-7(a)) along the depth axis, demonstrate the effectiveness of contrast enhancement. Fig. 5-8(a), (b), and (c) represent the subband images in three pseudo-colors, and Fig. 5-8(d) is the combination of the three subband images. The subband image at band 0-7 MHz (Fig. 5-8(a)) appears like the original image in Fig. 5-7(a), however, those at higher bands (i.e., 7-14 and 14-21 MHz) exhibit greater contrast between the two agarose phantoms. It can be conjectured that the photoacoustic signals of the phantom with lower absorption are suppressed. The

combination image is composed of the three subband images by overlapping them to form a color image. In Fig. 5-8(d), the phantom of 41.75 cm^{-1} appears to be white, which means that the photoacoustic signals have substantial frequency components in all three subbands, whereas the part corresponding to the absorption of 5.01 cm^{-1} is mostly red, which indicates that the frequency components are at band 0-7 MHz in majority.

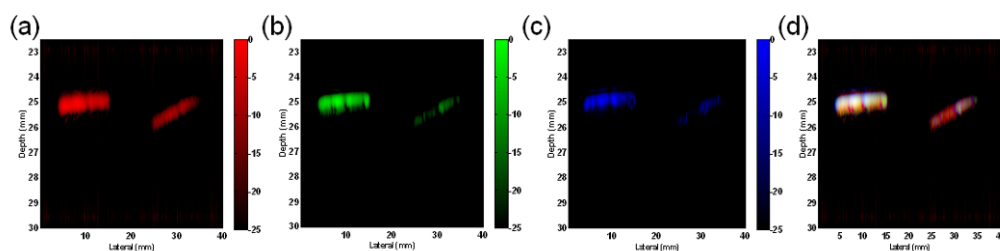


Figure 5-8. Subband images exhibited by using pseudo-colors. (a) Band 0-7 MHz. (b) Band 7-14 MHz. (c) Band 14-21 MHz. (d) Combination image of subband images.

The lateral projections of the three subband images in Fig. 5-9 can further verify the contrast enhancement. In Fig. 5-9(a), the amplitudes of the two absorbers differ about 9 to 15 dB at band 0-7 MHz, while the difference increases to about 13 to 25 dB at band 7-14 MHz (Fig. 5-9(b)). The results mean that at higher frequency band, which is appropriately chosen according to the spectrums, the contrast between absorbers can be effectively improved.

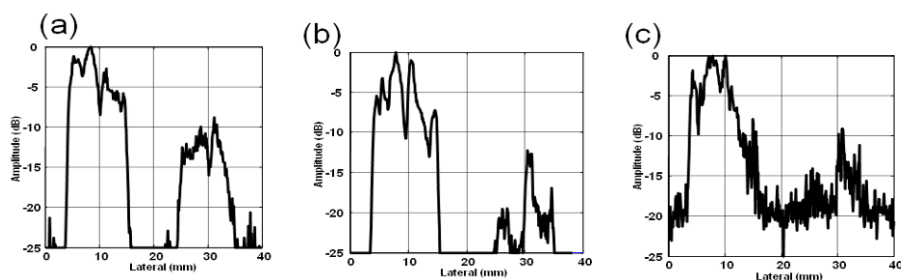


Figure 5-9. Lateral projections of subband images. (a) Band 0-7 MHz. (b) Band 7-14 MHz. (c) Band 14-21 MHz.

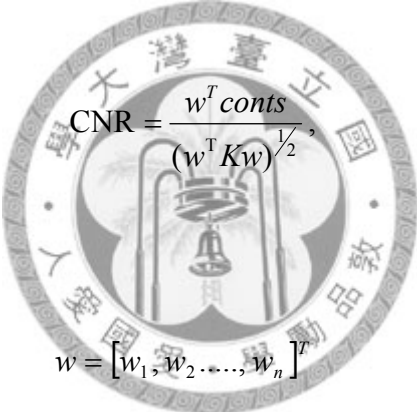
5.3.2 Optimal weighting imaging

Besides choosing the appropriate subbands of the received signals for imaging, the contrast can be improved by summing the subband images with an optimal weighting with information of all frequency bands preserved. The idea had been

proposed in a previous study by P. F. Stetson et al. [83]. Assume that the spectrum of the original image has been separated to N non-overlapping subbands with band-pass filters. The contrast-to-noise ratio (CNR) of two regions to be distinguished in one image is defined as [83]

$$\begin{aligned} \text{CNR} &= \frac{(\text{first region mean}) - (\text{second region mean})}{[\text{first region variance} + \text{second region variance}]^{1/2}} \\ &= \frac{\sum_{k=1}^N w_k \bar{a}_k - \sum_{k=1}^N w_k \bar{b}_k}{\left[\sum_{j=1}^N \sum_{k=1}^N w_j w_k \text{cov}(a_j, a_k) + \sum_{j=1}^N \sum_{k=1}^N w_j w_k \text{cov}(b_j, b_k) \right]^{1/2}} \end{aligned} \quad (5-3)$$

where w_k is the weighing of the k -th subband image, a_k and b_k respectively stand for the first and second region in the k -th subband images, and \bar{x} is the mean value of the region. $\text{cov}(x_j, x_k)$ is the covariance between the j -th and k -th subband images. CNR can be rewritten as



$$\text{CNR} = \frac{w^T \text{conts}}{(w^T K w)^{1/2}}, \quad (5-4)$$

where

$$w = [w_1, w_2, \dots, w_n]^T \quad (5-5)$$

is the weighting vector of the subband images, and

$$\text{conts} = [\bar{a}_1 - \bar{b}_1, \dots, \bar{a}_n - \bar{b}_n]^T \quad (5-6)$$

is the contrast vector. K is the sum of the covariance matrices of the two regions. By taking the first differentiate of CNR with respect to w , the values of w to make CNR have an extreme can be obtained. The result can be solved as

$$w = \alpha K^{-1} c, \quad (5-7)$$

where K^{-1} is the inverse matrix of K and α is the scaling factor. The diagram of the weighing and summation is shown in Fig. 5-10 [83].

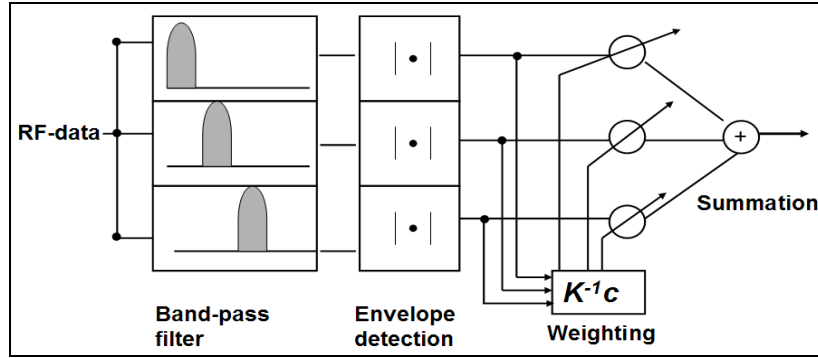


Figure 5-10. The optimal contrast weighting summation process.

Fig. 5-11 shows the summed images of the three subband images shown in Fig. 5-8(a)-(c) and the lateral projections with two types of weighting, equal weighting and optimal weighting. The summed image with equal weighting (Fig. 5-11(a)) is equivalent to the intensity of the color image shown in Fig. 5-8(d). With the optimal weighting derived in equation (5-7) with the scaling factor α equaling to 1, the contrast between the two absorbers is further enhanced. In Fig. 5-11(c), the lateral projections exhibit that the contrast of equal weighting image has less enhancements to the original image, while the contrast enhancement of the image with optimal weighting is evident, thus demonstrating the feasibility of the described method with the entire frequency bandwidth of the received signals preserved.

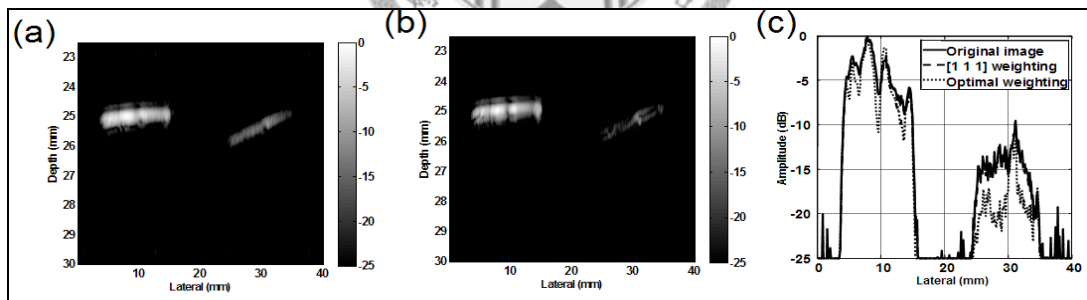


Figure 5-11. (a) Summed image with equal weighting. (b) Summed image with optimal weighting. (c) Lateral projections of the original image, equal weighting image, and optimal weighting image, respectively.

5.4 Discussion

5.4.1 Signal frequency at backward and forward detection

Comparing the results between the two detection modes, the increments of peak frequencies, -6 dB and -20 dB bandwidths with the increasing absorptions are all smaller by backward detection than those by forward detection. The small frequency variation by backward detection may be due to the included angle between the hydrophone and the optical fiber. To verify the influences of the detection directivity, a study compares the photoacoustic signals detected by forward mode, backward mode, and sideward mode (i.e., the detection is perpendicular to the optical irradiation) by using numerical simulations. Fig. 5-12 shows the summary of the peak frequencies of the photoacoustic waveforms obtained by the two detection modes, forward mode and backward mode. In the experimental setup of backward detection, the hydrophone-fiber angle is about 30~45 degrees, which form a detection mode between backward and sideward mode instead of backward mode. The geometry of the experimental setup for forward detection limits the practical applications in biomedical imaging. Thus, the setup for backward detection will be adopted for more applications in the future.

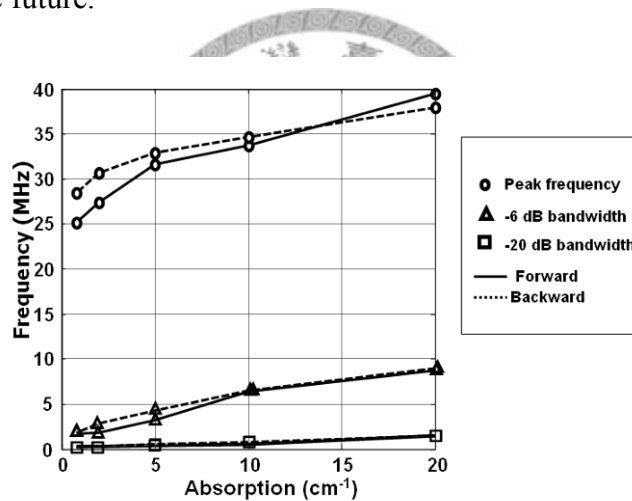


Figure 5-12. Peak frequencies vs. various absorptions by forward mode and backward mode, respectively.

5.4.2 More precise methods for frequency component extraction

In Fourier transform analysis, using a larger window of signal for frequency spectrum calculation gives a better frequency resolution, which is beneficial for obtaining frequency parameters (i.e., peak frequency and bandwidth). However, a large window means a poor spatial resolution. Wavelet transform and Hilbert Huang transform (HHT) provide local frequency analysis without degrading the spatial resolution. The following works will focus on using these two methods for frequency

analysis in simulations. Also, experimental data acquired with a home-made broadband photoacoustic transducer will be used to demonstrate the feasibility of contrast enhancement using subband imaging and reconstruction of absorption coefficients. Fig. 5-13 shows an example of a simulated case of frequency analysis using Wavelet and HHT methods. The original absorption coefficient distribution and the simulated photoacoustic signals received by an infinite-band transducer are shown in Fig. 5-13(a) and (b), respectively. The averaged frequency (the first moment of the spectrum) calculated from the spectra analyzed from Wavelet method and HHT method are illustrated in Fig. 5-13(c) and (d), respectively. The structure of the original absorption map can be clearly seen in the images of averaged frequency calculation. However, there is unknown distortion which needs to be corrected.

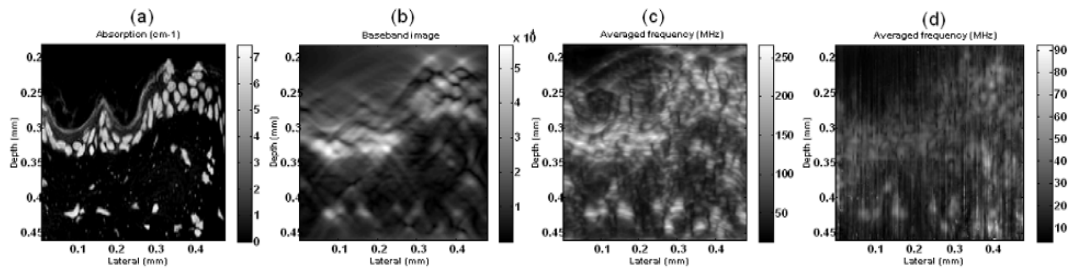


Figure 5-13. Simulation results for frequency analysis. (a) Absorption coefficient distribution. (b) Received photoacoustic image. (c) Averaged frequency by Wavelet analysis. (d) Averaged frequency by HHT analysis.

Besides taking subbands for imaging, the contrast of the photoacoustic image can be also enhanced by multiplying the received photoacoustic image (Fig. 5-13(b)) by the averaged frequency image (Fig. 5-13(d)), which means adding weighting on the original photoacoustic image. The multiplying image shown in Fig. 5-14 shows that the artifacts due to focusing errors in Fig. 5-13(b) are successfully reduced and the amplitude distribution is more like the original absorption map in Fig. 5-13(a).

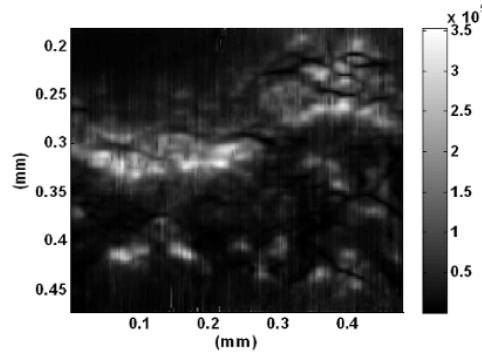


Figure 5-14. Multiplying image of subband image and averaged frequency image.

5.4.3 Geometry dependent frequency

From the simulation and experimental results, the frequency information (i.e., peak frequency and bandwidth) of the photoacoustic signal of an object with fixed absorption will differ due to the variation of architecture (e.g., laser irradiated pattern, detection location and distance, etc). It is difficult to reconstruct the absorption coefficient based on the frequency spectrum at this stage. Nevertheless, the relative relation of frequency spectrum of objects with various absorptions is apparent if the photoacoustic signals are detected by the same setup of detection. It may be feasible to reconstruct absorption coefficients relatively. An absorber with known absorption coefficient and geometry will be set as a reference placed above the region of interest. The comparison between the received photoacoustic signals from the absorber will help to find out the relation between frequency component and geometry. Fig. 5-15 shows a simulation result of three absorbers with different absorption coefficients: 10 cm^{-1} , 5 cm^{-1} , and 2 cm^{-1} , with the absorption map shown in Fig. 5-15(a). The averaged frequency distribution analyzed by HHT (Fig. 5-15(b) and (c)) shows the relation between the frequency component and the absorption of the absorbers, indicating the frequency increases as the absorption. The relation between the thickness of the absorbers and the signal frequency is also simulated (Fig. 5-16). The absorbers were set to be 5 cm^{-1} in absorption and the thicknesses were different (from 0.5 mm to 6 mm). The averaged frequency of the received photoacoustic signal is plotted as a function of thickness in Fig. 5-16(b), which indicates the frequency is higher when the absorber has a smaller thickness. More simulations about other factors which will alter the signal frequency spectrum will be performed. The factors include optical illumination, laser pulse duration, and detection location. With the simulation results,

the absorption coefficient of an objective absorber can be obtained by comparing the frequency component with that of a reference absorber with known absorption coefficient and geometry. These methods need to be further demonstrated by analyzing more realistic simulation cases and experimental data.

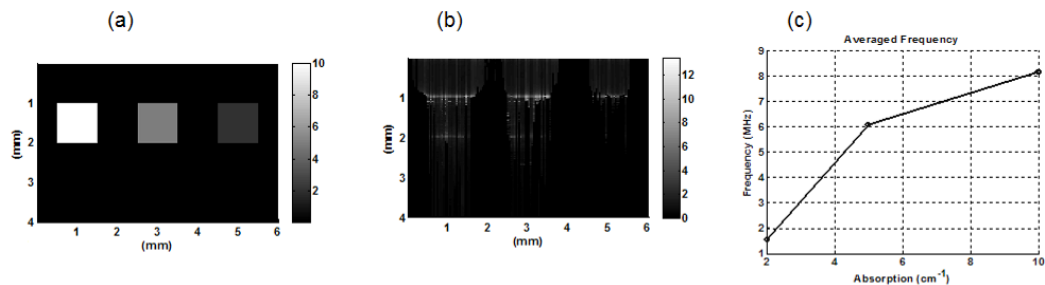


Figure 5-15. Simulation results of absorbers with different optical absorptions. (a) Absorption coefficient distribution. (b) Averaged frequency by HHT analysis. (c) Averaged frequency vs. Absorption coefficient.

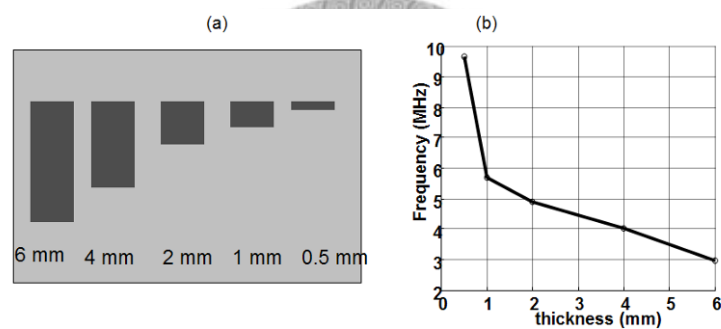


Figure 5-16. Simulation results of absorbers with different thickness. (a) Absorption coefficient distribution. (b) Averaged frequency vs. thickness.

5.5 Concluding remarks

It has been demonstrated that the subband photoacoustic imaging method enhances the contrast between objects with different absorption coefficients. This method was demonstrated by simulations and experiments. The simulation, which is based on the Beer-Lambert law, verified the appearance of frequency variation due to the disparity of absorption coefficients. The experiments were performed by using agar phantom with various concentrations of graphite to create optical absorptions with more than tens times difference. For absorbers with absorption coefficients from 2.5 cm^{-1} to 100 cm^{-1} , the peak frequencies and the -6 dB bandwidths of the PA signals

increase from 1.17 to 3.83 MHz and from 2.17 to 7.58 MHz, respectively. Imaging an agar-based phantom further demonstrated that the contrast between two objects with absorption coefficients of 5.01 and 41.75 cm^{-1} can be improved by up to 10 dB when the frequency band was changed from 0–7 to 7–14 MHz. The subband images can be displayed with different pseudo-colors to reveal signals from different frequency bands (i.e., different optical absorption). Also, an optimal weighting scheme was applied to weight and integrate subband images to obtain a more improvement of image contrast. The contrast can be further improved by using optimal weighting. The proposed method will be applied to *in vivo* mouse imaging using gold nanoparticles as the contrast agent. Region with a high concentration of gold nanoparticles is likely to exhibit high optical absorption, and hence applying the subband imaging method is expected to improve the quality of molecular imaging.



CHAPTER 6 DISCUSSION

6.1 Laser safety regulation

The maximum permissible exposure (MPE) of laser irradiation on humans is regulated in The American National Standard Z136.1[84]. MPE is defined as the maximum energy/power level that will not cause any damage to the surface skin or tissues of humans. It correlates with the optical wavelength, pulse duration, and pulse repetition rate. For CW laser, three different ranges of optical wavelength from visible to near infrared are discussed. From 400 nm to 700 nm, the MPE is 0.2 W/cm². For wavelength from 1050 nm to 1400 nm, the MPE increases to 1 W/cm². The MPE within the middle range (700 nm~ 1050 nm) is

$$0.2 \times Ca \text{ W/cm}^2, \quad (6-1)$$

where Ca is wavelength dependent parameter given by

$$Ca = 10^{2\left(\frac{\lambda(\text{nm})-700}{1000}\right)}, \quad 700 \text{ nm} < \lambda < 1050 \text{ nm}. \quad (6-2)$$

At wavelength used in this thesis for thermal therapy (i.e., 800 nm) described in Chapter 4, the MPE is 0.32 W/cm². For subcutaneous injection of gold nanorods into tumor in section 4.3.1, the CW laser power was 0.76 W/cm², which exceeds the MPE. This experiment was for demonstration of the efficacy of the photoacoustic system in obtaining temperature changes during thermal therapy, and there was no any damage or change observed in the tumor, which may be due to the lack of melanin on the mice skin. For real targeted imaging and therapy experiment in section 4.3.2, the power of CW laser was within the MPE at 800 nm.

The MPE for PW laser at several wavelengths used in this thesis are listed as follows. For laser pulse with duration of 10 ns, the MPE is 20 mJ/cm² at 400 nm to 700 nm, 100 mJ/cm² at 700 nm to 1050 nm, and 20×Ca mJ/cm², where Ca is defined in equation (6-2). For wash-out flow velocity measurement in section 2.4, the energy at 532 nm was 35 mJ/cm², which was larger than the MPE. For all other experiments for flow estimation and cell targeting, the energy levels of the PW laser for photoacoustic generation were well below the MPEs, which were 31.7 mJ/cm² at 800

nm, 100 mJ/cm² at 1064 nm.

6.2 Biocompatibility of gold nanoparticles

Biocompatibility testing of gold nanoparticles is necessary for photoacoustic *in vivo* studies. Although there is no safety regulation of gold nanoparticles to date, ISO 10993 provides guidance for biological evaluation of gold nanoparticles in biomedical applications. The results shown in this section were accomplished by Dr. D.-B. Shieh's lab in National Cheng Kung University.

The toxicity of the gold nanorods had been tested *in vitro*. Vero cells, which were derived from African green monkey kidney, were used as the model cell lines for cytotoxic assay. Subconfluence (~80%) Vero cells were treated with anti-HER2 or anti-CXCR4 antibody conjugated gold nanorods in 0.6, 0.3, and 0.15 nM for 4 hours. The cell viability was then measured by WST-1 assay (Takara), which stood for cell number and activity. Fig. 6-1 shows the relation between cell viability (normalized to the number of control sample) and the concentration of bioconjugated gold nanorods. The cell viability of all test samples remained almost the same as the control sample, indicating that the toxicity was low within the concentration range of particles. The concentration of gold nanorods used in this study is below 0.2 nM (estimated by multiplying the cell concentration to N_{Au} described before), which is within the range for toxicity test, and therefore it is safe to use gold nanorods in biological issues.

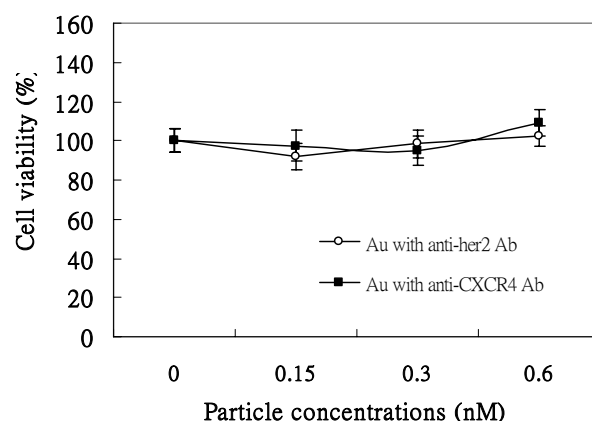


Figure 6-1. The relation between cell viability (normalized to the control) and the concentration of bioconjugated gold nanorods. The results were from Dr. D.-B. Shieh's lab in National Cheng Kung University.

The *in vitro* biosafety analysis of AuNRs including cellular toxicity test and hemocompatibility analysis have been accomplished. The results show that AuNRs are biocompatible and hemocompatible for *in vivo* tests (Fig. 6-2, Fig. 6-3, and Fig. 6-4). In the dosages aiming to be applied for future *in vivo* applications, the nanoparticles presented satisfactory biosafety for *in vivo* evaluation.

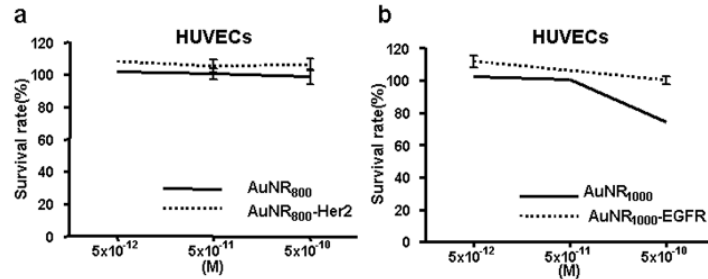


Figure 6-2. *In vitro* biosafety analysis of the Au nanorods. The analysis was performed using MTT assay in Human Umbilical Vein Endothelial Cell (HUVEC) line. (a) Cells reacted with AuNR₈₀₀ and AuNR₈₀₀-antiHER2. (b) Cells reacted with AuNR₁₀₀₀ and AuNR₁₀₀₀-antiEGFR. The results were from Dr. D.-B. Shieh's lab in National Cheng Kung University.

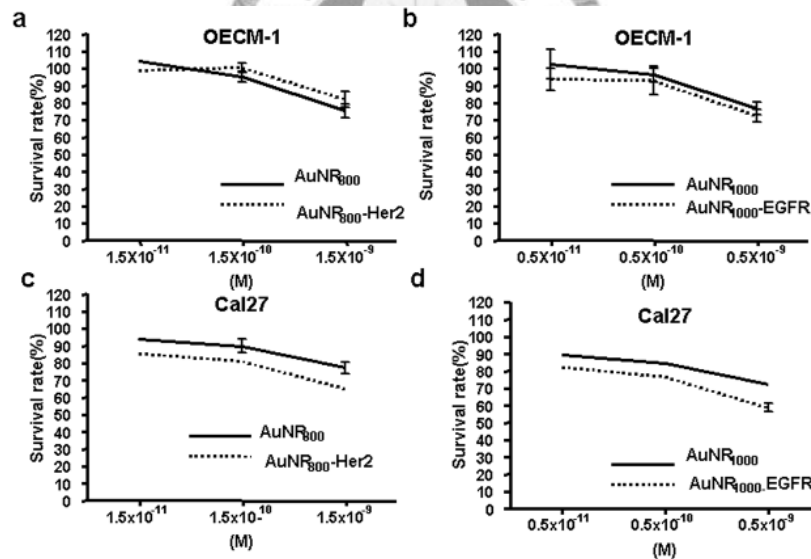


Figure 6-3. *In vitro* biosafety analysis of the Au nanorods. The analysis was performed using MTT assay in OECM1 and Cal27 cell lines with a number of 5,000 cells. The test time was 24 hours (a) OECM1 cells reacted with AuNR₈₀₀ and AuNR₈₀₀-antiHER2. (b) OECM1 cells reacted with AuNR₁₀₀₀ and AuNR₁₀₀₀-antiEGFR. (c) Cal27 cells reacted with AuNR₈₀₀ and AuNR₈₀₀-antiHER2. (d) Cal27 cells reacted with AuNR₁₀₀₀ and AuNR₁₀₀₀-antiEGFR. The results were from Dr. D.-B. Shieh's lab in National Cheng Kung University.

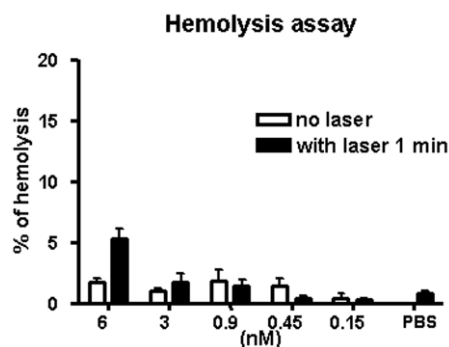


Figure 6-4. Hemolysis assay results. Human blood was mixed with AuNR₈₀₀ of different concentration. The experimental groups were irradiated by laser pulses at 800 nm with an energy density of 40 mJ/cm² per pulse. The irradiation time was 1 minute (about 600 pulses). Three samples were performed for each case to obtain the average and standard deviation. The results were from Dr. D.-B. Shieh's lab in National Cheng Kung University.

The *in vivo* toxicity test for AuNRs in BALB/c mice through tail-vein injection has also been performed. A satisfactory experimental result was obtained as the mice all survived the two-month observation period (Fig. 6-5).

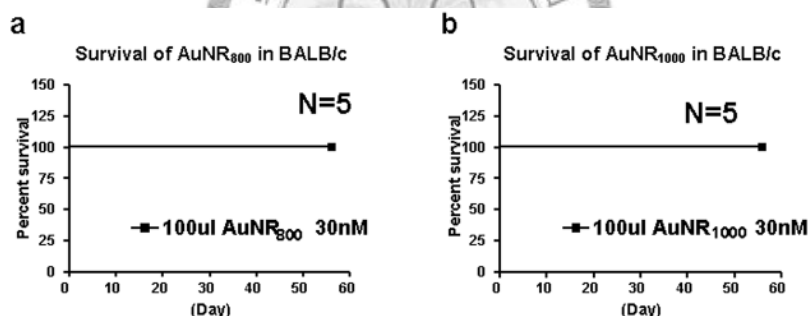


Figure 6-5. *In vivo* systemic toxicity analysis revealed that all test animals survived the two months evaluation period of time. (a) Mice injected with AuNR₈₀₀. (b) Mice injected with AuNR₁₀₀₀. The results were from Dr. D.-B. Shieh's lab in National Cheng Kung University.

In addition, analyzing the biodistribution of AuNRs in BALB/c mice in a time course to realize the metabolic clearance of the AuNRs has also been developed. A primary evaluation result of metabolic uptake and clearance of the nanoparticles indicates that these nanoparticles were mainly uptake by the liver and the accumulated in the spleen and liver that reached a plateau at 24 hours then gradually reduced through time (Fig. 6-6). The nanorod concentrations returned to background level at 168 hours after intravenous injection.

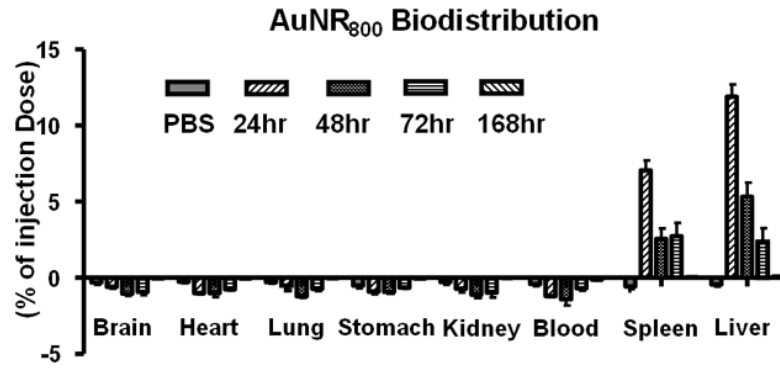


Figure 6-6. Atomic absorption spectroscopy analysis of organs taken from test mice at different time period after intravenous injection. The result revealed that these nanorods were mainly accumulated in the spleen and liver and could be cleared after 168 hours. The results were accomplished by Dr. D.-B. Shieh's lab in National Cheng Kung University.



CHAPTER 7 CONCLUSIONS AND FUTURE WORKS

7.1 Conclusions

In this thesis, gold nanoparticles based functional and molecular photoacoustic imaging techniques have been developed for quantitative flow estimation and targeted cancer diagnosis and treatment, respectively. Also, a subband imaging method has been used to enhance the contrast between region of interest (with contrast agent) and background surrounding tissues.

For flow estimation, both wash-out and wash-in analyses were performed. In wash-out results, the correlation coefficients between the theoretical values and flow related parameter (i.e., MTT and τ) are all above 0.97, indicating the feasibility of relative measurement. Wash-in analysis, which avoids the limitation of assuming bolus injection in wash-out methods, has a better potential for *in vivo* studies. Destruction-replenishment method using shape-transition of gold nanorods has been developed for both two-energy and single-energy methods. By using the single-energy method, fixed laser energy is employed, no need to use two different laser energies. The correlation coefficients between actual flow velocities and the measured flow velocities are all above 0.96, thus demonstrating the feasibility of photoacoustic flow estimation with wash-in analysis using gold nanorods. Future work will focus on *in vivo* perfusion measurement on tumor angiogenesis using the wash-in methods for monitoring the development of tumor.

Photoacoustic molecular imaging with simultaneous multiple selective targeting has been demonstrated by using bioconjugated gold nanorods on oral cancer cells and angiogenesis *in vitro* and *in vivo*. Two different oral cancer cells, each with a specific cell-antibody pair (OECM1 to antiHER2 probe and Cal27 to antiEGFR probe), were adopted to demonstrate the multiple targeting relations. The results show that both cancer cells exhibit a higher photoacoustic response (maximum 3.5 dB) than control groups with specific targeting. Multiple targeting on oral cancer cell line with two specific targets was also performed, revealing further enhancement of targeting (4 dB) of OECM1 with mixed antiHER2 and antiCXCR4 probes. Angiogenesis targeting was

achieved with peptide RGD4C-conjugated gold nanorods. At last, simultaneous targeting by using mixed antiHER2 and RGD4C probes on OECM1 tumor was performed, showing that the probe injected tumor exhibits higher photoacoustic signal than pure gold nanorod injected tumor at two wavelengths corresponding to the peak absorption of probes/nanorods. The results reveal that the information from oncogene surface molecules of cancer cell can be probed with photoacoustic techniques, which help to understand the characteristics of cancer cells better and provide an effective diagnosis tool as well as indication for efficacious treatment.

Targeted thermal therapy system was integrated with the photoacoustic imaging system to perform treatment of the tumor by irradiating the targeted gold nanorods on tumor with continuous wave laser. The temperature could rise to above 42 °C to reach the hyperthermia condition of tumor region with the existence of targeted gold nanorods. The pathological results of the taken out tumors after imaging exhibit tumor necrosis but no damage found in normal cells, including fibroblast cells and peripheral follicles. Also, quantitative thermal imaging based on the photoacoustic signal amplitude was achieved to observe the temperature changes for safety and efficacy concerns. The thermal images reveal that the temperature distribution within the tumor during thermal therapy (CW laser on) is generally higher than that after therapy (CW laser off), indicating the efficacy of real-time monitoring of temperature by photoacoustic technique during thermal therapy.

A subband imaging method has been developed to enhance the contrast between different absorbers by simulations and experiments. The simulation, which is based on the Beer-Lambert law, verified the appearance of frequency variation due to the disparity of absorption coefficients. The experiments were performed by using agar phantom with various concentrations of graphite to create optical absorptions. The peak frequencies and the -6 dB bandwidths of the photoacoustic signals increase from 1.17 to 3.83 MHz and from 2.17 to 7.58 MHz for absorption coefficients from 2.5 cm⁻¹ to 100 cm⁻¹, respectively. The subband image at band 7-14 MHz shows maximum 25 dB intensity difference between two agars with respective absorption of 41.75 cm⁻¹ and 5.01 cm⁻¹, while the maximum difference is 15 dB at band 0-7 MHz, indicating a 10 dB contrast enhancement.

7.2 Future work: *in vivo* perfusion measurements

Angiogenesis, blood supply developed violently at early stage of tumor, is a

critical indicator to the growth of cancers [85]. Therefore, detecting and monitoring the angiogenesis will help diagnose and trace the tumors. In Chapter 2, destruction mode (i.e., wash-in) time-intensity based flow estimation techniques have been developed. For tumor observation, these techniques provide useful tools for imaging the angiogenesis. The concentration of gold nanorods recorded in this study was from a time sequence of photoacoustic intensities and can be used for flow measurements. In practice, nonetheless, TIC measurements from a single region of interest may not be ideal. For *in vivo* applications, the TIC can also be measured using a sequence of two-dimensional (2D) images. In this case, a region of interest is identified and the average intensity within the region of interest is used as a data point in the TIC. The regions with perfusion can be determined by subtracting the image before gold nanorods injection from the image after the injection.

For 2D imaging, a high frame rate photoacoustic imaging system needs be constructed using an array transducer instead of a single-element transducer and a high firing rate laser system. With an array, photoacoustic data can be acquired simultaneously from multiple channels and mechanical scanning can be avoided. With such a system, image-based TIC measurements are feasible to capture the rapid flow change of angiogenesis in small animal model.

The measurement process will be as follows. Tumor induced on the back of mice after 10 to 15 days of growth is to be monitored. Gold nanorods are injected through the lateral tail vein, and the image scanning is commenced at several minutes after injection in order to achieve a constant concentration of gold nanorods by blood circulation. Then, a series of laser pulses are delivered for nanorod transformation and photoacoustic generation, and two energy levels are applied if two-energy method is used, while one energy level if single-energy method is used. The photoacoustic signals are then stored for subsequent analyses. Then the averaged flow velocities of each perfusion regions can be derived from the temporal photoacoustic images.

The calculated flow velocities v can be used to quantify the tumor angiogenesis. The flow rate Q is an important parameter for evaluate the growth of tumor and can be obtained by

$$Q = v \times A_{perfusion}, \quad (7-1)$$

where $A_{perfusion}$ is the area of the perfusion region, which can be determined by the angiogenesis targeting with peptide conjugated nanorods described in section 3.4.2.

Besides, vascularity index (VI) is used for quantifying tumor angiogenesis in color Doppler ultrasound system [86]. VI is defined as the ratio of the number of the colored pixels (with flow detected) within the defined tumor section over the number of pixels in the same section and is a good preoperative indicator of tumor metastasis. VI can be also evaluated as the ration of the area of the perfusion region over the total area of the predetermined tumor region A_{total} . That is,

$$VI = \frac{A_{perfusion}}{A_{total}} \quad (7-2)$$

7.3 Future work: subband imaging for *in vivo* studies

In the future, the proposed subband imaging methods will be applied on *in vivo* investigations, including perfusion estimation using gold nanoparticles as dilution indicators and molecular imaging with targeted gold nanoparticles on tumor. The injected gold nanoparticles within blood vessels or the targeted gold nanoparticles on tumor results in a higher absorptions, which means higher frequency components comparing to those of surrounding tissues. Thus, applying the subband method assists in increasing the detection sensitivity of recognizing the blood vessel in tumor region.

A wideband photoacoustic transducer will be needed to capture the signals with widespread frequency bands from various absorbers. In Chapter 5, a wideband hydrophone was used for signal detection. However, a hydrophone is not able to produce pulse/echo image for obtaining scattering properties of the observed region. Therefore, a photoacoustic transducer that can transmit/receive ultrasonic waves for ultrasonic imaging and detect wideband photoacoustic signals is needed. Table 7-1 lists several physical properties of common piezoelectric materials. The polyvinylidene fluoride (PVDF) membrane is a typical piezoelectric polymer material with low acoustic impedance Z similar to that of human tissues and a low dielectric constant ϵ , which is suitable for electrical impedance matching. It can be easily pressed into a curve-shaped geometry that makes excellent focusing. Moreover, the low quality factor Q_m makes PVDF a suitable material for broadband transducer. Thus, PVDF is a good candidate for fabricating wideband photoacoustic transducer. A single crystal transducer will be first fabricated for initial test of the performance of the transducer of PVDF. Fabricating an array transducer will be the ultimate goal for achieving high frame rate broadband photoacoustic imaging.

Table 7-1. The properties of piezoelectric materials.

Material	K_t	ϵ	ρ (g/cm ³)	c_s (m/s)	Q_m	Z (Mrayl)
PVDF	0.13	6.5	1.8	2150	12	3.87
PZT-5H	0.50	1470	7.5	4560	9.2	34.2
1-3 PZT	0.6	200	3.3	3943	9.2	13
LiNbO ₃	0.49	50	4.64	7340	10000	34

With the transducer, the wideband photoacoustic signals corresponding to absorbers with different optical absorption can be all collected without being truncated. Taking target as an example, the signal acquisition process will be as follows. The tumor induced on a small animal model will be observed. Gold nanorods will be injected into the mouse through the tail vein. At a certain time a sufficient number of gold nanorods targeted on tumor, both ultrasonic and photoacoustic images will be acquired subsequently. From the results in Chapter 3, the intensity increasing with targeted gold nanorods of tumor is up to about 4 dB. With subband imaging, the increase of intensity is expected to be more than 6 dB, which provides a more distinguishable contrast between the tumor and surrounding tissue. The recorded photoacoustic images will be divided into several subband images by convoluting with bandpass filters. The center frequency and passband of the filters will be designed according to the received images. For example, one of the filters can be designed to match the spectrum of the photoacoustic signals from tumor region with targeted gold nanorods. Therefore, choosing this subband for imaging can enhance the signals from gold nanorods and increase the contrast in addition to the difference in optical absorption. Alternatively, the subband images can be integrated with optimal weighting according to section 5.3.2 to obtain images with enhanced contrast.

7.4 Future Work: new nanoparticles for sensitivity improvement

Design and synthesis of gold nanoparticles for enhanced photoacoustic response is beneficial for biomedical imaging with the assist of using gold nanoparticles as contrast agents. For example, gold nanorods have been used as the tracer in time-intensity based flow estimation methods. Gold nanorods have also been used as nanoprobles with targeting ability to cancer cells for diagnosis at the early stage [87]

and effective treatment.

New particles for further enhancing photoacoustic response were designed from Prof. C.-R.-C. Wang's group in National Chung Cheng University and tested using photoacoustic techniques. The key idea of fabricating new particles is to let the particles to transmit heat anisotropically. The heat flux is designed to release outwards from the end(s) of the particle and therefore provide a greater temperature gradient, which generates enhanced photoacoustic signals. To achieve this, a layer of SiO₂ is coated along the longer axis of the gold nanorods, but not covered both ends. These new particles are labeled as AuNR@SiO₂. Since the laser irradiation on AuNRs is to excite the free electron cloud into a collective dipolar oscillation mode, a unique anisotropic growth chemical method along with surface assisted deposition was developed by Prof. C.-R.-C. Wang's group to attach metal spheres such as Au or Ag on the end of AuNR@SiO₂, which is like nanodumbbell. The designed synthetic scheme is as Fig. 7-1.

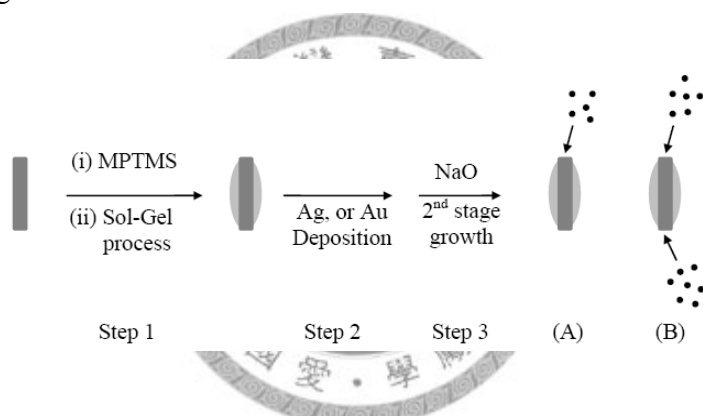


Figure 7-1. Schematic diagram representing the asymmetric synthesis of AuNR@SiO₂ or nanodumbbells gold/silver nanoparticles. This synthesis process was from Prof. C.-R.-C. Wang's lab in National Chung Cheng University.

Fig. 7-2 shows the diagram of original AuNR with coated PEG and new synthesized particles, including AuNR@SiO₂ and nanodumbbells, and their TEM images are shown in Fig. 7-3.

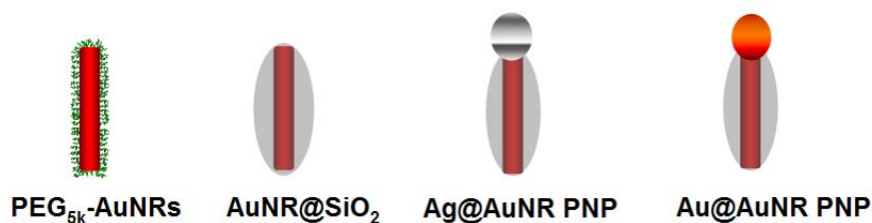


Figure 7-2. Diagrams of different AuNR samples.

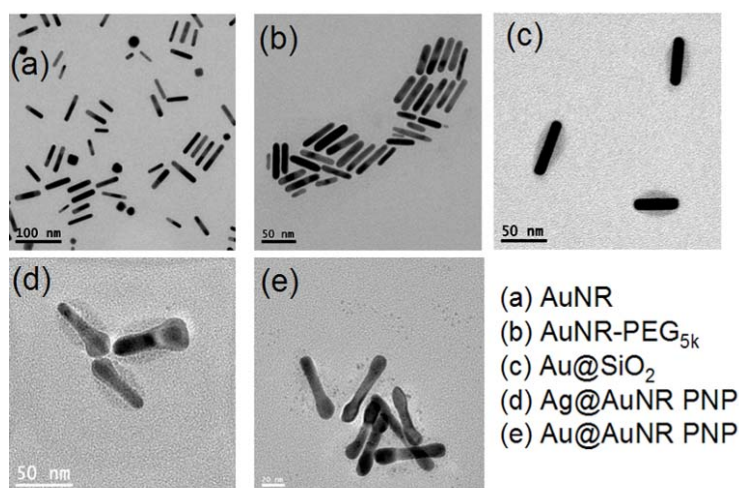


Figure 7-3. TEM images of new AuNR particles. The images were from Prof. C.-R.-C. Wang's lab in National Chung Cheng University.

The synthesized new particles, including Ag@AuNR PNP, Au@AuNR PNP, and AuNR@ SiO₂, were measured with the photoacoustic method. The obtained images were compared with those of AuNR-PEG in PBS solution and deionized water. The diagram of experimental setup is shown in Fig. 7-4. The samples and a small amount of cotton were placed into a transparent plastic tube with an inner diameter of 3 mm. The use of cotton was to simulate randomized distribution of samples in real tissues. The optical illumination was delivered by a Ti: Sapphire laser (CF-125, SOLAR TII) pumped by an Nd: YAG laser (LS-2137, LOTIS TII). The irradiating laser has a wavelength of 900 nm corresponding to the peak absorption wavelength of test samples. The pulse repetition rate was 10 Hz and the laser energy density was 21.22 mJ/cm². A home-made photoacoustic transducer with a center frequency of 20 MHz and focus depth of 10 mm was used for signal receiving. A hole was drilled in the center of the transducer to be inserted an optical fiber for photoacoustic signal generation. The combined photoacoustic probe was driven by a precision stage to perform 1D scanning. Each sample was measured three times.

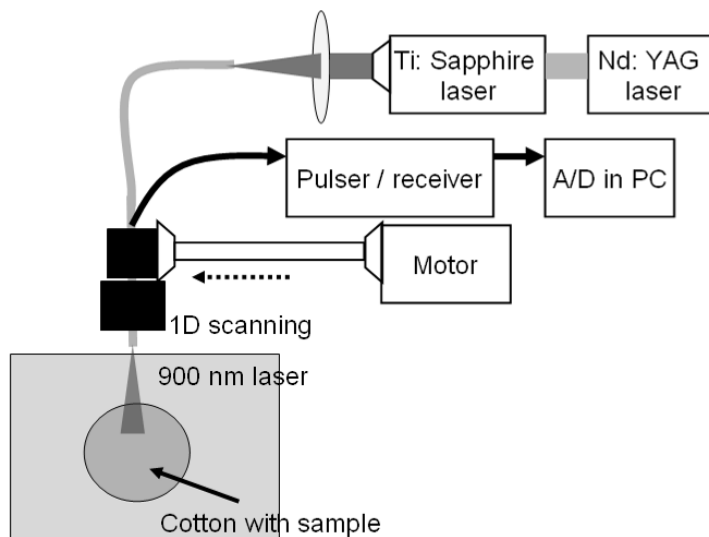


Figure 7-4. Photoacoustic experimental setup for testing new particles.

Fig. 7-5 shows the photoacoustic images of 5 different samples of three measurements: deionized water, AuNR-PEG in PBS solution, Ag@AuNR PNP, Au@AuNR PNP, and AuNR@SiO₂ (top to bottom). The energy decay of the incident laser energy due to optical absorption of sample can be clearly seen in each image. For the images of reference sample, deionized water, only a slice of arc region of signal can be observed. For AuNR-PEG, a little more high intensity region can be seen. The images of the three new particles, Ag@AuNR PNP, Au@AuNR PNP, and AuNR@SiO₂, reveal obvious stronger intensity within the tube region. The mean intensity and the error bars showing the standard deviations of the three measurements are shown in Fig. 7-6, which the maximum increase of intensity is about 5 dB between AuNR-PEG and AuNR@SiO₂.

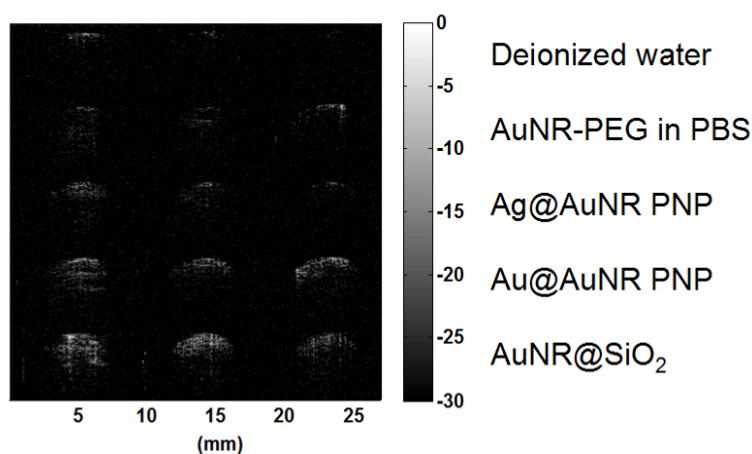


Figure 7-5. Photoacoustic images of different samples. Up to bottom: water, AuNR-PEG in

PBS, Ag@AuNR PNP, Au@AuNR PNP, and AuNR@SiO₂.

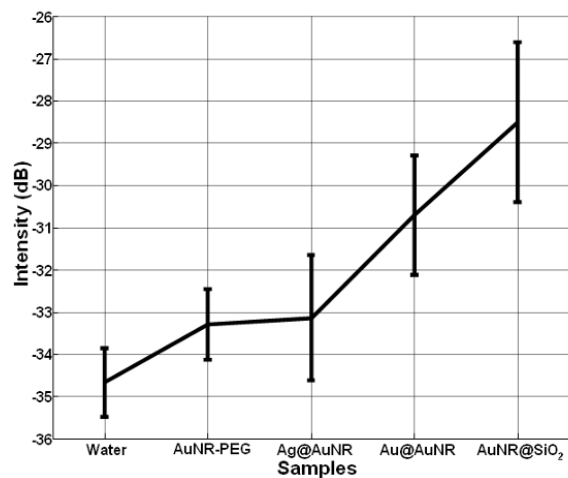


Figure 7-6. Photoacoustic intensity within the tube of different samples.

The shape transition property of new particles was also tested. AuNR-PEG and one of the new particles, AuNR@SiO₂, were measured to record the photoacoustic responses versus time after high laser energy irradiation. The laser energy density was 42.44 mJ/cm², which can induce shape transition of AuNR [29]. The irradiation time was 50 seconds, 500 pulses. Fig. 7-7 shows two time-intensity curves of AuNR and AuNR@SiO₂, respectively. The intensity was normalized to its maximum, showing the intensity of AuNR decreases to below 0.6 after about 10 seconds of irradiation, while the intensity is mostly larger than 0.7 for AuNR@SiO₂. The results indicate that the new particles own higher resistance to shape transition under pulse laser irradiation and thus higher shape stability due to the confinement of SiO₂ coating. In other words, AuNR@SiO₂ can preserve their higher photoacoustic responses under laser irradiation compared to traditional AuNR.

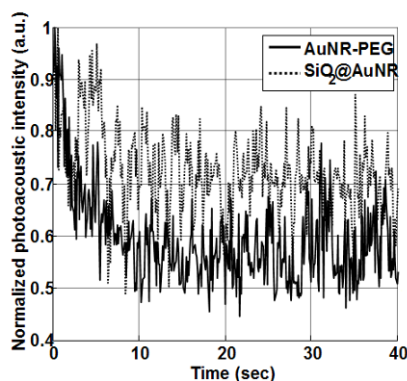
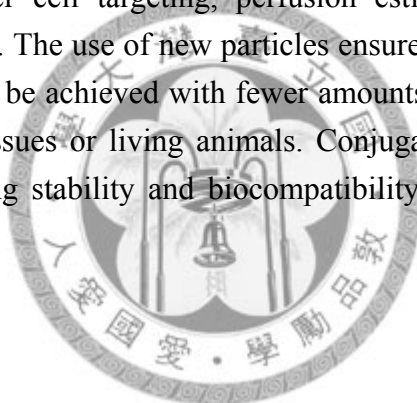


Figure 7-7. Normalized photoacoustic intensity of AuNR-PEG and AuNR@SiO₂ vs. time.

The measurement results demonstrate the promise of using new particles to enhance the photoacoustic response. These new particles can improve the detection sensitivity of photoacoustic images and assist *in vivo* studies involved with cancer research, including cancer cell targeting, perfusion estimation, and nanoparticles based thermal therapy, etc. The use of new particles ensures that the goal of diagnosis and therapy of cancer can be achieved with fewer amounts of particles, which means less toxicity to normal tissues or living animals. Conjugating biomolecules on new particles and the following stability and biocompatibility tests are necessary for *in vivo* studies in the future.



References

- [1] E. Gusev and A. A. Karabutov, *Laser Optoacoustics*, 1993.
- [2] R. O. Esenaliev, A. A. Karabutov, and A. A. Oraevsky, "Sensitivity of laser opto-acoustic imaging in detection of small deeply embedded tumors," *IEEE Journal of Selected Topics in Quantum Electronics*, vol. 5, pp. 981-988, Jul-Aug 1999.
- [3] A. A. Karabutov, N. B. Podymova, and V. S. Letokhov, "Time-resolved laser optoacoustic tomography of inhomogeneous media," *Applied Physics B-Lasers and Optics*, vol. 63, pp. 545-563, Dec 1996.
- [4] J. A. Viator, L. O. Svaasand, G. Aguilar, B. Choi, and J. S. Nelson, "Photoacoustic measurement of epidermal melanin," in *BiOS, Proc. SPIE*, San Jose, 2003, pp. 14-20.
- [5] H. F. Zhang, K. Maslov, G. Stoica, and L. H. V. Wang, "Functional photoacoustic microscopy for high-resolution and noninvasive in vivo imaging," *Nature Biotechnology*, vol. 24, pp. 848-851, Jul 2006.
- [6] S. Manohar, A. Kharine, J. C. G. van Hespén, W. Steenbergen, and T. G. van Leeuwen, "Photoacoustic mammography laboratory prototype: imaging of breast tissue phantoms," *Journal of Biomedical Optics*, vol. 9, pp. 1172-1181, Nov-Dec 2004.
- [7] R. O. Esenaliev, I. V. Larina, K. V. Larin, D. J. Deyo, M. Motamedi, and D. S. Prough, "Optoacoustic technique for noninvasive monitoring of blood oxygenation: a feasibility study," *Applied Optics*, vol. 41, pp. 4722-4731, Aug 1 2002.
- [8] J. Laufer, D. Delpy, C. Elwell, and P. Beard, "Quantitative spatially resolved measurement of tissue chromophore concentrations using photoacoustic spectroscopy: application to the measurement of blood oxygenation and haemoglobin concentration," *Physics in Medicine and Biology*, vol. 52, pp. 141-168, Jan 7 2007.
- [9] A. Agarwal, S. W. Huang, M. O'Donnell, K. C. Day, M. Day, N. Kotov, and S. Ashkenazi, "Targeted gold nanorod contrast agent for prostate cancer detection by photoacoustic imaging," *Journal of Applied Physics*, vol. 102, pp. -, Sep 15 2007.
- [10] P. C. Li, C. W. Wei, C. K. Liao, C. D. Chen, K. C. Pao, C. R. C. Wang, Y. N. Wu, and D. B. Shieh, "Multiple targeting in photoacoustic imaging using bioconjugated gold nanorods," in *BiOS, Proc. SPIE*, 2006, pp. 175-184.

- [11] M. A. Eghtedari, J. A. Copland, P. VL, K. NA, M. M, and O. AA, "Bioconjugated gold nanoparticles as a contrast agent for optoacoustic detection of small tumors," in *BiOS, Proc. SPIE*, 2003, pp. 76-85.
- [12] A. De La Zerda, C. Zavaleta, S. Keren, S. Vaithilingam, S. Bodapati, Z. Liu, J. Levi, B. R. Smith, T. J. Ma, O. Oralkan, Z. Cheng, X. Y. Chen, H. J. Dai, B. T. Khuri-Yakub, and S. S. Gambhir, "Carbon nanotubes as photoacoustic molecular imaging agents in living mice," *Nature Nanotechnology*, vol. 3, pp. 557-562, Sep 2008.
- [13] Y. Q. Lao, F. F. Zhou, and H. Y. Wang, "In vivo photoacoustic imaging of subcutaneous vasculature and vascular anomalies in small animals," *European Physical Journal-Applied Physics*, vol. 41, pp. 151-155, Feb 2008.
- [14] X. D. Wang, Y. J. Pang, G. Ku, G. Stoica, and L. H. V. Wang, "Three-dimensional laser-induced photoacoustic tomography of mouse brain with the skin and skull intact," *Optics Letters*, vol. 28, pp. 1739-1741, Oct 1 2003.
- [15] X. D. Wang, Y. J. Pang, G. Ku, X. Y. Xie, G. Stoica, and L. H. V. Wang, "Noninvasive laser-induced photoacoustic tomography for structural and functional in vivo imaging of the brain," *Nature Biotechnology*, vol. 21, pp. 803-806, Jul 2003.
- [16] Y. W. Wang, X. Y. Xie, X. D. Wang, G. Ku, K. L. Gill, D. P. O'Neal, G. Stoica, and L. V. Wang, "Photoacoustic tomography of a nanoshell contrast agent in the in vivo rat brain," *Nano Letters*, vol. 4, pp. 1689-1692, Sep 2004.
- [17] X. D. Wang, G. Ku, M. A. Wegiel, D. J. Bornhop, G. Stoica, and L. H. V. Wang, "Noninvasive photoacoustic angiography of animal brains in vivo with near-infrared light and an optical contrast agent," *Optics Letters*, vol. 29, pp. 730-732, Apr 1 2004.
- [18] H. P. Brecht, R. Su, M. Fronheiser, S. A. Ermilov, A. Conjusteau, A. Liopo, M. Motamedi, and A. A. Oraevsky, "Optoacoustic 3D whole-body tomography: experiments in nude mice," in *BiOS, Proc. SPIE*, 2009, pp. 0E-1.
- [19] C. M. Niemeyer, "Nanoparticles, proteins, and nucleic acids: Biotechnology meets materials science," *Angewandte Chemie-International Edition*, vol. 40, pp. 4128-4158, 2001.
- [20] M. A. Hayat, *Colloid Gold: Principles, Methods and Applications*: Academic Press: New York, 1989.
- [21] J. Kreuter, *Microcapsules and Nanoparticles in Medicine and Pharmacy*: CRC: Boca Raton, 1992.
- [22] A. P. Alivisatos, K. P. Johnsson, X. G. Peng, T. E. Wilson, C. J. Loweth, M. P. Bruchez, and P. G. Schultz, "Organization of 'nanocrystal molecules' using

- DNA," *Nature*, vol. 382, pp. 609-611, Aug 15 1996.
- [23] A. K. Boal and V. M. Rotello, "Fabrication and self-optimization of multivalent receptors on nanoparticle scaffolds," *Journal of the American Chemical Society*, vol. 122, pp. 734-735, Feb 2 2000.
- [24] C. C. Lin, Y. C. Yeh, C. Y. Yang, C. L. Chen, G. F. Chen, C. C. Chen, and Y. C. Wu, "Selective binding of mannose-encapsulated gold nanoparticles to type 1 pili in *Escherichia coli*," *Journal of the American Chemical Society*, vol. 124, pp. 3508-3509, Apr 10 2002.
- [25] C. C. Lin, Y. C. Yeh, C. Y. Yang, G. F. Chen, Y. C. Chen, Y. C. Wu, and C. C. Chen, "Quantitative analysis of multivalent interactions of carbohydrate-encapsulated gold nanoparticles with concanavalin A," *Chemical Communications*, pp. 2920-2921, 2003.
- [26] S. Link and M. A. El-Sayed, "Shape and size dependence of radiative, non-radiative and photothermal properties of gold nanocrystals," *International Reviews in Physical Chemistry*, vol. 19, pp. 409-453, Jul-Sep 2000.
- [27] M. A. Eghtedari, J. A. Copland, V. L. Popov, N. A. Kotov, M. Motamedi, and A. A. Oraevsky, "Bioconjugated gold nanoparticles as a contrast agent for detection of small tumors," in *BiOS, Proc. SPIE*, San Jose, California, USA, 2003, pp. 76-85.
- [28] S. Link and M. A. El-Sayed, "Spectral properties and relaxation dynamics of surface plasmon electronic oscillations in gold and silver nanodots and nanorods," *Journal of Physical Chemistry B*, vol. 103, pp. 8410-8426, Oct 7 1999.
- [29] S. S. Chang, C. W. Shih, C. D. Chen, W. C. Lai, and C. R. C. Wang, "The shape transition of gold nanorods," *Langmuir*, vol. 15, pp. 701-709, Feb 2 1999.
- [30] X. H. Gao, Y. Y. Cui, R. M. Levenson, L. W. K. Chung, and S. M. Nie, "In vivo cancer targeting and imaging with semiconductor quantum dots," *Nature Biotechnology*, vol. 22, pp. 969-976, Aug 2004.
- [31] D. B. Ellegala, H. L. Poi, J. E. Carpenter, A. L. Klibanov, S. Kaul, M. E. Shaffrey, J. Sklenar, and J. R. Lindner, "Imaging tumor angiogenesis with contrast ultrasound and microbubbles targeted to $\alpha(v)\beta(3)$," *Circulation*, vol. 108, pp. 336-341, Jul 22 2003.
- [32] L. Josephson, M. F. Kircher, U. Mahmood, Y. Tang, and R. Weissleder, "Near-infrared fluorescent nanoparticles as combined MR/optical imaging probes," *Bioconjugate Chemistry*, vol. 13, pp. 554-560, May-Jun 2002.
- [33] S. R. Cherry, "In vivo molecular and genomic imaging: new challenges for imaging physics," *Physics in Medicine and Biology*, vol. 49, pp. R13-R48, Feb 7 2004.

- [34] P. N. Burns and C. C. Jaffe, "Quantitative Flow Measurements with Doppler Ultrasound - Techniques, Accuracy, and Limitations," *Radiologic Clinics of North America*, vol. 23, pp. 641-657, 1985.
- [35] P. C. Li, C. J. Cheng, and C. C. Shen, "Doppler angle estimation using correlation," *IEEE Transactions on Ultrasonics Ferroelectrics and Frequency Control*, vol. 47, pp. 188-196, Jan 2000.
- [36] X. C. Chen, K. Q. Schwarz, D. Phillips, S. D. Steinmetz, and R. Schlieff, "A mathematical model for the assessment of hemodynamic parameters using quantitative contrast echocardiography," *IEEE Transactions on Biomedical Engineering*, vol. 45, pp. 754-765, Jun 1998.
- [37] Y. L. He, H. Tanigami, H. Ueyama, T. Mashimo, and I. Yoshiya, "Measurement of blood volume using indocyanine green measured with pulse-spectrophotometry: Its reproducibility and reliability," *Critical Care Medicine*, vol. 26, pp. 1446-1451, Aug 1998.
- [38] C. K. Yeh, M. J. Yang, and P. C. Li, "Contrast-specific ultrasonic flow measurements based on both input and output time intensities," *Ultrasound in Medicine and Biology*, vol. 29, pp. 671-678, May 2003.
- [39] C. Loo, A. Lin, L. Hirsch, M. H. Lee, J. Barton, N. Halas, J. West, and R. Drezek, "Nanoshell-enabled photonics-based imaging and therapy of cancer," *Technology in Cancer Research & Treatment*, vol. 3, pp. 33-40, Feb 2004.
- [40] V. Tuchin, *Tissue optics: light scattering methods and instruments for medical diagnosis*. Bellingham, WA: Georgia Institute of Technology, 2000.
- [41] H. Brannon, "<http://dermatology.about.com/cs/skinanatomy/a/anatomy.htm>."
- [42] K. L. Zierler, "Theoretical Basis of Indicator-Dilution Methods for Measuring Flow and Volume," *Circulation Research*, vol. 10, pp. 393-&, 1962.
- [43] V. Moravi, S. Akselrod, D. David, L. Keselbrener, and Y. Bitton, "Myocardial Transit-Time of the Echocardiographic Contrast-Media," *Ultrasound in Medicine and Biology*, vol. 19, pp. 635-648, 1993.
- [44] K. Wei, A. R. Jayaweera, S. Firoozan, A. Linka, D. M. Skyba, and S. Kaul, "Quantification of myocardial blood flow with ultrasound-induced destruction of microbubbles administered as a constant venous infusion," *Circulation*, vol. 97, pp. 473-483, Feb 10 1998.
- [45] C. K. Yeh, D. E. Kruse, M. C. Lim, D. E. Redline, and K. W. Ferrara, "A new high frequency destruction/reperfusion system," in *Proc. IEEE Ultrason. Symp.*, Hawaii, USA, 2003.
- [46] E. A. Gardner, R. Bendiksen, N. Sponheim, G. L. Holley, A. Tornes, S. Krishnan, P. D. Miller, K. Fowkes, A. Gee, and K. G. Oygarden, "Synchronization of

- contrast agent destruction and imaging for perfusion assessment," in *Proc. IEEE Ultrason. Symp.*, 2000, pp. 1911-1915.
- [47] P. C. Li, C. W. Wei, C. K. Liao, H. C. Tseng, Y. P. Lin, and C. C. Chen, "Time-intensity based optoacoustic flow measurements with gold nanoparticles," in *BiOS, Proc. SPIE*, San Jose, California, USA, 2005, pp. 63-72.
- [48] P. C. Li, C. K. Yeh, and S. W. Wang, "Time-intensity-based volumetric flow measurements: An in vitro study," *Ultrasound in Medicine and Biology*, vol. 28, pp. 349-358, Mar 2002.
- [49] C. K. Yeh, S. W. Wang, and P. C. Li, "Feasibility study of time-intensity-based blood flow measurements using deconvolution," *Ultrasonic Imaging*, vol. 23, pp. 90-105, Apr 2001.
- [50] S. Aronson, J. G. Wienczek, S. B. Feinstein, P. A. Heidenreich, J. G. Zaroff, R. Walker, and M. F. Roizen, "Assessment of Renal Blood-Flow with Contrast Ultrasonography," *Anesthesia and Analgesia*, vol. 76, pp. 964-970, May 1993.
- [51] T. R. Harris and E. V. Newman, "An Analysis of Mathematical Models of Circulatory Indicator-Dilution Curves," *Journal of Applied Physiology*, vol. 28, pp. 840-&, 1970.
- [52] C. W. Sheppard, *Basic Principles of the Tracer Method*. New York: NY: Wiley, 1962.
- [53] L. T. Ltd., "<http://www.lotis-tii.com/files/LS-2132U.pdf>," Minsk, Belarus.
- [54] P. C. Li, S. W. Huang, C. W. Wei, Y. C. Chiou, C. D. Chen, and C. R. C. Wang, "Photoacoustic flow measurements by use of laser-induced shape transitions of gold nanorods," *Optics Letters*, vol. 30, pp. 3341-3343, Dec 15 2005.
- [55] B. W. Zweifach and H. H. Lipowsky, "Pressure and flow distribution in microcirculation." vol. 11, E. M. R. a. C. C. Michel, Ed. Washington, D. C.: American Physiological Society, 1985, pp. 251-307.
- [56] K. Shah, A. Jacobs, X. O. Breakefield, and R. Weissleder, "Molecular imaging of gene therapy for cancer," *Gene Therapy*, vol. 11, pp. 1175-1187, Aug 2004.
- [57] P. C. Li, C. W. Wei, C. K. Liao, C. D. Chen, K. C. Pao, C. R. C. Wang, Y. N. Wu, and D. B. Shieh, "Photoacoustic imaging of multiple targets using gold nanorods," *IEEE Transactions on Ultrasonics Ferroelectrics and Frequency Control*, vol. 54, pp. 1642-1647, Aug 2007.
- [58] D. L. Chamberland, A. Agarwal, N. Kotov, J. B. Fowlkes, P. L. Carson, and X. Wang, "Photoacoustic tomography of joints aided by an Etanercept-conjugated gold nanoparticle contrast agent - an ex vivo preliminary rat study," *Nanotechnology*, vol. 19, pp. -, Mar 5 2008.
- [59] J. A. Copland, M. Eghtedari, V. L. Popov, N. Kotov, N. Mamedova, M.

- Motamedi, and A. A. Oraevsky, "Bioconjugated gold nanoparticles as a molecular based contrast agent: Implications for imaging of deep tumors using optoacoustic tomography," *Molecular Imaging and Biology*, vol. 6, pp. 341-349, Sep-Oct 2004.
- [60] W. Fu, D. B. Shenoy, G. Jones, C. Dimarzio, S. Sridhar, and M. Amiji, "Biomedical applications of gold nanoparticles functionalized using hetero-bifunctional poly(ethylene glycol) spacer," in *Mater. Res. Soc. Symp. Proc.* vol. **845**, 2005, pp. AA5.4.1-6.
- [61] F. Meric-Bernstam and M. C. Hung, "Advances in targeting human epidermal growth factor receptor-2 signaling for cancer therapy," *Clinical Cancer Research*, vol. 12, pp. 6326-6330, Nov 1 2006.
- [62] S. Kalyankrishna and J. R. Grandis, "Epidermal growth factor receptor biology in head and neck cancer," *Journal of Clinical Oncology*, vol. 24, pp. 2666-2672, Jun 10 2006.
- [63] H. Hanaoka, T. Mukai, H. Tamamura, T. Mori, S. Ishino, K. Ogawa, Y. Iida, R. Doi, N. Fujii, and H. Saji, "Development of a In-111-labeled peptide derivative targeting a chemokine receptor, CXCR4, for imaging tumors," *Nuclear Medicine and Biology*, vol. 33, pp. 489-494, May 2006.
- [64] S. Hatse, K. Princen, E. De Clercq, M. M. Rosenkilde, T. W. Schwartz, P. E. Hernandez-Abad, R. T. Skerlj, G. J. Bridger, and D. Schols, "AMD3465, a monomacrocyclic CXCR4 antagonist and potent HIV entry inhibitor," *Biochemical Pharmacology*, vol. 70, pp. 752-761, Sep 1 2005.
- [65] S. Zitzmann, V. Ehemann, and M. Schwab, "Arginine-glycine-aspartic acid (RGD)-peptide binds to both tumor and tumor-endothelial cells in vivo," *Cancer Research*, vol. 62, pp. 5139-5143, Sep 15 2002.
- [66] B. R. Line, A. Mitra, A. Nan, and H. Ghandehari, "Targeting tumor angiogenesis: comparison of peptide and polymer-peptide conjugates," *J Nucl Med*, vol. 46, pp. 1552-60, Sep 2005.
- [67] Z. Su, G. Z. Liu, S. Gupta, Z. H. Zhu, M. Rusckowski, and D. J. Hnatowich, "In vitro and in vivo evaluation of a technetium-99m-labeled cyclic RGD peptide as a specific marker of alpha(V)beta(3) integrin for tumor imaging," *Bioconjugate Chemistry*, vol. 13, pp. 561-570, May-Jun 2002.
- [68] H. M. Ellerby, W. Arap, L. M. Ellerby, R. Kain, R. Andrusiak, G. D. Rio, S. Krajewski, C. R. Lombardo, R. Rao, E. Ruoslahti, D. E. Bredesen, and R. Pasqualini, "Anti-cancer activity of targeted pro-apoptotic peptides," *Nat Med*, vol. 5, pp. 1032-8, Sep 1999.
- [69] Y. Y. Yu, S. S. Chang, C. L. Lee, and C. R. C. Wang, "Gold nanorods: Electrochemical synthesis and optical properties," *Journal of Physical*

- Chemistry B*, vol. 101, pp. 6661-6664, Aug 21 1997.
- [70] C. W. Shih, W. C. Lai, C. C. Hwang, S. S. Chang, and C. R. C. Wang, *Metal Nanoparticles: Synthesis, Characterization, and Application*, 2001.
- [71] L. R. Hirsch, J. B. Jackson, A. Lee, N. J. Halas, and J. West, "A whole blood immunoassay using gold nanoshells," *Analytical Chemistry*, vol. 75, pp. 2377-2381, May 15 2003.
- [72] H. W. Liao and J. H. Hafner, "Gold nanorod bioconjugates," *Chemistry of Materials*, vol. 17, pp. 4636-4641, Sep 6 2005.
- [73] B. W. Zweifach and H. H. Lipowsky, "Pressure and flow distribution in microcirculation," in *Handbook of Physiology*. vol. 11, E. M. R. a. C. C. Michel, Ed. Washington, D. C: American Physiological Society, 1985.
- [74] "Optical Absorption Spectra <http://omlc.ogi.edu/spectra/index.html>."
- [75] X. H. Huang, P. K. Jain, I. H. El-Sayed, and M. A. El-Sayed, "Plasmonic photothermal therapy (PPTT) using gold nanoparticles," *Lasers in Medical Science*, vol. 23, pp. 217-228, Jul 2008.
- [76] I. V. Larina, K. V. Larin, and R. O. Esenaliev, "Real-time optoacoustic monitoring of temperature in tissues," *Journal of Physics D-Applied Physics*, vol. 38, pp. 2633-2639, Aug 7 2005.
- [77] J. Shah, S. R. Aglyamov, K. Sokolov, T. E. Milner, and S. Y. Emelianov, "Ultrasound-Based Thermal and Elasticity Imaging to Assist Photothermal Cancer Therapy - Preliminary Study," in *Proc. IEEE Ultrason Symp*, 2006, pp. 1029-1032.
- [78] J. Kandulla, H. Elsner, R. Birngruber, and R. Brinkmann, "Noninvasive optoacoustic online retinal temperature determination during continuous-wave laser irradiation," *Journal of Biomedical Optics*, vol. 11, pp. -, Jul-Aug 2006.
- [79] J. Shah, S. Park, S. Aglyamov, T. Larson, L. Ma, K. Sokolov, K. Johnston, T. Milner, and S. Y. Emelianov, "Photoacoustic imaging and temperature measurement for photothermal cancer therapy," *Journal of Biomedical Optics*, vol. 13, pp. -, May-Jun 2008.
- [80] S. H. Wang, "Photoacoustic quantitative thermal imaging for laser-induced thermotherapy," in *Graduate Institute of Biomedical Electronics and Bioinformatics*. vol. Master Taipei: National Taiwan University, 2009, p. 92.
- [81] S. R. Arridge, H. Dehghani, M. Schweiger, and E. Okada, "The finite element model for the propagation of light in scattering media: A direct method for domains with nonscattering regions," *Medical Physics*, vol. 27, pp. 252-264, Jan 2000.
- [82] E. W. Weisstein, "<<http://mathworld.wolfram.com/WaveEquation.html>>."
- [83] P. F. Stetson, F. G. Sommer, and A. Macovski, "Lesion contrast enhancement in

- medical ultrasound imaging," *IEEE Transactions on Medical Imaging*, vol. 16, pp. 416-425, Aug 1997.
- [84] "American National Standard for the Safe Use of Lasers in Health Care Facilities: Standard Z136.1-2000," A. N. S. Institute, Ed. ANSI, Inc., New York, 2000.
- [85] B. R. Zetter, "Angiogenesis and tumor metastasis," *Annual Review of Medicine*, vol. 49, pp. 407-424, 1998.
- [86] W. F. Cheng, C. N. Lee, J. S. Chu, C. A. Chen, T. M. Chen, W. Y. Shau, C. Y. Hsieh, and F. J. Hsieh, "Vascularity index as a novel parameter for the in vivo assessment of angiogenesis in patients with cervical carcinoma," *Cancer*, vol. 85, pp. 651-657, Feb 1 1999.
- [87] P. C. Li, C. R. C. Wang, D. B. Shieh, C. W. Wei, C. K. Liao, C. Poe, S. Jhan, A. A. Ding, and Y. N. Wu, "In vivo Photoacoustic Molecular Imaging with Simultaneous Multiple Selective Targeting Using Antibody-Conjugated Gold Nanorods," *Optics Express*, vol. 16, pp. 18605-18615, Nov 10 2008.



Publication List

Journal papers:

1. **C.-W. Wei**, S.-W. Huang, C.-R. C. Wang, and P.-C. Li, "Photoacoustic flow measurements based on wash-in analysis of gold nanorods," *IEEE Trans. Ultrason. Ferroelectr. Freq. Control*, vol. 54, no. 6, pp. 1131-1141, 2007.
2. **C.-W. Wei**, C.-K. Liao, H.-C. Tseng, Y.-P. Lin, C.-C. Chen, and P.-C. Li, "Photoacoustic flow measurements with gold nanoparticles," *IEEE Trans. Ultrason. Ferroelectr. Freq. Control*, vol. 53, pp. 1955-1959, 2006.
3. P.-C. Li, C.-R. C. Wang, D.-B. Shieh, **C.-W. Wei**, C.-K. Liao, C. Poe, S. Jhan, A.-A. Ding, and Y.-N. Wu, "In vivo photoacoustic molecular imaging with simultaneous multiple selective targeting using antibody-conjugated gold nanorods," *Opt. Express*, vol. 16, no. 23, pp. 18605-18615, 2008.
4. P.-C. Li, **C.-W. Wei**, and Y.-L. Sheu, "Subband photoacoustic imaging for contrast improvement," *Opt. Express*, vol. 16, no. 25, pp. 20215-20226, 2008.
5. P.-C. Li, S.-W. Huang, **C.-W. Wei**, Y.-C. Chiou, C.-D. Chen, and C.-R. C. Wang, "Photoacoustic flow measurements by use of laser-induced shape transitions of gold nanorods," *Opt. Lett.*, vol. 30, pp. 3341-3343, 2005.
6. D.-H. Huang, C.-K. Liao, **C.-W. Wei**, and P.-C. Li, "Simulations of photoacoustic wave propagation in light-absorbing media using a finite-difference time-domain method," *J. Acoust. Soc. Am.*, vol. 117, pp. 2795-801, 2005.
7. C.-K. Liao, S.-W. Huang, **C.-W. Wei**, and P.-C. Li, "Nanorod-based flow estimation using a high-frame-rate photoacoustic imaging system," *J. Biomedical Opt.*, vol. 12, no. 6, pp. 064006-1-9, 2007.

International conference papers:

1. **C.-W. Wei**, S.-W. Huang, Y.-C. Chiou, C.-D. Chen, C.-R. C. Wang, and P.-C. Li, "Single-energy wash-in photoacoustic blood flow measurements using shape transitions of gold nanorods," *SPIE International Symposium on Biomedical Optics*,

vol. 6086, San Jose, California, USA, Jan., 2006.

2. **C.-W. Wei**, Y.-L. Sheu, and P.-C. Li, "Photoacoustic contrast enhancement using selective subband imaging: experimental results," SPIE International Symposium on Biomedical Optics, vol. 6437, San Jose, California, Jan., 2007.
3. **C.-W. Wei**, C.-K. Liao, Y.-Y. Chen, C.-R. C. Wang, A.-A. Ding, D.-B. Shieh, and P.-C. Li, "In vivo Photoacoustic Imaging with Multiple Selective Targeting Using Bioconjugated Gold Nanorods, " SPIE International Symposium on Biomedical Optics, vol. 6856, San Jose, California, USA, Jan., 2008.
4. P.-C. Li, **C.-W. Wei** , C.-K. Liao, H.-C. Tseng, Y.-P. Lin, and C.-C. Chen, "Time-intensity based optoacoustic flow measurements with gold nanoparticles," SPIE International Symposium on Biomedical Optics, vol. 5697, San Jose, California, USA, Jan., 2005.
5. C.-K. Liao, S.-W. H., **C.-W. Wei**, and P.-C. Li, "A high frame rate photoacoustic imaging system and its applications to perfusion measurements," 2005 SPIE International Symposium on Biomedical Optics, vol. 6086, San Jose, California, USA, Jan., 2005.
6. P.-C. Li, **C.-W. Wei**, C.-K. Liao, C.-D. Chen, K.-C. Pao, and C.-R. C. Wang, Y.-N. Wu, and D.-B. Shieh, "Multiple targeting in photoacoustic imaging using bioconjugated gold nanorods," SPIE International Symposium on Biomedical Optics, vol. 6086, San Jose, California, USA, Jan., 2006.
7. Y.-L. Sheu, **C.-W. Wei**, P.-C. Li, "Effects of absorption properties on photoacoustic spectral characteristics: numerical analysis," SPIE International Symposium on Biomedical Optics, San Jose, California, USA, vol. 6437, Jan., 2007.
8. J.-H. Liu, **C.-W. Wei**, Y.-L. Sheu, Y.-T. Tasi , Y.-H. Wang, and P.-C. Li, " Design, fabrication, and testing of a dual-band photoacoustic transducer," SPIE International Symposium on Biomedical Optics, San Jose, California, USA, vol. 7177, Jan., 2009.

Local conference papers:

1. **C.-W. Wei**, C.-K. Liao, and P.-C. Li, "Applications of gold nanoparticles in opto-acoustic imaging: quantitative blood flow estimation," Symposium of Annual Conference of the Biomedical Engineering Society, Tainan, Taiwan, R.O.C., Dec.,

2004.

2. **C.-W. Wei**, S.-W. Huang, C.-R. C. Wang, K.-C. Pao, Y.-C. Chiou, and P.-C. Li, “Photoacoustic flow estimations based on shape transition of gold nanorods,” Symposium of Annual Conference of the Biomedical Engineering Society, Taoyuan, Taiwan, R.O.C., Dec., 2005.
3. **C.-W. Wei**, C.-K. Liao, P.-C. Li, C.-D. Chen, K.-C. Pao, C.-R. C. Wang, Y.-N. Wu, A.-A. Ding, and D.-B. Shieh, “photoacoustic molecular imaging using bioconjugated gold nanorods with multiple targeting,” Symposium of Annual Conference of the Biomedical Engineering Society, Taipei, Taiwan, R.O.C., Dec., 2006.
4. **C.-W. Wei**, C.-K. Liao, Y.-Y. Chen, C. Poe, C.-R. C. Wang, A.-A. Ding, D.-B. Shieh, and P.-C. Li, “Multiple selective targeting in photoacoustic molecular imaging using gold nanorods,” Symposium of Annual Conference of the Biomedical Engineering Society, Taichung, Taiwan, R.O.C., Dec., 2007.
5. **C.-W. Wei**, C.-K. Liao, C. Poe, Z.-M. Chen, C.-R. C. Wang, P.-C. Wu, Z.-S. Yang, D.-B. Shieh, and P.-C. Li, “In vivo multiple selective targeting in photoacoustic molecular imaging using gold nanorods,” Symposium of Annual Conference of the Biomedical Engineering Society, Taipei, Taiwan, R.O.C., Dec., 2008.
6. C.-K. Liao, **C.-W. Wei**, D.-H. Huang, M.-L. Li, and P.-C. Li, “Improved backward opto-acoustic imaging using synthetic aperture focusing technique,” Symposium of Annual Conference of the Biomedical Engineering Society, Taipei, Taiwan, R.O.C., Dec., 2003.
7. D.-H. Huang, C.-K. Liao, **C.-W. Wei**, and P.-C. Li, “Simulation of optoacoustic wave propagation in light absorbing media,” Symposium of Annual Conference of the Biomedical Engineering Society, Taipei, Taiwan, R.O.C., Dec., 2003.